

CAD MODELING AND INTERFACE STRESS
ANALYSIS OF DIAMOND-COATED
TOOLING

by

CHAO MIAO

A THESIS

Submitted in partial fulfillment of the requirements
for the degree of Master of Science in the
Department of Mechanical Engineering
in the Graduate School of
The University of Alabama

TUSCALOOSA, ALABAMA

2010

Copyright Chao Miao 2010
ALL RIGHTS RESERVED

ABSTRACT

Diamond-coated cutting tools have been widely employed in machining applications due to their superior properties. However, during the deposition process, significant residual stresses will be generated to affect the coating-substrate adhesion quality. In addition, interface delamination is another major factor causing catastrophic tool failure.

The objectives of this research consist of: (1) to evaluate deposition-induced residual stresses of diamond-coated drills, (2) to analyze the interface failure of diamond-coated tools by numerical simulations of indentations, and (3) to evaluate deposition-induced residual stresses developed on diamond-coated macro/micro end mills with the inclusion of a cohesive zone model. The research scopes of this research are to investigate diamond-coated tool residual stresses as well as interface behaviors under the contact loading. The research methodologies include: (1) 3D CAD modeling of diamond coated drills and macro/micro end mills, (2) finite element analysis (FEA) of diamond-coated cutting tools after the deposition, and (3) indentation based simulations incorporating a cohesive zone model for the analysis of interface behaviors.

The major findings were summarized as follows: (1) for diamond-coated drills, FEA results indicated that the edge radius had the most dominant effect on interface stresses, which were 1.41 GPa, 3.11 GPa for $3\ \mu\text{m}\ r_e$ and 0.73 GPa, 2.94 GPa for $15\ \mu\text{m}\ r_e$ in terms of $\sigma_{r_{\max}}$ and $\sigma_{\theta_{\max}}$, (2) for the indentation with a spherical indenter, increasing the coating Young's Modulus reduced delamination sizes, and a thicker coating tended to have greater resistance to the interface delamination. Residual stresses facilitated the interface delamination. For the

indentation with a wedge indenter, substrate surface curvature slightly affected the loading vs. displacement curve. Residual stresses increased delamination sizes. The coating with a larger Young's Modulus had less delamination sizes, and (3) as for diamond-coated end mills, the edge radius still dominantly affected residual stresses. When the size of macro end mills was scaled down to micro level, interface stresses were increased. The existence of a CZM reduced residual stresses. The major achievements included (1) diamond-coated tool geometry and cohesive zone effects on residual stresses and interface stresses, and (2) coating attribute, residual stresses, and substrate surface curvature effects on the interface behavior.

LIST OF ABBREVIATIONS AND SYMBOLS

<i>PCD</i>	polycrystalline diamond
<i>CVD</i>	chemical vapor deposition
<i>MMC</i>	metal matrix composite
<i>FEA</i>	finite element analysis
<i>FE</i>	finite element
<i>R</i>	indenter radius (μm)
<i>NCD</i>	nano-crystalline diamond
<i>MCD</i>	microcrystalline diamond
<i>Al</i>	aluminum
δ_{max}	characteristic length (μm)
σ_{max}	cohesive strength (MPa)
σ_x	stress along the x direction (GPa)
σ_y	stress along the y direction (GPa)
T_0	work of separation for brittle materials (J/m^2)
T_1	work of plastic deformation (J/m^2)
\emptyset_{sep}	work of separation (J/m^2)
δ	normalizing parameter
\emptyset_n	work of normal separation (J/m^2)
\emptyset_t	work of tangential separation (J/m^2)
δ_n	critical displacements under normal condition (μm)

δ_t critical displacements under shear condition (μm)

E Young's Modulus (GPa)

δ_c critical displacement (μm)

δ_1 factor governing shape

δ_2 factor governing shape

σ_0 normal stress at impact fracture initiation (MPa)

τ_0 shear stress at impact fracture initiation (MPa)

$\delta_{\sigma cr}$ critical normal opening displacement (μm)

$\delta_{\tau cr}$ critical shear opening displacement (μm)

Δ_n normal displacement jump (μm)

Δ_t tangential displacement jump (μm)

UMIS Ultra-Micro-Indentation System

AFM atomic force microscopy

MWIT Microwedge Indentation Test

FEM finite element method

WC tungsten-carbide

CAD computer-aided design

r_e edge radius (μm)

σ_r radial normal stress (GPa)

σ_θ circumferential normal stress (GPa)

$\tau_{r\theta}$ shear stress (GPa)

ν Poisson's ratio

CAX4R a 4-node bilinear axisymmetric quadrilateral, reduced integration, hourglass control

COHAX4 a 4-node axisymmetric cohesive element

t coating thickness (μm)

σ_0 strength coefficient (MPa)

n strain hardening exponent

σ_y yield strength (MPa)

Δ_n^c critical normal separations (μm)

Δ_t^c critical tangential separations (μm)

Δ_n non-dimensional normal displacement jumps (μm)

Δ_t non-dimensional tangential displacement jumps (μm)

Δ non-dimensional total displacement jumps (μm)

$G1$ interface stiffness for normal mode (GPa)

$G2$ interface stiffness for shear mode (GPa)

$S22$ normal traction (GPa)

t coating thickness (μm)

FCM fictitious crack model

CPEAR a 4-node bilinear plane strain quadrilateral, reduced integration, hourglass control

COH2D4 a 4-node two-dimensional cohesive element

ξ viscosity factor

\emptyset_1 first relief angle (degree)

γ rake angle (degree)

R_c chamfer length (mm)

β helix angle (degree)

L_c cutter length (mm)

L	overall length (mm)
Φ_2	second relief angle (degree)
R_i	radius of inner circle (mm)
D_s	shank diameter (mm)
D_c	cutter diameter (mm)
L_s	shank length (mm)
N_f	number of flutes
CAM	computer aided manufacturing
$HF-CVD$	hot-filament chemical vapor deposition
r_e	edge radius (μm)
h	helix angle (degree)
r	drill radius (mm)
l	flute length (mm)
w	webthickness (mm)
p	point angle (degree)
s	distance between the top plane and offset plane (mm)
t_1	first wheel thickness (mm)
θ_1	first wheel angle (degree)
Φ_1	first relief angle (degree)
Φ_2	second relief angle (degree)
C_w	cutter width (mm)
$t_2 - t_1$	second wheel thickness (mm)
θ_2	second wheel angle (degree)

ACKNOWLEDGMENTS

First and foremost, I must express my deepest appreciation for my research and thesis advisor, Dr. Y. Kevin Chou, for his guidance, patience, encouragement, support and understanding. Dr. Chou's invaluable insights, comments and suggestions play critical roles in helping me to accomplish this thesis. I must thank Dr. Chou again for giving me this opportunity to further my graduate study and conduct the research under his technical guidance at The University of Alabama. During the whole course of research, Dr. Chou not only provided me the insightful advice and suggestions to help me out of the obstacles, but also taught me how to be a mature graduate student with the capability to solve tough problems, and brew innovative research ideas, which supplied me with the driving force to be an independent thinker. Dr. Chou's mentorship has helped me to learn a lot from him. I hope that one day I can become an advisor as excellent as Dr. Chou.

I show my deep appreciation for Dr. Joey K. Parker, Dr. Daniel J. Fonseca and Dr. Jialai Wang for consenting to be on my thesis committee, whose valuable supports and remarks are critical to the completion of my thesis.

An immense debt of gratitude is owed to my parents MinSheng Miao and Fang Liu, and my wife Shanshan Qian. Without their patience and encouragement, the completion of this thesis will not be possible.

I would also like to express my gratitude to the members in our group, Feng Qin and Ping Lu, for their assistance to my research. Special thanks are given to Dr. James L. Wang, Aishen Chao, Dr. Guohai Jing, Yi Wang, Chao Zhang, Xin Yang, Hsiao-Ching Kuo, Chen Dai, and Dr. Yuxin Feng as well as other friends in Tuscaloosa Chinese Christian Church. I feel honored to have those friends in my life because they have not only provided me enormous support when I am in Tuscaloosa but also introduced me to the kingdom of God.

Last but not least, financial support from the National Science Foundation (NSF) and Vista Engineering, Inc. is also acknowledged.

CONTENTS

ABSTRACT.....	ii
LIST OF ABBREVIATIONS AND SYMBOLS	iv
ACKNOWLEDGMENTS	viii
LIST OF TABLES	xiv
LIST OF FIGURES	xv
1. INTRODUCTION	1
Background and Motivation	1
Research Objectives and Scope	5
Organization of the Thesis	6
2. INTEGRATED DESIGN AND ANALYSIS OF DIAMOND- COATED DRILLS	8
Abstract	8
Introduction.....	9
Solid Modeling of 3D Diamond-Coated Two Flute Twist Drills...	11
Finite Element Analysis of Deposition Stresses	12
3D Drill Stress Analysis.....	12
2D Approximation	15
Drill Geometry Effects.....	18
Conclusions.....	23

Acknowledgments.....	24
References.....	24
3. NUMERICAL ANALYSIS OF INTERFACE BEHAVIOR OF DIAMOND COATED TOOLS	26
Abstract	26
Introduction.....	27
Finite Element Model of Indentation with a Spherical Indenter.....	31
Physical Phenomenon Formulation of Indentation Simulation with Spherical Indenter	31
Interface Behavior Modeling	32
Cohesive Zone Parameter Determination	34
Results and Discussions for Indentations with a Spherical Indenter	35
Typical Examples for Indentations with a Spherical Indenter	35
Coating Attribute Effects on Indentations with a Spherical Indenter	40
A Finite Element Model of Indentations with a Wedge Indenter ...	42
Problem Description	42
Physical Phenomenon Formulation of Indentation Simulations with a Wedge Indenter	44
Interface Behavior Modeling and Cohesive Parameters Determination	45
Results and Discussions for Indentations with a Wedge Indenter ..	45
Typical Examples for Indentations with a Wedge Indenter..	45
Coating Attribute Effects on Indentations with a Wedge Indenter	49

Conclusions.....	56
Acknowledgments.....	57
References.....	57
4. CAD AND FEA OF DIAMOND-COATED END MILLS WITH CZM INCLUSION	61
Abstract.....	61
Introduction.....	62
Solid Modeling of 3D Diamond-Coated Four Flutes Corner Chamfer Macro End Mills	66
Finite Element Analysis of Diamond-Coated Macro End Mill Deposition Residual Stresses	68
3D Diamond-Coated Macro End Mill Residual Stress Analysis.....	68
2D Approximation	69
Diamond-Coated Macro End Mill Geometric Parameters Effect.....	72
Finite Element Analysis of Diamond-Coated Micro End Mill Deposition Residual Stresses	76
Modeling Process and Cross Section Generation of Diamond-Coated Micro End Mills	76
3D Diamond-Coated Micro End Mill Analysis	77
Diamond-Coated Micro End Mill 2D Cross Section FE Simulation.....	78
2D Approximation with the Inclusion of a CZM.....	82
Conclusions.....	86
Acknowledgments.....	87
References.....	87

5. CONCLUSIONS AND RECOMMENDATIONS FOR FUTURE RESEARCH.....	91
Conclusions.....	91
Contributions	93
Recommendations for Future Research.....	94
REFERENCES	96
APPENDIX A. 3D DIAMOND-COATED DRILL CAD MODELING PROCESS	97
APPENDIX B. 3D DIAMOND-COATED END MILL CAD MODELING PROCESS.....	104

LIST OF TABLES

2.1. Wedge Angle ($^{\circ}$) at Different Sections of Drills with Different Point and Helix Angles	20
2.2. Maximum Interface Normal Stresses for Different Edge Radii	22
2.3. Maximum Interface Normal Stresses for Different Helix Angles	22
2.4. Maximum Interface Normal Stresses for Different Point Angles	23
2.5. Maximum Interface Normal Stresses for Different Web Thicknesses	23
3.1. Material Properties of WC-Co Substrate	32
3.2. The Cohesive Zone Parameters for Diamond-Coated WC-insert.....	35
3.3. Range of Parameters Studied for Indentation Simulations with a Spherical Indenter	39
3.4. Range of Parameters Studied for Indentation Simulations with a Wedge Indenter	49
4.1. Parameters to Define End-milling Cutter Dimensions	63
4.2. Maximum Radial Normal Stress for Different Edge Radii	76
4.3. Maximum Radial Normal Stress for Different Coating Thicknesses ..	76
4.4. Edge Radius Effect on Interfacial Stresses for 2D Diamond-Coated Macro/Micro End Mills.	82
4.5. Maximum Radial Normal Stresses and Circumferential Stresses for End Mills with Different Edge Radii with the Inclusion of a CZM. ..	85
4.6. Maximum Radial Normal Stresses and Circumferential Stresses for End Mills with Different Coating Thicknesses with the Inclusion of a CZM.....	85

LIST OF FIGURES

1.1. First proposed cohesive zone concept.....	3
1.2. Bilinear cohesive zone model.....	4
1.3. (a) Stress distribution around the cutting tool edge (b) Edge radius effects on interfacial radial normal stresses	4
2.1. (a) Configuration of a standard two-flute twist drill and (b) an actual twist drill.....	10
2.2. An example of (a) fully defined twist drill solid model and (b) diamond-coated twist drill	12
2.3. Element meshing for diamond-coated drill stress simulations: (a) the entire drill model and (b) around drill tip.....	13
2.4. An example of stress distributions (longitudinal normal stress) in a diamond-coated drill: (a) overall and (b) near drill tip	14
2.5. Longitudinal normal stress contours in a sectional view of a diamond-coated drill: (a) overall and (b) near drill tip	15
2.6. An example of 2D section of a drill for FEA stress analysis: (a) Sectional plane specification, (b) Intersected profile on the drill, and (c) 2D view of the cross-section.....	16
2.7. Deposition stress contours (maximum principal stress) in a 2D coated-drill section: (a) overall distribution and (b) around the cutting edge area	17
2.8. (a) A schematic drawing showing the interfacial stress components around the edge area, and (b) Interface stress profiles around the cutting edge of a diamond-coated drill cross-section	18

2.9. Drills with different helix angles: (a) 20°, (b) 30°, and (c) 40°	19
2.10. Drills with different point angles: (a) 90°, (b) 118°, and (c) 135°	19
2.11. Locations of different drill cross-sections analyzed in Table 2.1	20
2.12. Interface stress profiles, radial normal component, for drills of different helix angles.....	21
2.13. Edge radius effects on interface stress profiles of diamond- coated drills: (a) radial normal stress, and (b) circumferential normal stress	21
3.1. (a). Polynomial type cohesive zone, (b) polynomial and exponential type cohesive zone, and (c) exponential fit for normal T_n and trigonometric fit for shear T_t	29
3.2. Traction-separation response	30
3.3. Bilinear traction separation response.....	30
3.4. Schematic of the indentation on a coated substrate by a sphere	32
3.5. (a) Normal traction T_n as a function of the normal separation Δ_n for $\Delta_t=0$, (b) shear traction T_t as a function of the shear separation Δ_t for $\Delta_n=0$	33
3.6. Example of plastic behaviors in a coating-substrate system during the indentation process (a) fully loading and (b) completely unloading.....	36
3.7. (a) Stress contours of the normal separation as the indenter completely withdrawn, (b) the normal traction at the interface, and (c) the normal separation at the interface.	37
3.8. The normal traction at the interface after the indenter completely unloaded.....	38
3.9. No cracked cohesive elements along the interface.	38
3.10. Loading vs. delamination sizes ($E = 1200$ GPa, Deposition Temperature = 800°C, Coating Thickness = 30 μ m).....	39
3.11. Effects of the coating Young's Modulus and residual stresses on interface delamination sizes (Coating Thickness = 30 μ m, Deposition Temperature = 800°C).	40

3.12. Effects of the coating thickness and residual stresses on delamination sizes ($E = 1200$ GPa, Deposition Temperature = 800°C).	41
3.13. Residual stresses effect on the diamond-coated insert with the inclusion of a cohesive zone: (a) overall view, (b) zoomed-in view of the cutting edge, (c) radial normal stress, and (d) circumferential stress.....	43
3.14. Indentation finite element model with a wedge indenter.....	45
3.15. (a) Residual stresses contours during the initial state, (b) S22 stress contour, fully loading, and (c) zoom-in view of the contact area between the indenter and the coating ($E = 1200$ GPa, Coating Thickness = $30\ \mu\text{m}$, Deposition Temperature = 800°C , Specimen Radius = $700\ \mu\text{m}$, Indentation Depth = $10\ \mu\text{m}$).....	46
3.16. Equivalent plastic strains, fully unloading, $10\ \mu\text{m}$ indentation depths ($E = 1200$ GPa, Coating Thickness = $30\ \mu\text{m}$, Deposition Temperature = 800°C , Specimen Radius = $700\ \mu\text{m}$, Indentation Depth = $10\ \mu\text{m}$).....	46
3.17. (a) Normal separations after indenter fully unloaded, (b) normal tractions at the interface, and (c) normal separations at the interface. ($E = 1200$ GPa, Coating Thickness = $30\ \mu\text{m}$, Specimen Radius = $700\ \mu\text{m}$, Deposition Temperature = 800°C , Indentation Depth = $10\ \mu\text{m}$).....	47
3.18. Normal traction vs. horizontal distance at the interface after indenter completely unloaded.....	48
3.19. Loading vs. delamination size ($E = 1200$ GPa, σ_r (Residual Stresses) = 0 GPa, Coating Thickness = $30\ \mu\text{m}$, Specimen Radius = $700\ \mu\text{m}$).....	48
3.20. Loading vs. displacement curves with different curvatures ($E = 1200$ GPa, σ_r (Residual Stresses) = 0 GPa, Coating Thickness = $30\ \mu\text{m}$, Indentation Depth = $10\ \mu\text{m}$).....	50
3.21. Curvature and residual stresses effects on delamination sizes ($E = 1200$ GPa, Coating Thickness = $30\ \mu\text{m}$, Indentation Depth = $10\ \mu\text{m}$).....	50
3.22. (a) Normal tractions and separations for a model with a specimen radius = $2800\ \mu\text{m}$, and (b) normal tractions and separations for a model with a specimen radius = $100\ \mu\text{m}$ ($E = 1200$ GPa, σ_r (Residual Stresses) = 0 GPa, Coating Thickness = $30\ \mu\text{m}$,	

Indentation Depth = 10 μm).....	51
3.23. Curvature effects on the critical loading ($E = 1200 \text{ GPa}$, σ_r (Residual Stresses) = 0 GPa, Coating thickness = 30 μm).....	51
3.24. Coating Young's Modulus and curvature effects on delamination sizes (Specimen Radius = 700 μm , σ_r (Residual Stresses) = 0 GPa, Coating thickness = 30 μm , Indentation Loading = 133 N)	52
3.25. Residual stresses effects on loading vs. displacement curves ($E = 1200 \text{ GPa}$, Sample Curvature = 700 μm , Coating thickness = 30 μm , Indentation Depth = 10 μm)	54
3.26. Residual stresses effects on delamination sizes ($E = 1200 \text{ GPa}$, Sample Curvature = 700 μm , Coating thickness = 30 μm , Indentation Depth = 10 μm).....	54
3.27. Coating thickness effects on delamination sizes ($E = 1200 \text{ GPa}$, Sample Curvature = 700 μm , Indentation Depth = 10 μm , σ_r (Residual Stresses) = 0GPa)	55
3.28. Residual stresses and curvature combined effects on the critical loading ($E = 1200 \text{ GPa}$, Coating thickness = 30 μm)	56
4.1. (a) Section dimensions and (b) external shape dimensions of end mill	62
4.2. Different types of end mills: (a) square end end mill, (b) corner chamfer end mill, (c) corner radius end mill, (d) ball nose end mill, and (e) corner rounding end mill	65
4.3. (a) a completed end mill solid model and (b) a diamond-coated end mill	67
4.4. Mesh distributions on a diamond-coated macro end mill: (a) whole model (b) around head	68
4.5. Longitudinal stress distributions in a diamond-coated macro end mill (a) entire end mill (b) around end mill head.....	69
4.6. 2D cross section of an end mill for FEA: (a) sectional plane specification and workpiece plane view#1, (b) sectional plane specification and workpiece plane view#2, (c) highlighted cross section area, and (d) extracted 2D cross section	71
4.7. Maximum principal stress contour of a 2D diamond-coated macro end	

mill cross section (a) entire model (b) around the cutting edge.....	72
4.8. End mills with different helix angles (a) 15° (b) 30° (c) 45°	73
4.9. Edge radius effect on interface stresses of 2D diamond-coated macro end mills (a) radial normal stresses (b) circumferential stresses (helical angle = 30° and coating thickness = 5µm).....	74
4.10. Coating thickness effect on interface stresses of 2D diamond-coated macro end mills (a) radial normal stresses (b) circumferential stresses (r_e (edge radius) = 15µm and helical angle = 30°).....	74
4.11. (a) a micro end mill substrate and (b) a diamond-coated micro end mill.....	77
4.12. Longitudinal stress distributions in a diamond-coated micro end mill (a) around end mill head (b) sectional view.....	78
4.13. Maximum principal stress contours in a 2D diamond-coated micro end mill cross section (a) entire model (b) around the cutting edge	80
4.14. Edge radius effect on the interface stresses of diamond-coated micro/macro end mills (a) radial normal stresses of micro end mills, (b) circumferential stresses of micro end mills, (c) radial normal stresses of macro end mills, and (d) circumferential stresses of macro end mills.....	81
4.15. Maximum principal stress contours in a 2D diamond-coated macro end mill cross section with the inclusion of a cohesive zone model (a) entire model, (b) around the cutting edge, (c) normal tractions at the interface, and (d) normal separations at the interface ($r_e = 7 \mu\text{m}$, coating thickness = 5 µm and helix angle = 30°).....	83
4.16. Edge radius effect on interface stresses of 2D diamond-coated macro end mills with the inclusion of a CZM (a) radial normal stress (b) circumferential stress (coating thickness = 5 µm and helix angle = 30°).....	84
4.17. Coating thickness effect on interface stresses of 2D diamond-coated macro end mills with the inclusion of a CZM (a) radial normal stress (b) circumferential stress ($r_e = 15 \mu\text{m}$ and helix angle = 30°)	84

CHAPTER 1

INTRODUCTION

Background and Motivation

With the development of surface engineering technologies, diamond-coated tools have been widely studied for tooling applications in machining high silicon aluminum alloys, copper alloys, metal-matrix composites, nonferrous metals, ceramics, fiber-reinforced plastics, and graphite. Due to their excellent tribological and mechanical properties, diamond-coated tools have been considered as an alternative to the synthetic polycrystalline diamond (PCD) tools. With regard to the manufacturing of PCD tools, they are fabricated by distributing micrometer-sized diamond grains in a metal matrix. The tool tip is made by pressing, sintering, and brazing to a shank of cemented carbide. However, fabricating and processing of PCD tools are high costly. On the other hand, chemical vapor deposition (CVD) of diamond films has been widely explored for cutting tool applications.

Due to the abrasive nature of the reinforced phase in metal matrix composites (MMC), machinability is poor and tool wear is rapid when using conventional tools. Thus, diamond-coated tools, with their economical viability, superior mechanical properties, and tribological behavior, are better suited for MMC machining. Under such conditions, Chou and Liu (2005) conducted a study of the CVD diamond tool performance in MMC machining. The tool wear was measured and compared under different machining conditions. The authors of this paper concluded that the cutting speed and the feed affect the tool wear, and coating failure due to high stresses is the dominant wear mechanism, which suggested that the tool performance is strongly

affected by the bonding between the coating and substrate. Because of the different thermal expansions between the coating and substrate, a significant interfacial stress is induced at the bonding surface.

Later, Hu and Chou (2007) applied finite element analysis (FEA) to study the stress distributions in diamond coating tools. The major finding in this study showed that increasing the edge radius reduces the maximum radial normal stress as well as the tangential stress. Radial normal stress and tangential stress are the stress components after the Cartesian coordinate system is changed to the local polar coordinate system.

Besides numerical studies of diamond-coated cutting tools, experiments have also been conducted to compare nano-crystalline diamond (NCD) coating tools, conventional microcrystalline diamond coating (MCD), and PCD tools regarding surface topography, grain sizes, carbon bonds, and mechanical properties (Hu et al., 2007). The diamond tools were characterized and were evaluated while machining an Al-matrix composite and a high-strength aluminum (Al) alloy. The study (Hu et al., 2007) indicated that coating delamination is the major tool wear mechanism leading to catastrophic tool failures.

Since diamond-coated tools have been increasingly used for machining advanced materials, Hu, Chou, and Thompson (2008) evaluated nanocrystalline diamond (NCD) coating tools in machining a high-strength Al alloy. The study demonstrated that catastrophic failures are affected by cutting speeds, and at a high feed rate, coating delamination is even propagated to rake face.

It has been widely reported and found that diamond coating tool performance in machining is limited by interface delamination. Hence, Hu et al. (2008) conducted a numerical study of the interface behavior of diamond-coated cutting tools. This study incorporated the

cohesive zone model (CZM) to characterize the interface behavior between the coating and the substrate. Also, a finite element code was applied to simulate the indentation process and interface delamination. The results of this study showed that (1) due to the delay of substrate yielding, increasing the coating Young's Modulus reduces the delamination size, (2) the delamination size marginally increases with the increase of coating residual stresses (compressive), and (3) thicker coatings have greater resistance to the interface delamination.

The functions and parameters describing the properties of the CZM vary from model to model, and the cohesive zone studies can be dated back to the mid-20th century. Barenblatt (1959, 1962) initiated the study of the CZM as a possible alternative to the concept of fracture mechanics in perfectly brittle materials. Figure 1.1 describes the cohesive zone response under loading.

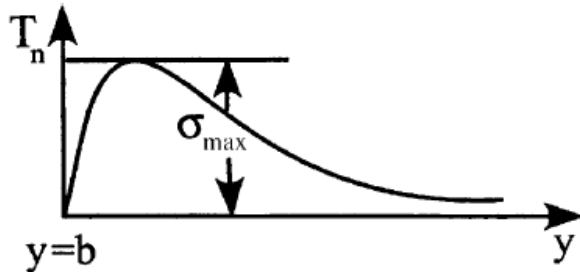


Figure 1.1. First proposed cohesive zone concept (Barenblatt, 1959, 1962).

Geubelle and Baylor (1998) simulated the delamination process in thin composite plates using a 2D cohesive finite element scheme, which introduced the cohesive elements along the boundaries of the inner layers and inside the transverse plies to simulate the spontaneous initiation and propagation of transverse matrix cracks. Figure 1.2 describes the cohesive zone model proposed by Geubelle and Baylor.

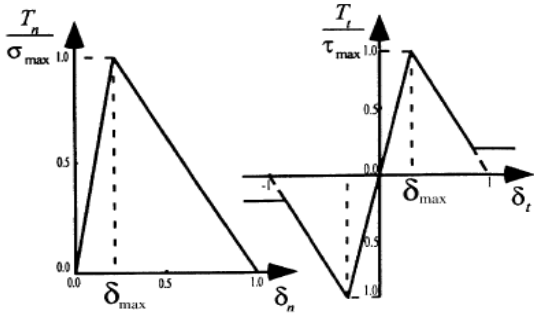


Figure 1.2. Bilinear cohesive zone model (Geubelle & Baylor, 1998).

Renaud et al. (2009) conducted a 3D simulation of residual stresses developed in diamond-coated tools, and the results showed that (1) the cutting edge radius is the most significant factor, and (2) for a 5 μm edge radius insert, the radial and circumferential normal stresses are about 1.5 GPa in tension and 3.7 GPa in compression, respectively. Figure 1.3 (a) illustrates the stress distribution along the cutting tip and Figure 1.3 (b) plots the interfacial stresses around the cutting edge. It is noted that high stresses are concentrated at the edge rounding area.

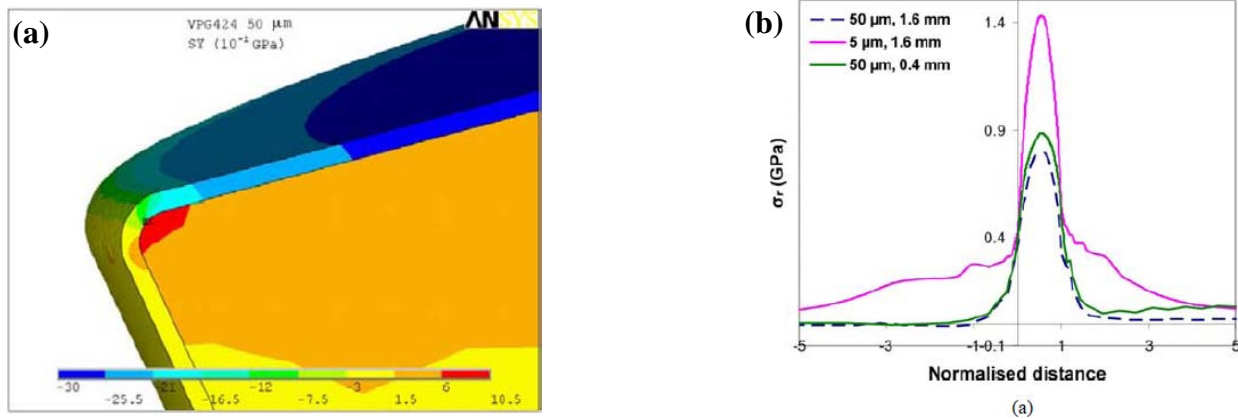


Figure 1.3. (a) Stress distribution around the cutting tool edge (b) Edge radius effects on interfacial radial normal stresses (Renaud et al., 2009).

Following the work of Renaud et al., Qin et al. (2009) employed a 3D FEA to investigate diamond-coated tungsten carbide cutting inserts with different edge radii because the cutting edge geometry has compound effects on diamond-coated tools, and edge radius affects the

deposition stresses and machining loads in an opposite way. The results of this study showed that (1) with increasing of the edge radius, the deposition residual stresses decrease significantly, (2) cutting forces increase with the increase of the edge radius; however, the increasing rate decreases at a higher feed, and (3) the combined effects cause complex wear behavior of diamond-coated tools with different edge radii.

Besides the edge radius, coating thickness effects on depositional residual stresses were also investigated. Qin et al. (2009) conducted a study of coating thickness effects on the deposition residual stresses, particularly around a cutting edge. Coating failure modes were investigated numerically as well. The results showed that increasing the coating thickness increases the residual stresses at the coating–substrate interface. On the other hand, increasing the coating thickness will generally increase the resistance of coating cracking and delamination.

While there are plenty of papers discussing the mechanical properties and tribological behavior of diamond-coated tools, few studies have been found to properly address diamond coating tools' interfacial delamination. Additionally, almost no study has focused on studying the curvature effect on interfacial delamination. Similarly, little attention has been emphasized to the residual stresses developed in diamond-coated cutting tools with complicated geometry, such as twist drills and end mills, and the effects of their geometry on the magnitude of deposition residual stresses, even though the deposition residual stresses generated by the thermal expansion mismatch are critical to their machining performance. With regard to the residual stresses developed in diamond-coated cutting tools, few studies have included cohesive zone models.

Research Objectives and Scope

This research focused on investigating the thermal-mechanical and the interface behavior of conventional diamond-coated cutting tools, such as inserts, drills, and end mills. Since this

research discussed various aspects of diamond-coated cutting tools, each of the subsequent chapters formed an independent paper. Thus, their specific objectives were listed below:

1. To develop a 3D modeling technique, and investigate the residual stresses of diamond-coated drills with 2D and 3D finite element analysis (FEA).
2. To evaluate the interfacial failure of diamond-coated tools under the indentation by developing a numerical method.
3. To develop a 3D modeling technique, study the deposition residual stresses of diamond-coated macro/micro end mills with 2D and 3D FEA, and investigate the cohesive zone effects on interface stresses.

The diamond-coated drills were designed by applying 3D CAD modeling methodologies. 2D/3D FEA were applied to investigate the geometric parameter effects on the residual stresses during deposition process. Since the depositional residual stresses affect the coating-substrate adhesion quality, and interface delamination limits diamond-coated tool performance, indentation based simulations incorporating a cohesive zone model has been developed to analyze the interface behavior under the contact loading. Coating attribute, residual stresses as well as curvature effects on interface delamination have been discussed. Besides, 3D CAD modeling methodologies have been extended to design diamond-coated macro/micro end mills, and 2D/3D FEA have been applied to investigate the end mill geometric parameter as well as size effects on depositional residual stresses. A cohesive zone model has also been incorporated into the macro end mill 2D cross-section to study its effect on interface stresses.

Organization of the Thesis

Chapter 1 presents the background, motivation and research objectives of this thesis.

Chapter 2 develops a 3D modeling technique for the diamond-coated drill. 2D/3D finite element analysis is conducted on diamond-coated drill to investigate the deposition-induced residual stresses. With regard to the 2D cross-section FEA, the geometric parameter effects, such as point angle, helical angle, and web-thickness etc., are studied, discussed, and compared.

Chapter 3 presents finite element methods to numerically investigate the interface behavior of diamond-coated tools under indentation with spherical and wedge indenters. In this chapter, a cohesive zone model characterized by traction-separation law is proposed to simulate interface delamination under the indentation. The coating attribute, residual stresses, and the curvature effects on interface delamination are studied.

Chapter 4 develops 3D modeling techniques of diamond-coated macro/micro end mills. 2D/3D FEA are conducted on diamond-coated macro end mills to investigate the deposition-induced residual stresses. The same methodologies are repeated on the diamond-coated micro end mills to investigate interface stresses. In addition to the FEA of 2D cross-sections of rigid contact models, cohesive zone models are incorporated into the 2D macro end mill cross-sections to characterize their interface behavior. The geometric parameter effects, such as helix angle, edge radius, and coating thickness etc., are studied, discussed, and compared.

Chapter 5 provides the summary, major contributions and future recommendations of this thesis.

CHAPTER 2

INTEGRATED DESIGN AND ANALYSIS OF DIAMOND-COATED DRILLS

Abstract

The objective of this chapter is to investigate the drill geometry effects on the deposition residual stresses in diamond coated carbide drills, especially the interface stresses. The approaches include (1) solid modeling of diamond-coated two-flute twist drills using commercial computer-aided design (CAD) software, and (2) finite element analysis (FEA) to simulate residual stresses in a diamond-coated drill, which are generated during the deposition process as a result of the mismatched thermal expansion coefficients. It is noted that the residual stresses generated by deposition in diamond-coated drills can be significant, on the order of GPa. The modeling methodology is employed to design drills of different geometries. Further, to compare interface stresses around the cutting edge, 2D FEA is applied to simulate residual stresses of the drill cross-sections, and the interface stress data at the drill cutting edge is manipulated to quantitatively evaluate the drill geometry effects. The major results are summarized as follows: (1) the micro-level geometry such as the edge radius has the most dominant effects on the interface stresses, (2) in particular, the radial normal stresses can become largely tensile, over 1.0 GPa, which may affect the coating adhesion integrity, and (3) changing the macro-level geometry such as the helix angle, point angle, and web-thickness will affect the wedge angle, 10° to 20° difference, at the drill tip. However, the effects on the interface stress magnitudes are rather minor.

Introduction

Drilling is among the most difficult machining processes because of chip-flow restrictions, poor heat dissipation, and rapid wear, which severely limits its productivity. Drilling constitutes about 40% of all metal-cutting operations (Hamade & Ismail, 2005), and 50% to 70% of all production time is spent on making holes (Benes, 2000). Twist drills used for hole making have one of the most complex shapes in machining tooling. A standard two-flute twist drill has a configuration as shown in Figure 2.1(a), which includes spiral flutes running along a cylindrical body and the point (drill tip) area. Drill geometry studies can be dated back to the mid-20th century. Several research groups developed drill models to formulate mathematical equations describing the drill geometry, some relying on computer software to generate the drill model. Galloway (1957) pioneered the drill geometry research with the focus on the drilling process mechanics. The author developed analytical equations relating the point shape of a two-flute twist drill to the geometry of the grinding cone used to generate the flute shape and tip area. Fujii et al. (1970) developed a method to create a drill by using CAD software. In their work, the orthogonal and oblique cutting planes were defined to conduct the geometric analysis of the drill point, and the cutting angles were also defined. Drills have a complex geometry, and designing an accurate drill tool based on the actual manufacturing parameters presents a challenge. Tsai and Wu (1979) presented the formula describing the ellipsoidal and hyperboloidal drills in addition to the conventional drills. Further, the grinding parameter effects on the cutting angles were studied. Ehmann (1990) introduced an approach for the inverse problem in the manufacture of drill flutes and developed the analytical equation to form the grinding wheel profile used to generate the flute cross-section. The comparison between the analytical results and actual measured cutting angles of drill samples indicated that the average error was less than 5%. Ren

and Ni (1999) studied both the drill cutting angles and the flute surface models. They developed a new mathematical model to describe the drill flute and the drill flank face with a quadratic model based on the grinding parameters. Drill angles in a two-flute drill and its grinding parameters were related via vector analysis. Shyu (2002) performed FEA simulations of the drilling process and developed drill meshing. Choi et al. (2003) created an applet to generate the meshing of multi-flute drills. Vijayaraghavan and Dornfeld (2004) developed a modeling algorithm for two-flute twist drills based on CAD software. Their work ensures that the models created are practical usage for subsequent finite element simulations of the drilling process. Their drill CAD models are defined based on the actual fabrication processes.

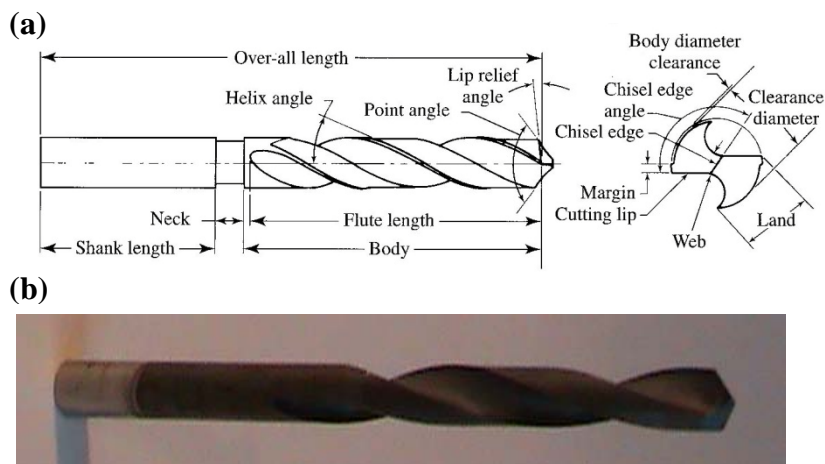


Figure 2.1. (a) Configuration of a standard two-flute twist drill (Stephenson & Agapiou, 1996) and (b) an actual twist drill.

Recently, diamond coatings using chemical vapor deposition (CVD) technologies have been applied as tooling applications to enhance machining performance. Cutting tools coated with diamond, $5\mu\text{m}$ to $30\mu\text{m}$, can have a tool life over 50 times longer than uncoated plain tungsten-carbide (WC) tools (Oles, Inspektor & Bauer, 1996). One of the challenges in coating diamond on carbide tooling is residual stresses generated in the tool after depositions due to the largely mismatched thermal expansion coefficients between diamond and carbide (Hu, Chou &

Thompson, 2007). The deposition residual stresses affect the adhesion quality of the diamond film and impact the cutting tool life which is mostly limited by coating delamination (Hu, Chou & Thompson, 2008). Diamond-coated drills have a potential for high performance drilling for difficult-to-machine materials. Applying diamond coating on complex-shaped tooling such as drills has also been attempted, however, few studies have been reported (Chen et al., 2002). Moreover, deposition residual stresses in diamond-coated carbide drills have not been investigated before. It is also known that around any geometric changes, stress distributions will be altered and stress concentration can be significant around the substrate edge compared to the uniform coating area. Since drills have a very complex shape, drill geometry is expected to have strong interactions with the deposition stresses. To effectively use diamond-coated drills, it is necessary to integrate the design and stress analysis from the drill geometry aspect.

In this study, a method to generate diamond-coated two-flute twist drills is developed using commercial CAD software. FEA software is further applied to simulate 3D deposition residual stresses in a diamond-coated drill. Further, 2D FEA stress simulations of drill cross-sections at the cutting edge, at different locations, are approximated to obtain stress distributions around the cutting edge which can be extracted and transformed to quantitatively evaluate local interface stresses of different components. The solid modeling methodology is also employed to develop drill models with different geometry parameters such as the helix angle, point angle, and web thickness, and the models are further used for 2D residual stress simulations. Therefore, drill geometry effects including the cutting edge radius on the deposition stresses are quantified.

Solid Modeling of 3D Diamond-Coated Two Flute Twist Drills

Solid modeling of a twist drill consists of several procedures. With Solidworks used in this study, first, a helix curve with a specified helix angle (later serving as the sweep trajectory)

is defined. Then, the spline curve of the flute cross-section is constructed according to the mathematical representation of specific drill geometry (Vijayaraghavan & Dornfeld, 2004). Once the flute cross-section (spline as well as the circular portion) is completed, the sweeping function is used to create the drill flute body. Next, the left and right grinding cones are defined to mimic the fabrication process generating the drill tip: two cutting lips and a chisel edge. Finally, an edge radius is incorporated along the cutting lips and chisel edge. The description of modeling processes can be found in Appendix A.

In order to model diamond-coated drills, the drill model developed above serves as the substrate, and revolve-cut and shell functions are employed to generate the coating with a given coating thickness and an edge radius. The completed drill substrate and coating models can then be assembled, assuming a rigid interface, to obtain a diamond-coated twist drill. Figure 2.2 shows an example of solid models of a twist drill body and a diamond-coated drill.

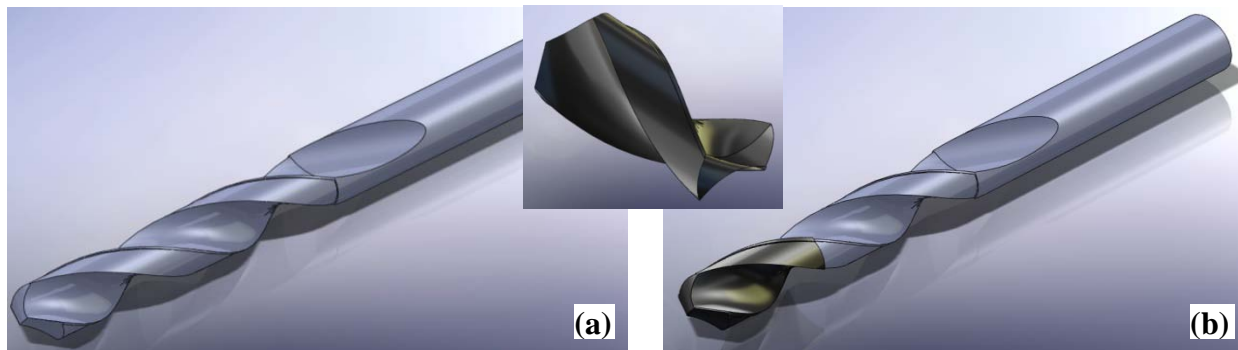


Figure 2.2. An example of (a) fully defined twist drill solid model and (b) diamond-coated twist drill.

Finite Element Analysis of Deposition Stresses

3D Drill Stress Analysis

Due to the mismatched thermal expansions between the drill substrate (WC) and coating (diamond), residual stresses will be developed in the diamond-coated drill when the deposition process is completed and the drill is returned to room temperature. To conduct 3D deposition-

stress simulations, the drill substrate and coating model files from Solidworks are imported into the FEA software, ABAQUS, for assembly and merging. Meshing is then performed using the element type C3D4 free Tet elements, and the coating area receives finer meshing. For the meshed model, the cutting-lip and chisel edge areas are further refined, as shown in Figure 2.3 below, as high stress gradients can be expected. Moreover, the material properties for the substrate material, WC, are 620 GPa for Young's modulus, 0.22 for Poisson's ratio, and $5.5 \mu\text{m}/(\text{m.K})$ for thermal expansion coefficient. For diamond coatings, the Young's Modulus is 1200 GPa, Poisson's ratio is 0.07, and the thermal expansion coefficient is $2.5 \mu\text{m}/(\text{m.K})$. For the stress simulations, static structural analysis is conducted and a deposition temperature of 800°C is set as the initial condition, and the room temperature of 25°C is defined as the final temperature. Material behaviors of both WC and diamond are assumed to be elastic due to their high melting points and brittleness. Thus, the coating-substrate interface is considered to be rigid. The boundary condition includes an axially constrained surface at the drill bottom.

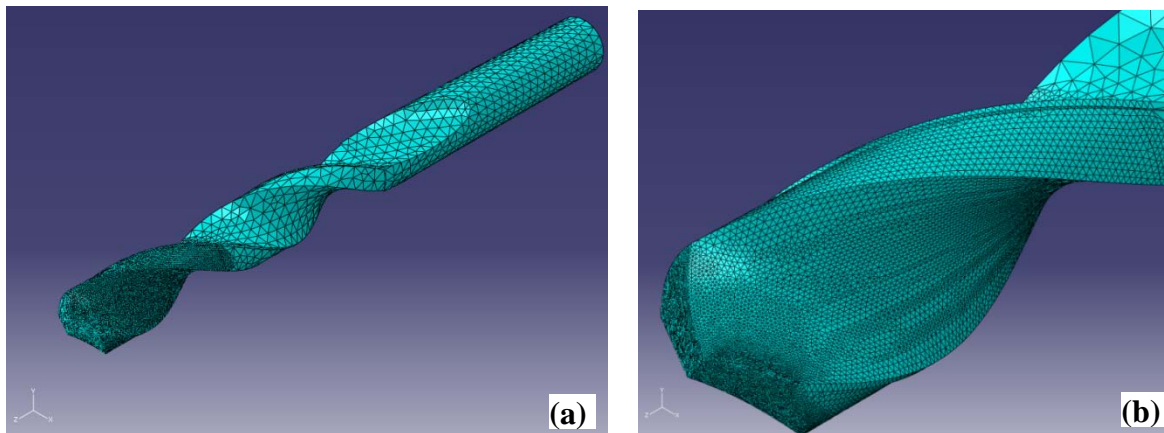


Figure 2.3. Element meshing for diamond-coated drill stress simulations: (a) the entire drill model and (b) around drill tip.

For illustration purposes, a stress analysis example from a diamond-coated drill with 6.34 mm diameter, 34.5 mm flute length, 30° helix angle, 135° point angle, 1.33 mm web-thickness, and $3 \mu\text{m}$ edge radius is given below. The length of the coating area along the longitudinal

direction is 12.7 mm. Figure 2.4 shows the stress contours (longitudinal normal stress) of the coated drill. It is noted that on the coating surface with moderate curving, the longitudinal stress is in the neighborhood of 3.0 GPa in compression. This is consistent with the results obtained from the biaxial stress analysis. On the other hand, the substrate has tensile stresses, on the order of 100 MPa, and is generally small in the area away from the coating area. It is further noted that around the drill tip, large stress gradients are prominent. Figure 2.5 plots the longitudinal stress in the sectional view of a coated drill to illustrate high stress concentrations near the drill tip, especially around the cutting edge.

It is known that interface stresses (between the coating and substrate) are more closely related to the coating integrity. Thus, it was intended to obtain the stress data along the interface. However, this is a complex and time-consuming process for the 3D drill model. Thus, a 2D approximation of stress analysis, described next, was applied to attain the interface stress data for further evaluations and investigation of drill geometry effects.

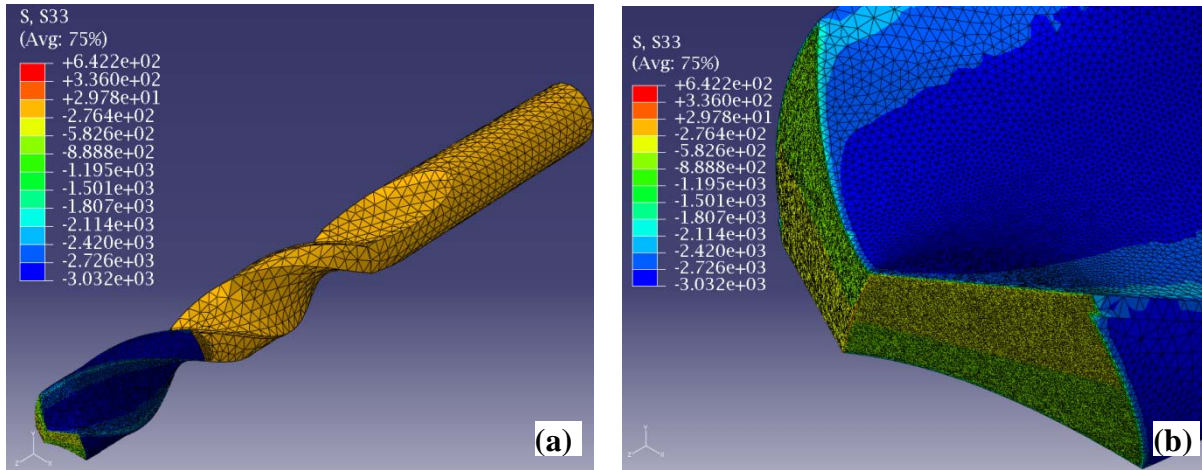


Figure 2.4. An example of stress distributions (longitudinal normal stress) in a diamond-coated drill: (a) overall and (b) near drill tip.

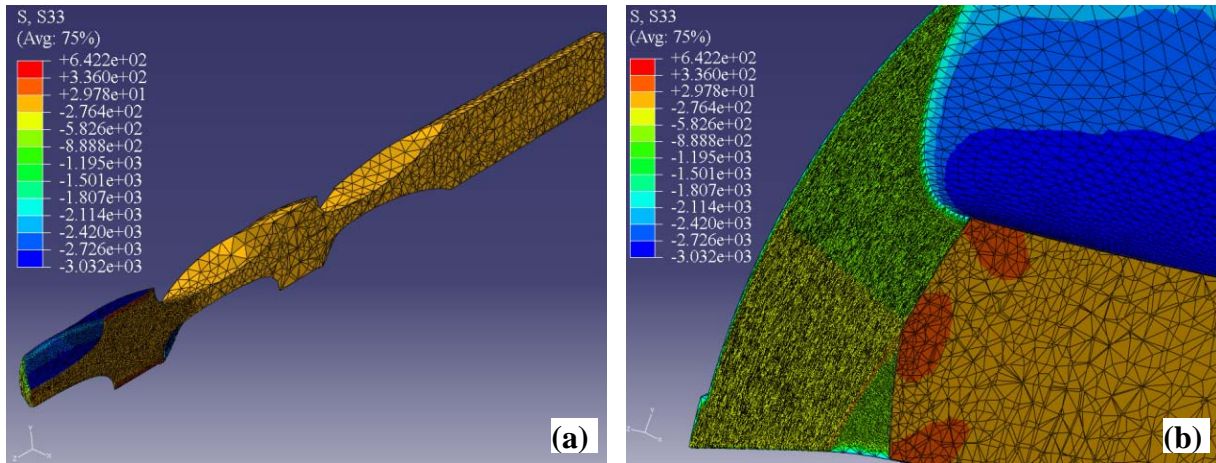


Figure 2.5. Longitudinal normal stress contours in a sectional view of a diamond-coated drill: (a) overall and (b) near drill tip.

2D Approximation

In order to evaluate the drill geometry effects on the interface stresses of a diamond-coated drill, 2D drill cross-sections around the drill tip were generated at different locations, both the cutting lip and chisel edge, using a plane normal to the cutting edge. Figure 2.6 shows an example of a 2D drill section being generated.

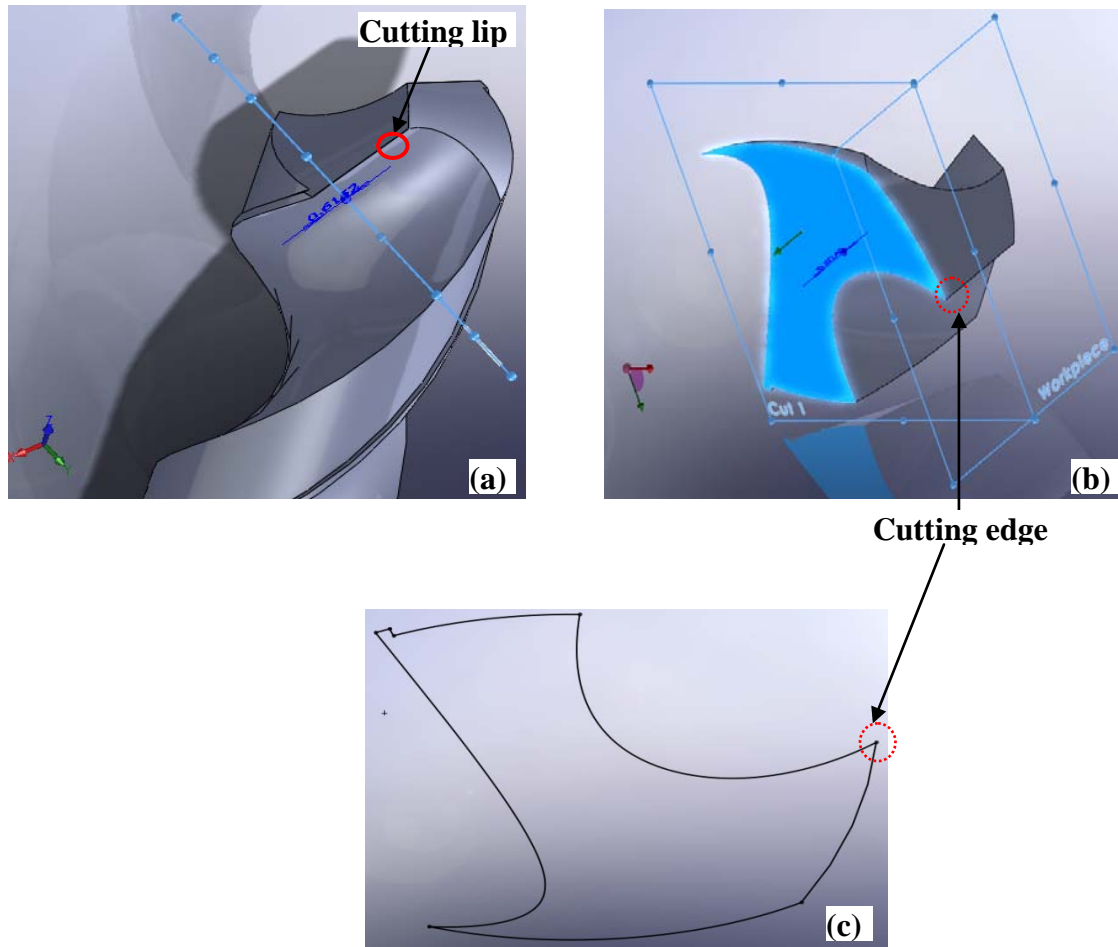


Figure 2.6. An example of 2D section of a drill for FEA stress analysis: (a) Sectional plane specification, (b) Intersected profile on the drill, and (c) 2D view of the cross-section.

Considering the relative motion at the local drill edge (i.e., rotation, as in actual drill operation), a workpiece plane can be defined, Figure 2.6(b), to evaluate the cutting geometry such as the rake angle. As seen from Figure 2.6(b), the highlighted area is the cross-section, and the two planes represent the sectional and workpiece planes. In this particular cross-section, which is about 1 mm away from the outer diameter, the rake and relief angles are 30.11° and 5.8° , respectively. The cross-section profile can then be extracted and exported to ABAQUS. With the addition of a specified edge radius and a uniform coating layer, 2D FEA simulations of deposition stresses are conducted, with an assumption of 2D plane strain. The material properties and the deposition temperature are the same as in the 3D analysis. The boundary

conditions applied include one fully constraint corner (away from the cutting edge) and another partially constrained (one direction) point.

As an example, Figure 2.7 shows the maximum principal stress contours in the studied cross-section. This example is from a diamond-coated drill: 6.34 mm diameter, 34.5 mm flute length, 30° helix angle, 135° point angle, 1.33 mm web-thickness, and 3 μm edge radius. The coating is 5 μm thick. The cross-section is on the cutting lip, about 1 mm away from the outer diameter. The stresses range from 2 GPa to 3 GPa. Though the stress distribution is uniform in most areas, the area around the coating-substrate interface, particularly near the cutting edge, has high stress gradients, as shown in Figure 2.7(b).

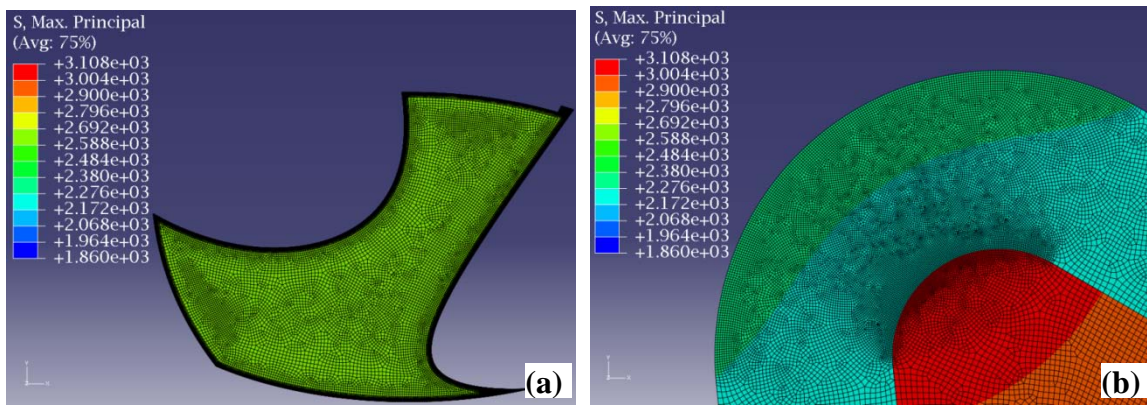


Figure 2.7. Deposition stress contours (maximum principal stress) in a 2D coated-drill section: (a) overall distribution and (b) around the cutting edge area.

In order to quantify the interface stresses around the cutting edges, the stress data along the interface of 2D results is extracted and stress transformation is conducted using the Mohr's circle concept. The stresses in the Cartesian coordinate system in FEA are changed to stress components associated with the local polar coordinate system around the cutting edge, including 3 components, namely, the radial normal stress (σ_r), the circumferential normal stress (σ_θ), and the shear stress ($\tau_{r\theta}$). Figure 2.8(a) illustrates the 3 stress components around the cutting edge,

noting that they vary along the rounded curve and can be evaluated in reference to a point where the rounded edge begins.

Figure 2.8(b) plots the interface stress profiles, all 3 components, for the example illustrated above. The stresses are at the coating-substrate interface and plotted around the edge (coordinate 0 is where the edge curve starts). The abscissa in the figure is the distance normalized by the arc length of the rounded edge (Figure 2.8(a)). It can be seen that tensile radial normal stresses, as high as close to 1.5 GPa, are developed because of the edge sharpness. Such high tensile stresses can be detrimental in brittle fracture due to crack propagations and require greater adhesion strengths. On the other hand, the circumferential stresses are in the neighborhood of 3 GPa in compression. The large compressive tangential stresses have been viewed to be beneficial for abrasive wear rate reductions; however, buckling could be another mechanism risky to the coating failure (Gahlin, Alahelisten, & Jacobson, 1996). The shear stresses are in the range of ± 0.6 GPa.

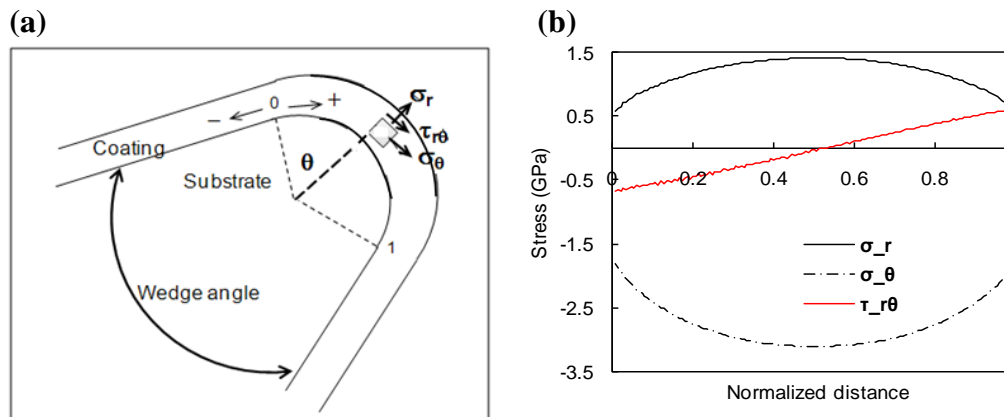


Figure 2.8. (a) A schematic drawing showing the interfacial stress components around the edge area, and (b) Interface stress profiles around the cutting edge of a diamond-coated drill cross-section.

Drill Geometry Effects

Using the developed modeling methodology, CAD is applied to design twist drills with different geometries. Among drill geometry parameters, the helix angle, the point angle, and the

web thickness are considered as the major parameters to be investigated (Stephenson & Agapiou, 1996). These parameters affect the cutting geometry, mainly the rake angle, and thus, the drilling process. In addition, the wedge angle changed may possibly affect the deposition stresses, the studied subject of this paper. In this study, the helix angles tested were 20° , 30° , and 40° , and the point angles included 90° , 118° , and 135° . The web-thicknesses changed from 0.64 mm, to 1.3 mm and 1.9 mm. Figure 2.9 and Figure 2.10 are examples of twist drills with different helix and point angles, respectively. Moreover, the micro-level of drill geometry, namely, cutting edge radius, is investigated as well. Three levels of edge radii were simulated: $3\ \mu\text{m}$, $7\ \mu\text{m}$, and $15\ \mu\text{m}$.

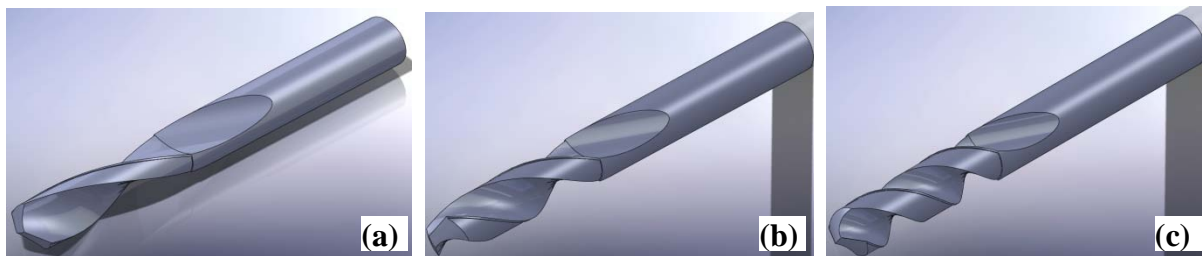


Figure 2.9. Drills with different helix angles: (a) 20° , (b) 30° , and (c) 40° .

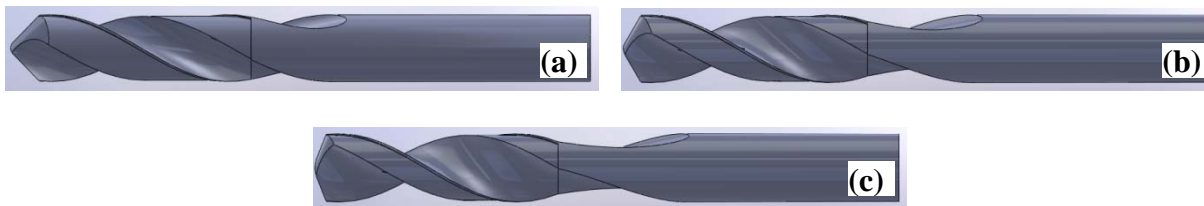


Figure 2.10. Drills with different point angles: (a) 90° , (b) 118° , and (c) 135° .

Applying the same procedures defined earlier, different 2D cross-sections along the drill cutting lip and chisel edge, at 3 different locations (See Figure 2.11), are obtained for further stress analysis. The wedge angle of each section is also evaluated and compared between different types of drills. Table 2.1 lists the wedge angles for different cross-sections of drills with different helix and point angles.

Table 2.1

Wedge Angle ($^{\circ}$) at Different Sections of Drills with Different Point and Helix Angles

<i>Point angle ($^{\circ}$)</i>	<i>Sec. 1</i>	<i>Sec. 2</i>	<i>Chisel Sec.</i>	<i>Helix angle ($^{\circ}$)</i>	<i>Sec. 1</i>	<i>Sec. 2</i>	<i>Chisel Sec.</i>
90	47	53	90	20	65	68	113
118	54	59	114	30	54	59	113
135	57	61	129	40	43	49	113

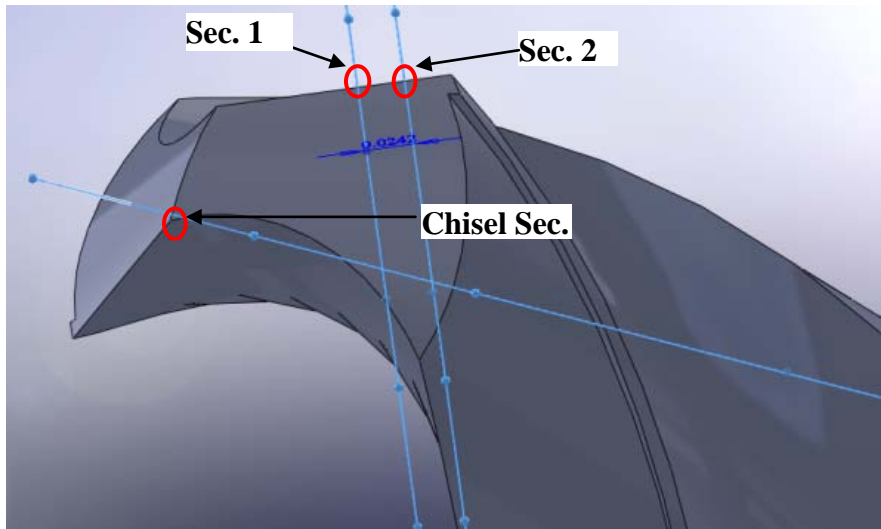


Figure 2.11. Locations of different drill cross-sections analyzed in Table 2.1.

Further, a layer of diamond coating with a given thickness is added to the drill cross-section, uniformly all around. Then, FEA deposition stress analysis is conducted to all generated diamond-coated sections according to the simulations specified earlier. Then, the stress data along the interface is extracted and transformed to evaluate the interface stress profiles. Figure 2.12 shows the helix angle effects on the radial normal stresses. It is noted that the radial normal stresses are virtually not affected by the helix angle. Note that the wedge angle, formed by the

rake and relief angles, changed due to different helix angles, is fairly noticeable, 10° to 20° differences, but the effect on the deposition stresses is little. On the other hand, Figure 2.13 plots the normal stress components affected by the drill cutting edge radius. It is clearly noted that the edge radius (r_e) significantly modifies the deposition interface stresses. For the radial normal stress (σ_r), the maximum reduces from 1.4 GPa for $3 \mu\text{m}$ r_e to 0.7 GPa for $15 \mu\text{m}$ r_e . The large edge radius also shows smooth stress gradients along the edge. For the circumferential normal stress (σ_θ), stress reductions by the edge hone are from -3.0 GPa for $3 \mu\text{m}$ r_e to -2.7 GPa for $15 \mu\text{m}$ r_e . For the shear stress component ($\tau_{r\theta}$), the stress magnitude is smaller and reductions at a large radius are also evident: from ~ 0.7 GPa for $3 \mu\text{m}$ r_e to ~ 0.3 GPa for $15 \mu\text{m}$ r_e .

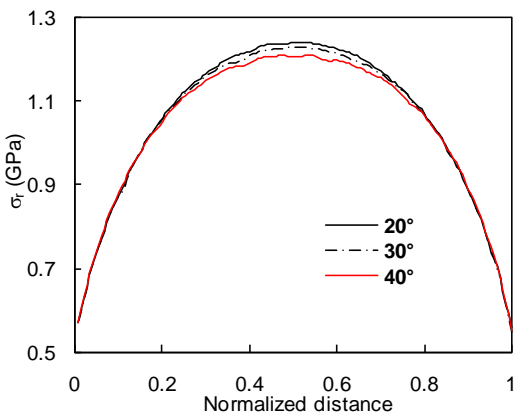


Figure 2.12. Interface stress profiles, radial normal component, for drills of different helix angles.

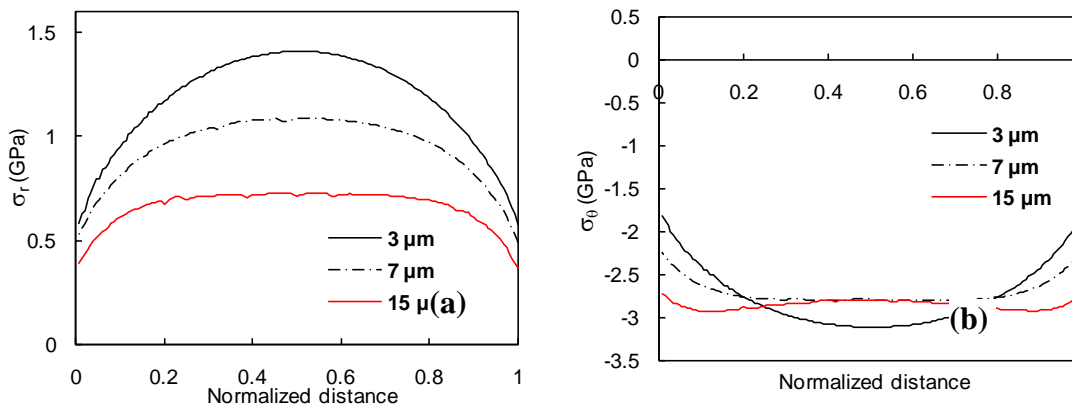


Figure 2.13. Edge radius effects on interface stress profiles of diamond-coated drills: (a) radial normal stress, and (b) circumferential normal stress.

In order to reach quantitative conclusions, the maximum values of stress magnitudes of all 3 components are obtained to examine the drill parameter effects studied. Table 2.2, Table 2.3, Table 2.4, and Table 2.5 compare the edge radius, helix angle, point angle, and web-thickness effects, respectively, on the maximum interface stresses by deposition. It is clear that the smallest edge radius drill, i.e., 3 μm , has the largest σ_{rmax} and $\sigma_{\theta\text{max}}$, 1.41 GPa and 3.11 GPa, respectively. For the drill with 15 μm edge radius, it has the $\sigma_{\text{rmax}} = 0.73$ GPa and $\sigma_{\theta\text{max}} = 2.94$ GPa, respectively. On the other hand, the macro-level parameters of drill geometry do not affect the deposition stress magnitudes.

Table 2.2

Maximum Interface Normal Stresses for Different Edge Radii

<i>Edge Radius (μm)</i>	<i>3 μm</i>	<i>7 μm</i>	<i>15 μm</i>
σ_{rmax} (GPa)	1.41	1.08	0.73
$\sigma_{\theta\text{max}}$ (GPa)	3.11	2.80	2.94

Table 2.3.

Maximum Interface Normal Stresses for Different Helix Angles

<i>Helical angle ($^{\circ}$)</i>	<i>20</i>	<i>30</i>	<i>40</i>
σ_{rmax} (GPa)	1.24	1.23	1.21
$\sigma_{\theta\text{max}}$ (GPa)	3.05	2.89	2.73

Table 2.4

Maximum Interface Normal Stresses for Different Point Angles

<i>Point angle (°)</i>	<i>90</i>	<i>118</i>	<i>135</i>
σ_{rmax} (GPa)	1.217	1.227	1.234
$\sigma_{\theta max}$ (GPa)	2.78	2.89	2.94

Table 2.5

Maximum Interface Normal Stresses for Different Web Thicknesses

<i>Web thickness</i>	<i>0.635</i>	<i>1.33</i>	<i>1.91</i>
<i>(mm)</i>			
σ_{rmax} (GPa)	1.22	1.23	1.23
$\sigma_{\theta max}$ (GPa)	2.85	2.89	2.92

Conclusions

Solid modeling of diamond-coated drills using CAD software has been achieved in this study. 3D FEA simulations have been developed as well to study deposition residual stresses in a diamond coated drill. The nominal longitudinal normal stresses in the area of less curvature are about 3 GPa in compression, which is consistent with the biaxial stress analysis. The model can be used to design drills with different geometric parameters. Moreover, 2D approximation of FEA stress simulations is applied to investigate drill geometry effects on interface stresses around the drill cutting edge. The residual stresses generated by deposition in the diamond-coated drills can be significant. The micro-level geometry, such as the edge radius, has the most dominant effects on the interface stresses. In particular, the radial normal stresses can become

largely tensile, over 1.0 GPa, which may affect the adhesion integrity. Changing the macro-level geometry such as the helix angle, point angle, and web-thickness will affect the wedge angle, 10° to 20° difference, at the cutting tip. However, the effects on the interface stress magnitudes are rather minor.

For future work, the coating thickness effects on the interface residual stresses in diamond coated drills will be incorporated. Moreover, during machining, the deposition residual stresses will be affected by the induced mechanical and thermal loads. Thus, it is necessary to concurrently investigate the stress field evolutions during drilling in order to effectively use diamond coated drills.

Acknowledgments

The research is supported by NSF Grant No: IIP 0741028 and CMMI 0728228.

References

- Benes, J. (2000). Hole making trends run deep, fast, and dry. *American Machinist*, 97 – 102.
- Chen, M., Jian, X. G., Sun, F. H., Hu, B., & Liu, X. S. (2002). Development of diamond-coated drills and their cutting performance. *Journal of Materials Processing Technology*, 129, 81-85.
- Choi, J., Min, S., Dornfeld, D. A., Alam, M., & Tzong, T. (2003). Modeling of inter-layer gap formation in drilling of a multilayered material. *Proceeding of 6th CIRP International Workshop on Modeling of Machining Operations*, McMaster University, Hamilton, Canada, May 19–20, 113–118.
- Ehmann, K. F. (1990). Grinding wheel profile definition for the manufacture of drill flutes. *CIRP Annal*, 39(1), 153–156.
- Fujii, S., DeVries, M. F., & Wu, S. M. (1970). An analysis of drill geometry for optimum drill design by computer — part I: drill geometry analysis. *ASME Journal of Engineering for Industry*, 92, 647–656.
- Fujii, S., DeVries, M. F., & Wu, S. M. (1970). An analysis of drill geometry for optimum drill design by computer — part II: computer aided design, *ASME Journal of Engineering for Industry*, 92, 657–666.

- Gahlin, R., Alahelisten, A., & Jacobson, S. (1996). The effects of compressive stresses on the abrasion of diamond coatings, *Wear*, 196, 226-233.
- Galloway, D. F. (1957). Some experiments on the influence of various factors on drill performance. *Transaction of ASME*, 79, 191–231.
- Hamade, R. F. & Ismail, F. (2005). A case for aggressive drilling of aluminum. *Journal of Materials Processing Technology*, 166, 86-97.
- Hu, J., Chou, Y. K., & Thompson, R. G. (2008). A numerical study of interface behavior of diamond coated cutting tools, *Transactions of NAMRI/SME*, 36, 533-540.
- Hu, J., Chou, Y. K., & Thompson, R. G. (2007). On stress analysis of diamond coating cutting tools, *Transactions of NAMRI/SME*, 35, 177-184.
- Oles, E. J., Inspektor, A., & Bauer, C.E. (1996). The new diamond-coated carbide cutting tools. *Diamond and Related Materials*, 5(6-8), 617-624.
- Ren, R. & Ni, J. (1999). Analyses of drill flute and cutting angles. *International Journal of Advanced Manufacturing Technonogy*, 15, 546–553.
- Shyu, B. (2002). Computer Simulations for Burr Formation Study. *Ph.D. thesis, University of California, Berkeley*.
- Stephenson, D. A. & Agapiou, J. S. (1997). Metal cutting theory and practice. Marcel Dekker, Inc., 191-205.
- Tsai, W. D. & Wu, S. M. (1979). Computer Analysis of Drill Point Geometry. *International Journal of Machine Tool Design and Research*, 19(1), 95–108.
- Vijayaraghavan, A. & Dornfeld, D. A. (2004). Automated drill modeling for drilling process simulation. *Journal of Computing and Information Science in Engineering*, 7, 276–282.

CHAPTER 3

NUMERICAL ANALYSIS OF INTERFACE BEHAVIOR OF DIAMOND COATED TOOLS

Abstract

Interface delamination is the major weakness limiting diamond-coated tool performance in machining. Thus, quantitative characterizations of interface behavior are important to better understand and design diamond-coated tools. In this study, a cohesive zone model is used to investigate coating-substrate interface behaviors. The cohesive zone model is based on a bilinear traction-separation law. The model is implemented in finite element codes to simulate the indentation processes with either a spherical or a wedge indenter, and to analyze the delamination size of diamond-coated tungsten-carbide substrates.

The simulations of the indentation with a spherical indenter indicate the following outcomes; (1) increasing the coating Young's Modulus reduces the delamination size, (2) a thicker coating tends to have greater resistance to interface delamination, and (3) the deposition residual stresses facilitate interface delamination. The results of the indentation simulations with a wedge indenter can be summarized below. (1) The substrate surface curvature slightly affects the loading vs. displacement curves; however, it makes the specimens more susceptible to interface delamination. (2) The residual stresses increase the delamination size under indentations, and make the substrate more compliant. (3) The coating with a larger Young's Modulus has less delamination sizes. (4) The coating thickness provides the coating-substrate specimen with greater resistance to interface delamination.

Introduction

As the candidates for alternatives to the polycrystalline diamond tools in machining applications, diamond-coated tools have been widely studied for their superior tribological and mechanical properties. However, diamond-coated tools are not without their problems. There is literature reporting that coating-substrate adhesion for diamond-coated tools limits their performance in machining. Delamination is considered to be the result of poor adhesion quality of diamond-coated tools. Hence, characterizing the interface strength will be critical for better understanding diamond-coated tools.

Among different tests, indentation techniques have been demonstrated to be useful methods for testing the mechanical properties of various materials, and several pioneers have studied coating adhesion through indentations for decades. Mehrotra and Quinto (1985) defined the critical load to form the Hertzian ring crack to measure coating adhesion. By conducting several indentations with increasing loads, Jindal et al. (1987) assessed the slope of the load vs. crack length curve and related it to an interface fracture toughness parameter. Following their works, other researchers (Swain & Mencik, 1994; Gagchi & Evans, 1996; Wang et al., 1998; Kriese & Gerberich, 1999) began to use indentation tests to measure interfacial energy. In addition to conventional indentation experiments and simulations with spherical indenters, investigators (Begley, 2000; Gao & Bower, 2004; Su & Anand, 2006; Kim et al, 2007; Liu et al., 2007; Fredriksson & Larsson, 2008; She et al., 2009; Zisis & Giannakopoulos, 2009) used indentation tests with wedge indenters to evaluate interface cracks and thin film mechanical properties. Although several studies have been conducted with a ductile film on a hard substrate, few researches have been done on hard coatings on ductile substrates. Also, little is known about

the substrate surface curvature effects on the interface delamination of coating-substrate specimens with deposition residual stresses.

Regarding the numerical methodologies, finite element (FE) methods have been widely used for studying the failure of coated solids (Chai, 2003; Michler & Blank, 2001; Miranda et al., 2003; Souza et al, 2001). It has been proven that bending the coating over the compliant substrate produces the concentrated tensile stresses at the coating surface, which initiates lateral or ring cracks there (Chai, 2003). Multiple studies have been carried out on the fracture behavior of coatings and the plasticity of substrates; however, interface delamination has seldom been discussed. In addition, the ring crack initiation mechanism does not explain or evaluate the adhesion strength of an interface. The primary difficulty of analyzing interfacial strengths is modeling of interface behaviors.

For cohesive zone concepts, Barenblatt (1959, 1962) initially proposed the cohesive zone model (CZM) as a possible alternative to explain the fracture mechanics in perfectly brittle materials. Dugdale (1960) assumed the existence of a process zone at the crack tip to propose perfectly plastic materials. Later on, based on models of Barenblatt and Dugdale, the CZM model's application was extended to the fractures of polymers, metals, ceramics, and their composites (Needleman, 1990b; Needleman, 1997; Rice & Wang, 1989; Wappling et al., 1998). Needleman (1987, 1990a, 1990b, 1997) initiated the usage of polynomial and exponential types of traction–separation equations to simulate the particle debonding in metal matrices (See Figure 3.1 (a)). Tvergaard (1990) employed a quadratic traction–displacement jump form to evaluate the interface. A trapezoidal shape of a traction–separation model was used by Tvergaard (1992). Later, a linear traction–separation equation with an additional fracture criterion to propagate multiple cracks along arbitrary paths was used by Camacho and Ortiz (1996). By utilizing a

bilinear CZM, Geubelle and Baylor (1998) simulated the spontaneous initiation and the transverse matrix crack propagation and delamination in thin composite plates.

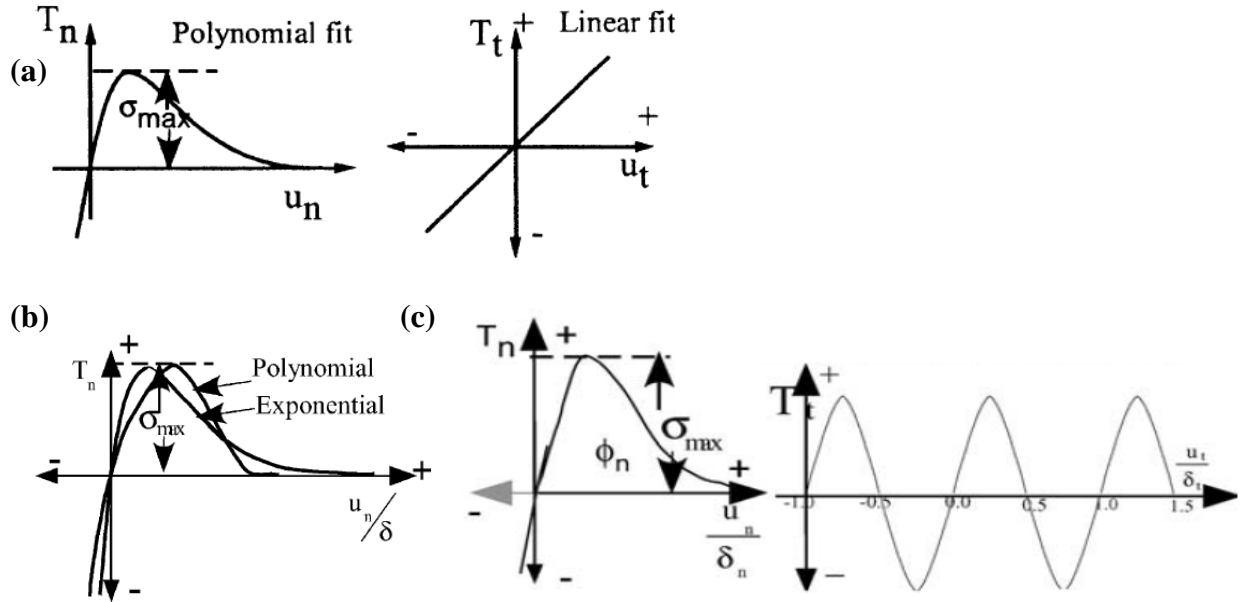


Figure 3.1 (a). Polynomial type cohesive zone (Needleman, 1987), (b) polynomial and exponential type cohesive zone (Needleman, 1990a), and (c) exponential fit for normal T_n and trigonometric fit for shear T_t (Needleman, 1990b).

In the previous studies on interface delamination of diamond-coated tools, Hu et al. (2008) have already conducted a numerical study of the interface behavior of diamond-coated tools through an indentation simulation of a diamond-coated tungsten carbide specimen. The cohesive zone model has been incorporated into the indentation simulation codes and the numerical results reveal the importance of the coating Young's Modulus and the coating thickness effects on interface delamination. Figure 3.2 illustrates the traction-separation response. The cohesive crack tip is initiated when the displacement reaches δ_{max} (characteristic length), where the traction reaches the cohesive strength σ_{max} .

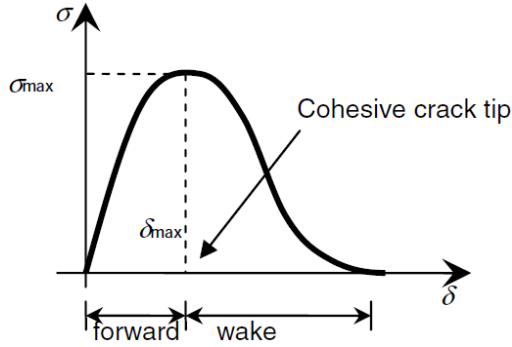


Figure 3.2. Traction-separation response (Hu et al., 2008).

In this chapter, a bilinear traction-separation law (Figure 3.3) was used to evaluate interface response. The T axis represents the traction and the Δ axis represents the interface opening (separation) due to the contact loading. The area of the triangle embodies the work of separation (fracture energy). When the displacement reaches δ_{\max} (a characteristic length), the corresponding damage initiation criterion is reached, and then, the damage evolution follows with the damage initiation, which characterizes the rate at which the cohesive stiffness is degraded once the damage initiation criterion is met. Interface delamination will happen once the displacement reaches δ_c (displacement at failure).

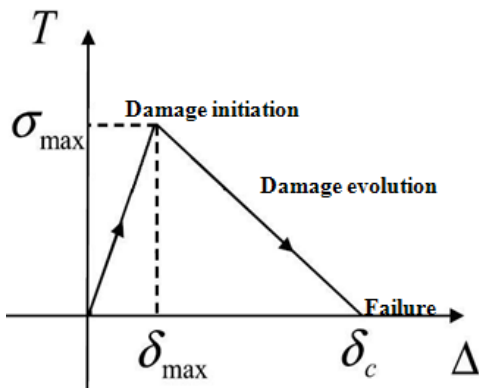


Figure 3.3. Bilinear traction-separation response.

In this research, finite element (FE) simulations incorporating a cohesive zone model are conducted to model the indentation testing of diamond-coated tungsten-carbide tools. The

objective is to better understand the delamination mechanism of a hard coating deposited on a compliant substrate under contact loading.

Finite Element Model of Indentation with a Spherical Indenter

Physical Phenomenon Formulation of Indentation Simulation with Spherical Indenter

ABAQUS is employed to conduct the indentation simulations for coating-substrate specimens with a cohesive zone interface. Referring to Figure 3.4, which is the indentation of an axis-symmetric coating-substrate system, the indenter, with a radius = 50 μm (assumed to be analytically rigid for simplification) is progressively pressed into the specimen until reaching the specified maximum depth, and then gradually withdrawn from the coating surface. Regarding the size of the model with residual stresses (Figure 3.4), $R = 6400 \mu\text{m}$, $h = 3200 \mu\text{m}$, and t represents the coating thickness. For the model without residual stresses, the substrate length (R) is equal to 300 μm because scaling down the size of the model without residual stresses can reduce calculation time, and the model size does not affect the FEA results of the model without residual stresses. However, for the model with residual stresses, size reductions cannot be conducted because the size will affect the magnitude and distribution of the residual stresses, thus affecting the final FEA results. For the material behavior, the CVD diamond coating is assumed to be an elastic body with the following material properties: E (Young's Modulus) = 600 – 1200 GPa and ν (Poisson's ratio) = 0.07. An elastic-plastic constitutive relation is defined for WC-Co substrates (Table 3.1) (Dugdale, 1960). The residual stresses induced due to the thermal expansion mismatch between diamond coatings and carbide substrates are incorporated by applying a deposition temperature (800°C) to this specimen, and cooling this down to the room temperature (25°C) to generate residual stresses, which are specified as the initial state of this specimen for the subsequent indentation simulation. For the element property of the coating

and the substrate, they are specified to be Quad, Structured CAX4R (a 4-node bilinear axisymmetric quadrilateral, reduced integration, hourglass control). For the interface element properties, they are defined as a cohesive element, which is COHAX4 (a 4-node axisymmetric cohesive element). The loading applied to the specimen is controlled by the indentation depth. The static, general analysis is conducted to simulate the loading (30 steps and 1 step per second) and the unloading cycles (30 steps and 1 step per second) of the indentation process.

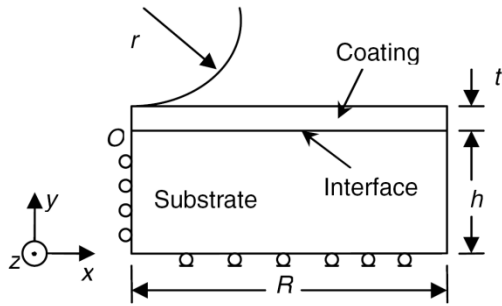


Figure 3.4. Schematic of the indentation on a coated substrate by a sphere (Hu et al., 2008).

Table 3.1

Materials Properties of WC-Co Substrate (Hu et al., 2008)

E (GPa)	ν	σ_0 (MPa)	n	σ_y (GPa)
619.5	0.24	18036	0.244	5.76

σ_0 : Strength coefficient, n : Strain hardening exponent, σ_y : Yield strength.

Interface Behavior Modeling

Geubelle and Baylor (1998) utilized a bilinear CZM to simulate the damage initiation and propagation of the delamination in thin composite plates subjected to a low-velocity impact. The traction-separation relation for the interface is such that with the increasing of interfacial separations, the traction across the interface linearly reaches a maximum value (the damage initiation value) and then decreases linearly (the damage evolution), and finally allows a

complete decohesion (delamination). The traction-separation under the pure tension and the pure shear are plotted in Figure 3.5.

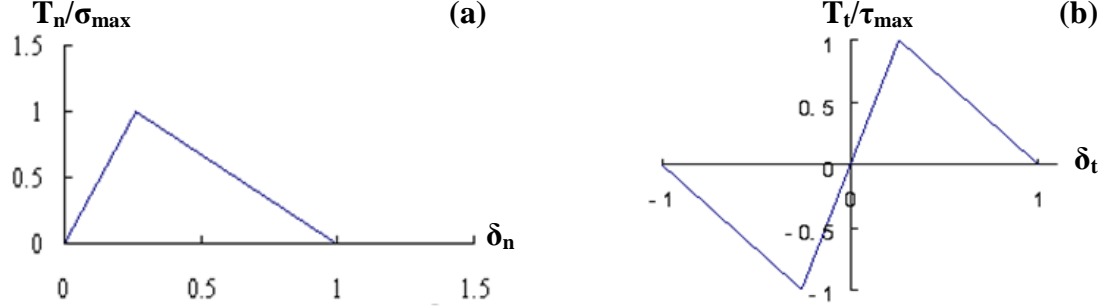


Figure 3.5. (a) Normal traction T_n as a function of the normal separation Δ_n for $\Delta_t=0$, (b) shear traction T_t as a function of the shear separation Δ_t for $\Delta_n=0$. (Geubelle & Baylor, 1998).

The interfacial constitutive relations for a bilinear CZM are given below (Geubelle & Baylor, 1998):

For $\delta_n > 0$,

$$T_n = \begin{cases} \frac{\sigma_{\max}}{\delta_{\max}} \delta_n & (\delta \leq \delta_{\max}) \\ \frac{\sigma_{\max}}{\delta} \frac{1-\delta}{1-\delta_{\max}} \delta_n & (\delta > \delta_{\max}) \end{cases} \quad (1)$$

$$T_t = \begin{cases} \frac{\sigma_{\max}}{\delta_{\max}} \frac{\Delta_n^c}{\Delta_t^c} \delta_t & (\delta \leq \delta_{\max}) \\ \frac{\sigma_{\max}}{\delta} \frac{1-\delta}{1-\delta_{\max}} \frac{\Delta_n^c}{\Delta_t^c} \delta_t & (\delta > \delta_{\max}) \end{cases} \quad (2)$$

For $\delta_n = 0$,

$$T_t = \begin{cases} \frac{\sigma_{\max}}{\delta_{\max}} \frac{\Delta_n^c}{\Delta_t^c} \delta_t & (\delta \leq \delta_{\max}) \\ \frac{\sigma_{\max}}{\delta} \frac{1-\delta}{1-\delta_{\max}} \frac{\Delta_n^c}{\Delta_t^c} \delta_t & (\delta > \delta_{\max}) \end{cases} \quad (3)$$

σ_{\max} and τ_{\max} are the interface normal and tangential strength, respectively; δ_{\max} is the interface characteristic length parameter; Δ_n^c and Δ_t^c are the critical normal and tangential

separations at which the complete separation is assumed; and Δ_n , Δ_t and Δ denote the non-dimensional normal, tangential and total displacement jumps, respectively, defined by

$$\delta_n = \frac{\Delta_n}{\Delta_n^c}, \delta_t = \frac{\Delta_t}{\Delta_t^c}, \delta = \sqrt{\delta_n^2 + \delta_t^2} \quad (4)$$

The normal (ϕ_n) and tangential (ϕ_t) works of separation per unit area of the interface are given by (Chandra et al., 2002)

$$\phi_n = \sigma_{\max} \Delta_n^c / 2, \quad \phi_t = \tau_{\max} \Delta_t^c / 2, \quad (5)$$

Cohesive Zone Parameter Determination

In the model above, the cohesive zone model (normal mode) can be characterized by σ_{\max} , $\delta_{n\max}$, Δ_n^c and the shear mode can be characterized by τ_{\max} , $\delta_{t\max}$, Δ_t^c .

The cohesive zone parameters are idealized as material constants determined by a soft layer (the substrate material). As Co in the WC inserts needs to be removed at the surface by etching prior to the diamond deposition, the cohesive characteristics are dominated by the tungsten carbide. Cavalli (2003) has confirmed this by modeling the deformation and the failure of spot-welded joints using a cohesive zone model. They found that the normal strength of a nugget is close to the measured ultimate strength of the bulk material of strips.

In Hu's study (Hu, Chou & Thompson, 2008) on the diamond coating tungsten carbide model, normal and shear characteristic lengths equal 0.26 μm and 1.05 μm , respectively. Since $\phi_n = \sigma_{\max} \Delta_n^c / 2 = e \delta_{n\max} \sigma_{\max}$, the normal strength σ_{\max} and Δ_n^c are dependent on each other, and only one needs to be determined. σ_{\max} is estimated to be 543 MPa by matching stress-strain curves between FE simulations and experiments for the single phase WC (Hu, Chou & Thompson, 2008). Thus, Δ_n^c is 1.4135 μm ; assuming the shear work of separation has the same value as the normal work of separation (Hu, Chou & Thompson, 2008), $\tau_{\max} = \sigma_{\max} / 3^{0.5}$ is adopted in this study; thus both τ_{\max} and Δ_t^c can be determined. G1 and G2 are the interface

stiffness for normal and shear modes, respectively, and $G1 = \sigma_{\max}/\delta_{n\max} = 2.088\text{GPa}$ and $G2 = \tau_{\max}/\delta_{t\max} = 0.299\text{GPa}$.

In this study, quasi-static finite element computations are unable to converge to an equilibrium solution; therefore, a small viscosity is introduced in constitutive equations for the cohesive interface to avoid such numerical difficulties (Gao & Bower, 2004).

The parameters of a cohesive zone for the diamond-coated WC are shown in the Table 3.2.

Table 3.2

The Cohesive Zone Parameters for Diamond-Coated WC-insert

<i>G1/GPa</i>	<i>G2/GPa</i>	<i>σ_{\max}/MPa</i>	<i>τ_{\max}/MPa</i>	<i>Fracture energy (J/m^2)</i>	<i>Viscosity factor (ζ)</i>
2.088	0.299	543	314	383.77	1E-5

Results and Discussions for Indentations with a Spherical Indenter

Typical Examples for Indentations with a Spherical Indenter

In this example (Figure 3.6), the substrate length, the indenter radius, and the coating thickness are equal to 300 μm , 50 μm , and 30 μm , respectively. The indenter is pressed with a 6 μm downward displacement, and no residual stresses are applied; in addition, Figure 3.6 (a) illustrates the normal traction (S22) of the coating-substrate system when the indenter is fully loaded, and Figure 3.6 (b) shows the normal traction (S22) of the coating-substrate system when the indenter is completely withdrawn from the coating surface.

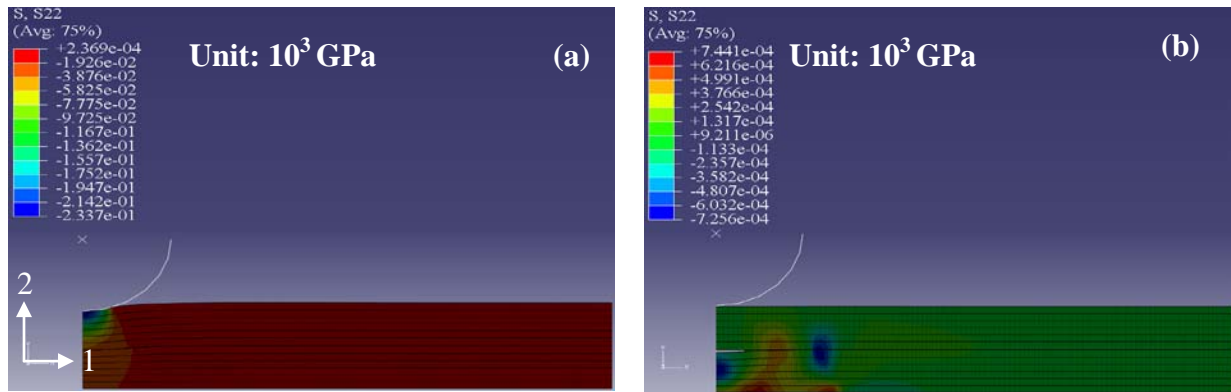


Figure 3.6 Example of plastic behaviors in a coating-substrate system during the indentation process (a) fully loading and (b) completely unloading.

Figure 3.7 illustrates the normal traction and separation at the interface after the indenter is completely withdrawn. For a delamination radius, it starts from the axis of symmetry with initial cracks continuing to increase and crack tips propagating toward away from the axis of symmetry; thus, delamination sizes are equal to a delamination radius multiplied by two because this coating-substrate model is axisymmetric. In this study, definition of the delamination can be defined as “cohesive elements failing,” which means that cohesive elements experience both damage initiation and evolution phases, allowing a complete interface decohesion. For uncracked elements, these will still phenomenologically exist and bind between the coating and the substrate. In Figure 3.7 (a), the highlighted specified dimension is the magnitude of a delamination radius, and in this study, a delamination radius is measured from the axis of symmetry to the end of the cracked area. The highlighted oval-shape sign represents uncracked cohesive elements. In Figure 3.7 (c), it is noted that most of the normal separation value is negative. This is because the U2 displacement here represents the coordinate of cohesive elements along the “2” direction. During the initial state without any contact loading, cohesive zone elements are on the original location, which is the location giving zero U2 displacement. Even though the cohesive zone will go up, namely the positive direction, when the indenter is

withdrawn from the sample, uncracked cohesive elements near the axis of symmetry are still located on the negative side of the “2” direction. The small positive value of the normal separation indicates that when a indenter is pressed into the sample, the side of the interface away from the axis of symmetry will go up slightly because the vertical displacement of both sides of the interface is not constrained. Hence, once one side is loaded, following a downward displacement, another side goes up slightly because the substrate length is long enough.

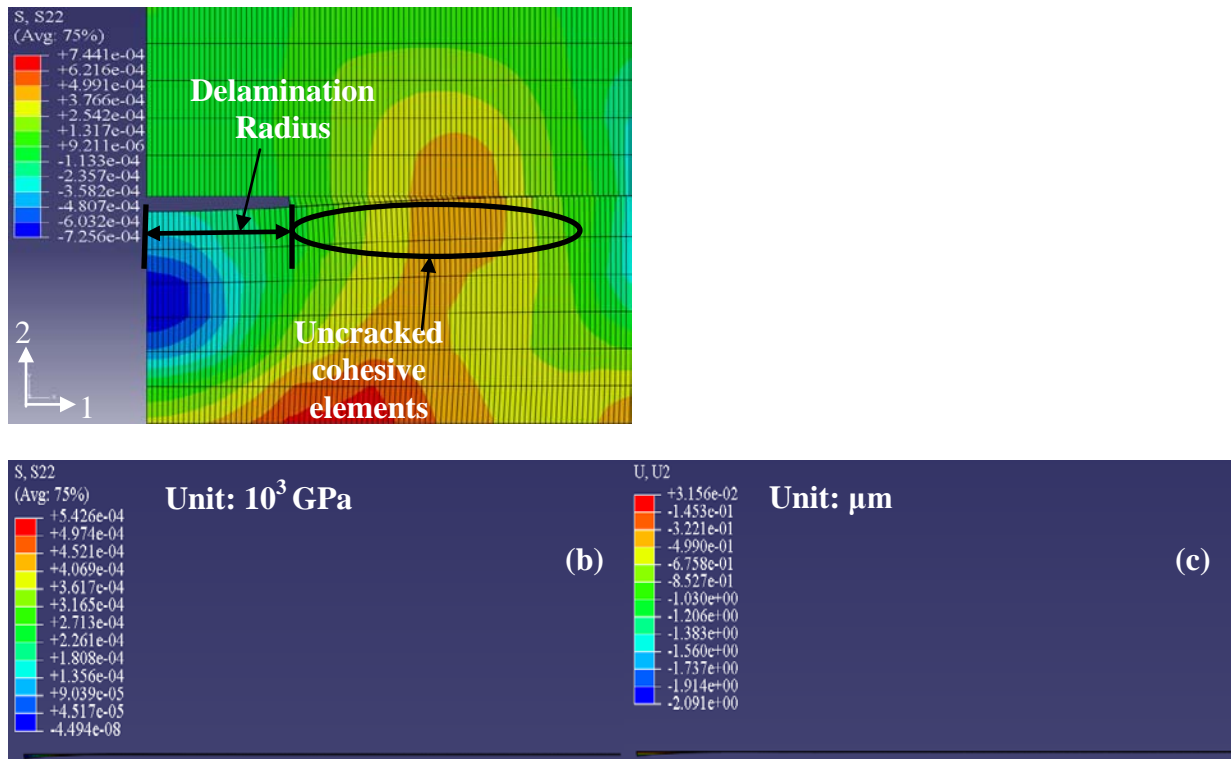


Figure 3.7. (a) Stress contours of the normal separation as the indenter completely withdrawn, (b) the normal traction at the interface, and (c) the normal separation at the interface.

By extracting interface stresses on the above example, the plot for the normal traction vs. horizontal distance at the interface can be obtained (see Figure 3.8). This distance moves from the axis of symmetry to the right end of a substrate, which is 300 μm in length. In this graph, the peak traction is equal to 543 MPa, representing the location of cohesive tips. The traction value begins to decrease while this value reaches the normal strength (543 MPa).

Another phenomenon that deserves attentions is the fact that if the indentation depth is controlled with a small value, cohesive elements along the interface will not crack because the contact loading is not large enough to make cohesive elements experience both damage initiation and damage evolution processes. Figure 3.9 shows the above described conditions in which no cohesive elements fail. In this case, the indenter is pressed with a 4 μm downward displacement.

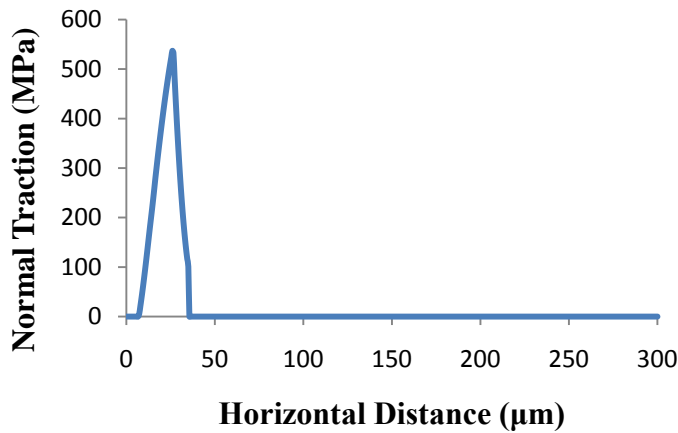


Figure 3.8. The normal traction at the interface after the indenter completely unloaded.

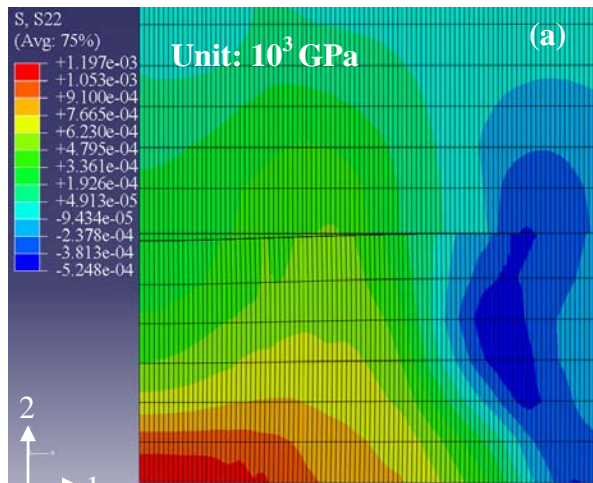


Figure 3.9. No cracked cohesive elements along the interface.

The above models are further used to investigate the relationships of indentation loadings and delamination sizes. Figure 3.10 indicates the non-linear relationships between the maximum indentation loading and delamination sizes. This plot reveals that the critical loading for the

interface delamination of the sample without residual stresses is around 110 N. However, for the model with residual stresses, the critical loading is around 98.2 N, which indicates that the residual stresses reduce the critical loading causing interface delamination. The model is also employed to study the coating attribute effects on delamination sizes. Table 3.3 shows the range of coating parameters studied.

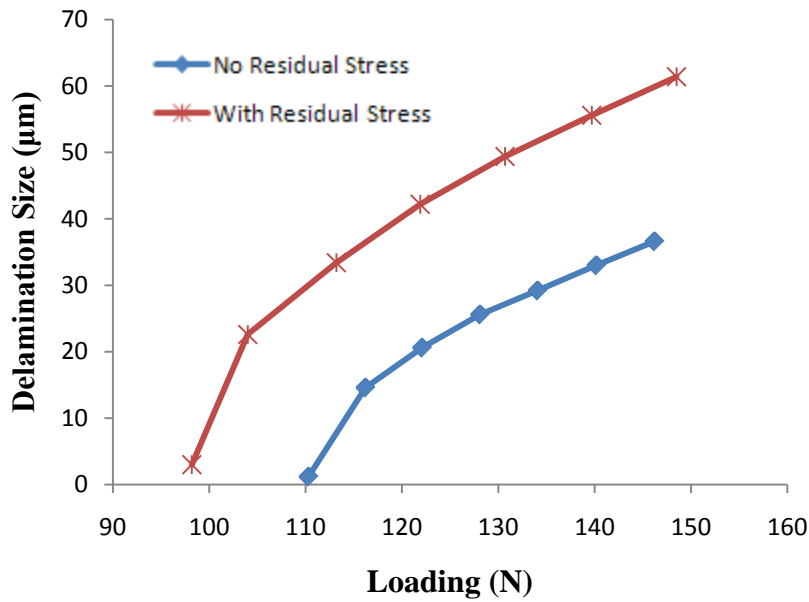


Figure 3.10. Loading vs. delamination sizes ($E = 1200$ GPa, Deposition Temperature = 800°C , Coating Thickness = $30\ \mu\text{m}$).

Table 3.3

Range of Parameters Studied for Indentation Simulations with a Spherical Indenter

Young's Modulus, E (GPa)	600-1200
Coating thickness, t (μm)	3-50
Deposition Temperature ($^{\circ}\text{C}$)	800°C

Coating Attribute Effects on Indentations with a Spherical Indenter

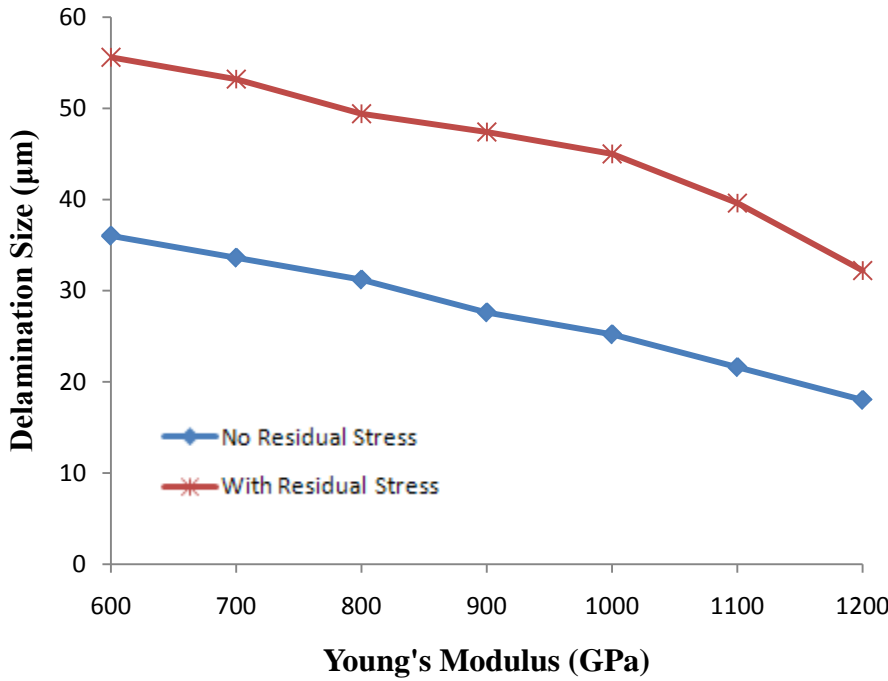


Figure 3.11. Effects of the coating Young's Modulus and residual stresses on interface delamination sizes (Coating Thickness = 30 µm, Deposition Temperature = 800°C).

The effect of the coating Young's Modulus and residual stresses on the interface delamination is shown in Figure 3.11. The maximum loading of each case hereafter is kept as 120 N. As shown, delamination sizes decrease nearly linearly with the increase of the coating Young's Modulus. Young's Modulus represents the ability of a material to resist elastic deformations. The larger the Young's Modulus, the harder a material is to deform. Under the same loading, coating with a larger Young's Modulus suffers less deformation and smaller strain, and permanent plastic deformations generated underneath a substrate is also smaller. When it comes to the unloading process, the delamination generated at the coating/substrate interface will also be less due to less resistance coming from the recovery. In addition, it is also noted that residual stresses can facilitate the interface delamination, which produces larger delamination

sizes than the sample without residual stresses. Hu's simulations (Hu, Chou & Thompson, 2008) using ANSYS also demonstrates the same regularity.

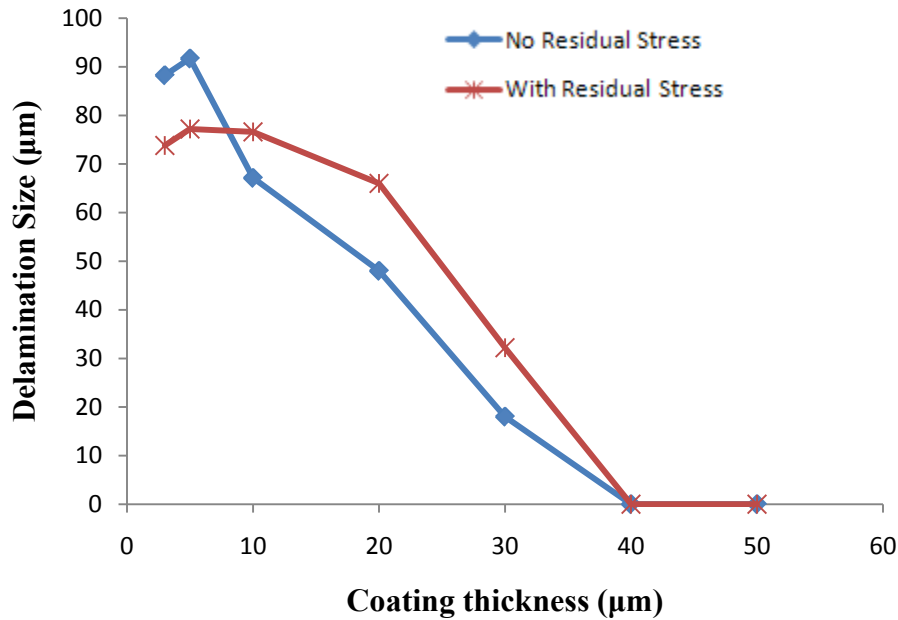


Figure 3.12. Effects of the coating thickness and residual stresses on delamination sizes ($E = 1200$ GPa, Deposition Temperature = 800°C).

The effects of the coating thickness and residual stresses on the interface delamination are plotted in Figure 3.12. The maximum loading for each case is also kept as 120 N. For coatings with a 40 µm and a 50 µm thickness, no delamination occurs at the coating/substrate interface. Available literature reports that the critical loading to initiate delamination increases with the coating thickness (Huang, Zhao & Zhang, 2004). For the coating thicknesses between 5 µm - 40 µm, with the coating thickness decreasing, delamination sizes noticeably increase. However, further decreasing the coating thickness to a smaller value indicates a reverse regularity. This is because when the coating thickness is above a certain point, the thinner the coating, the easier for it to deform; thus, larger plastic deformations will be generated in the substrate, causing larger delamination sizes. However, when coating thickness is too thin, excess

loss of rigidity may exert an opposite effect. In addition, residual stresses here increase delamination sizes again.

A Finite Element Model of Indentations with a Wedge Indenter

Problem Description

It has already been verified in the Chapter 2 that interface stresses along the cutting edge can be significant, and radial normal stresses are largely tensile, over 1.0 GPa, which may affect the adhesion integrity. A cohesive zone model developed in this chapter is further incorporated into the 2D diamond-coated insert to conduct the deposition residual stresses analysis. Figure 3.13 illustrates residual stresses contours and interface stresses of the diamond-coated insert, which has a 30 μm coating thickness and a 20 μm edge radius. This model is analyzed under plain strain conditions, and the material properties are the same as those used in Chapter 2. Figure 3.13 (b) provides a zoomed-in view of stress distributions along the interface of the cutting edge. It is noted that interface stresses are significant, which will affect interface behaviors of diamond-coated tools. In addition, Figure 3.13 (c) and Figure 3.13 (d) reveal that with the inclusion of a CZM, the maximum interface stresses are reduced, and for σ_r (the radial normal stress), it decreases from 1.5 GPa (rigid contact) to 1.3 GPa (with a CZM). For σ_θ (the circumferential stress), it decreases from 3.81 GPa (rigid contact) to 3.51 GPa (with a CZM). The rigid contact model represents the model without a CZM. Hence, it is important to include both residual stresses and a CZM into indentation finite element models when investigating interface behaviors of diamond-coated tools.

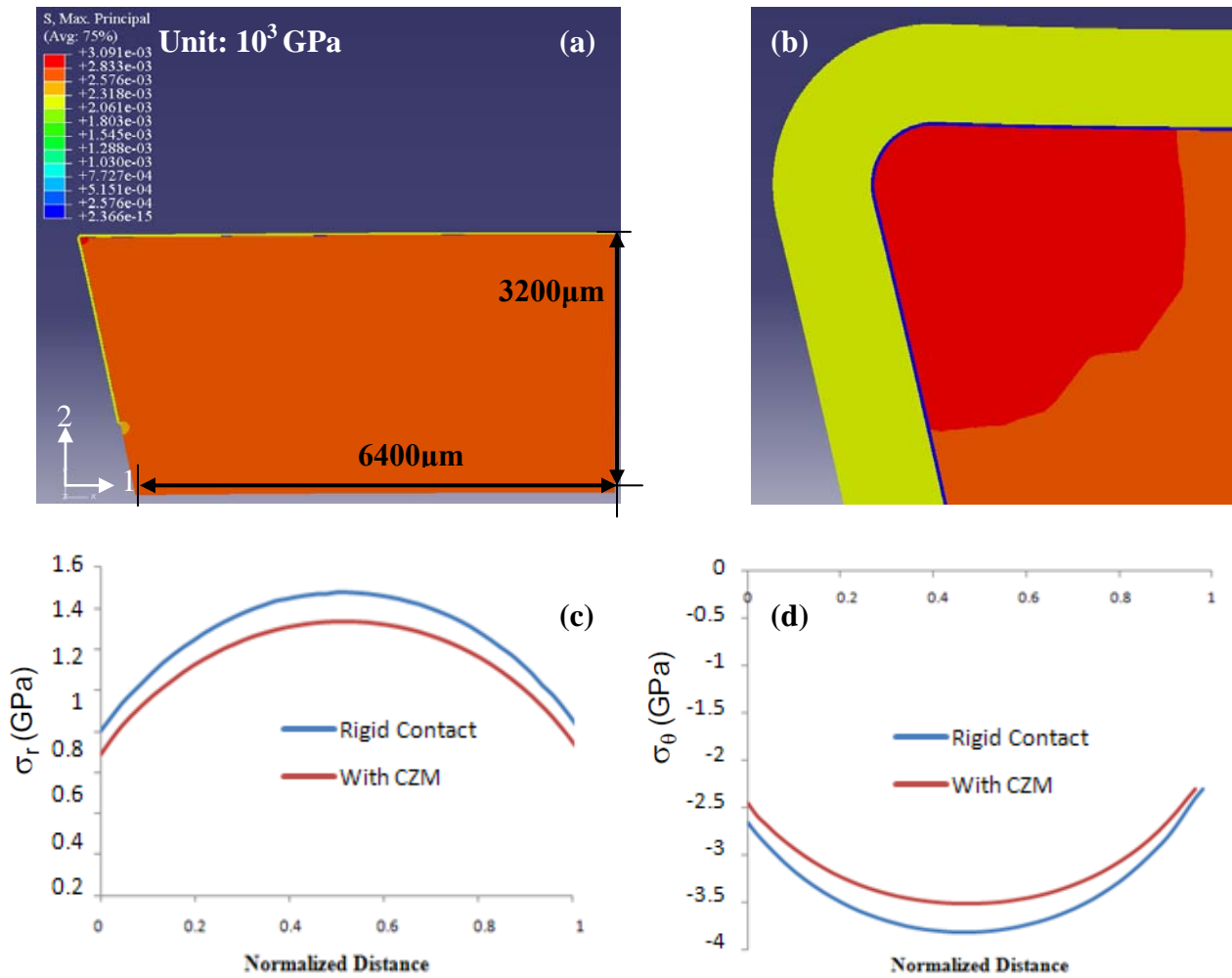


Figure 3.13. Residual stresses effect on the diamond coated insert with the inclusion of a cohesive zone: (a) overall view, (b) zoomed-in view of the cutting edge, (c) radial normal stress, and (d) circumferential stress.

Even though the flat surface indentation simulation model provides good representations and explanations for interface behaviors of diamond-coated tools, this method is still under the question regarding the type of its contact load because during the machining process, it is the cutting edge area contacting the workpiece causing the interface delamination, and the shape of a cutting edge is obviously not flat. Hence, the contact load causing the coating delamination is located on a surface with curvature, strengthening the necessity to conduct indentation

simulations on a curved model. Thus, simulations of indentations with a wedge indenter are proposed.

Physical Phenomenon Formulation of Indentation Simulations with a Wedge Indenter

ABAQUS is employed once again to conduct simulations of the indentation with a wedge indenter. Figure 3.14 describes the indentation finite element model with a wedge indenter. Regarding sizes of the model, for the model with a 100 μm specimen radius, the length and width are equal to 70 μm and 69 μm , respectively. Models with 300 μm , 500 μm , 700 μm , 1400 μm , and 2800 μm specimen radius are given with a fixed width value equal to 600 μm , and the lengths for them are equal to 482 μm , 841 μm , 1200 μm , 1200 μm , and 1200 μm , respectively. The wedge indenter (90° wedge angle, 5 μm wedge radius), assumed to be an analytical rigid body for simplification, is progressively pressed into the specimen until reaching a specified maximum indentation depth and then gradually withdrawn from the coating surface. The methodologies to apply residual stresses and material properties are the same as before. With regard to element properties, CPE4R (A 4-node bilinear plane strain quadrilateral, reduced integration, hourglass control) is assigned to a coating and a substrate, and COH2D4 (A 4-node two-dimensional cohesive element) is assigned to a cohesive zone model. The mesh density of the indenter-coating and the coating-substrate contact areas is higher (0.6 μm element size), and for the area away from the contact area, the mesh is coarser (16 μm element size). As for boundary conditions, the X and Y movements of a specimen bottom surface are constrained.

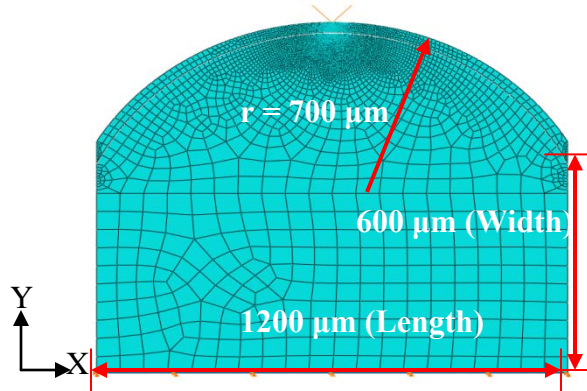


Figure 3.14. Indentation finite element model with a wedge indenter.

Interface Behavior Modeling and Cohesive Parameters Determination

The methodologies applied on the indentation model with a spherical indenter are revisited here. Details regarding the determination of cohesive zone parameters can be referred to the indentation model with a spherical indenter. The only major difference is that a viscosity factor (ξ) is excluded in this study because this model is easy to converge under plain strain conditions.

Results and Discussions for Indentations with a Wedge Indenter

Typical Examples for Indentations with a Wedge Indenter

In this example (Figure 3.15), the indenter is progressively pressed into the specimen. The downward displacement is $10 \mu\text{m}$. Figure 3.15 (a) shows the maximum principal residual stresses contour during the initial state. Figure 3.15 (b) and Figure 3.15 (c) show two indenter fully loading pictures. Figure 3.16 illustrates equivalent plastic strains of the specimen after the indenter is fully unloaded. Due to the finite strength of the interface, the substrate yielding initiates under the interface. In addition, it is also noted that the maximum compressive stress value is really high, in the neighborhood of 319.3 GPa in compression; this is because the indenter radius is extremely small, which is only $5 \mu\text{m}$, thus leading to a stress concentration.

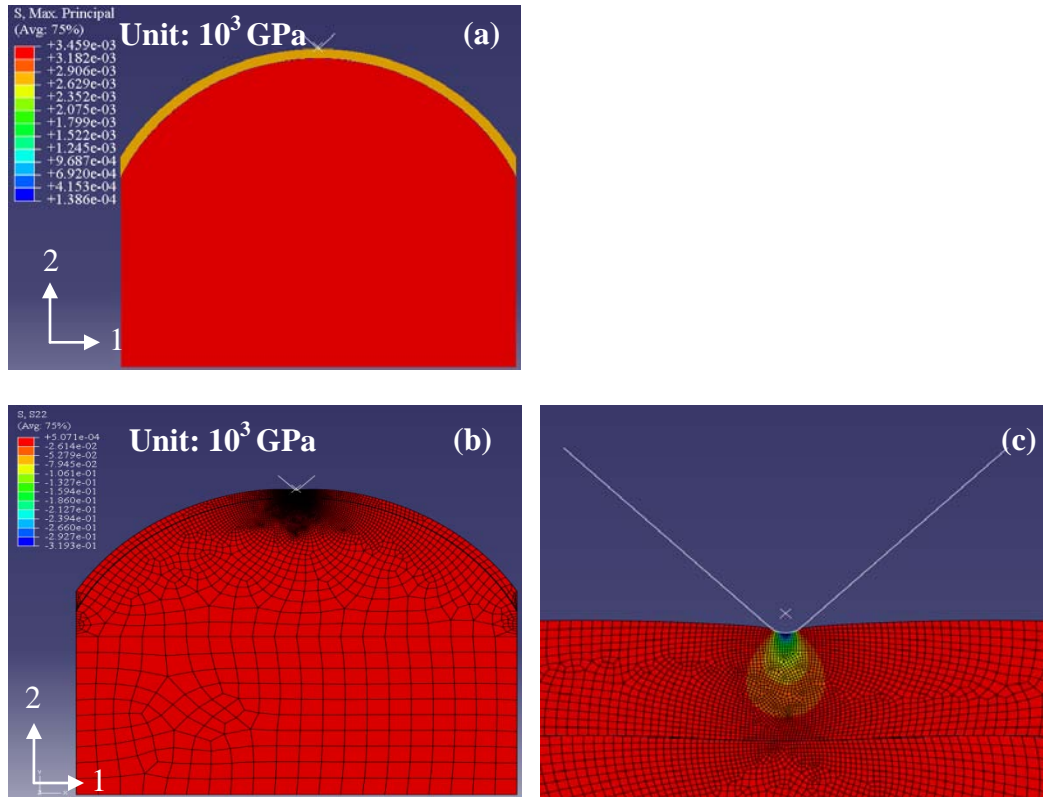


Figure 3.15. (a) Residual stresses contours during the initial state, (b) S22 stress contour, fully loading, and (c) zoom-in view of the contact area between the indenter and the coating ($E = 1200$ GPa, Coating Thickness = $30\ \mu\text{m}$, Deposition Temperature = 800°C , Specimen Radius = $700\ \mu\text{m}$, Indentation Depth = $10\ \mu\text{m}$).

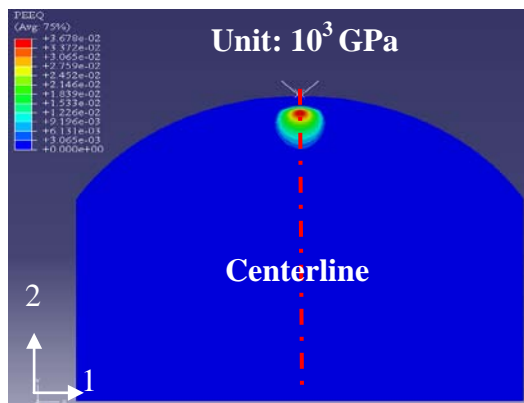


Figure 3.16. Equivalent plastic strains, fully unloading, $10\ \mu\text{m}$ indentation depths ($E = 1200$ GPa, Coating Thickness = $30\ \mu\text{m}$, Deposition Temperature = 800°C , Specimen Radius = $700\ \mu\text{m}$, Indentation Depth = $10\ \mu\text{m}$).

Figure 3.17 depicts the interface normal traction and separation after the indenter is completely withdrawn from the sample. With regard to delamination sizes, they start from the

centerline with initial cracks continuing to increase. The crack tips propagate away from the centerline to form interface cracks. Figure 3.17 (a) represents the dimension of delamination sizes, which are equal to the arc length of a cracked area.

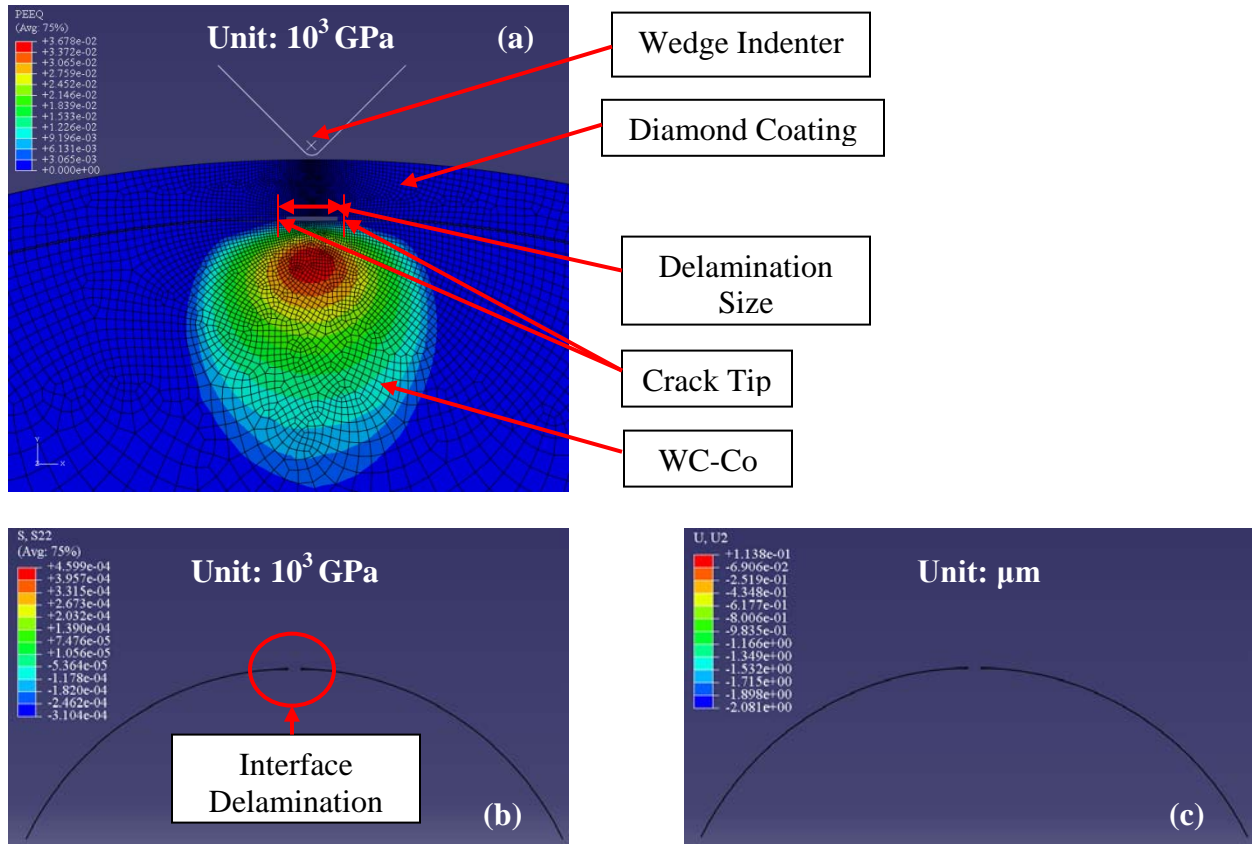


Figure 3.17. (a) Normal separations after indenter fully unloaded, (b) normal tractions at the interface, and (c) normal separations at the interface. ($E = 1200 \text{ GPa}$, Coating Thickness = $30 \text{ }\mu\text{m}$, Specimen Radius = $700 \text{ }\mu\text{m}$, Deposition Temperature = 800°C , Indentation Depth = $10\text{ }\mu\text{m}$).

Figure 3.18 shows the plot for the normal traction vs. the horizontal distance at the interface. This distance starts from the centerline to the end of the substrate. The peak traction is equal to 543 MPa , representing the location of cohesive tips. The traction value begins to decrease while the value reaches the instantaneous normal strength.

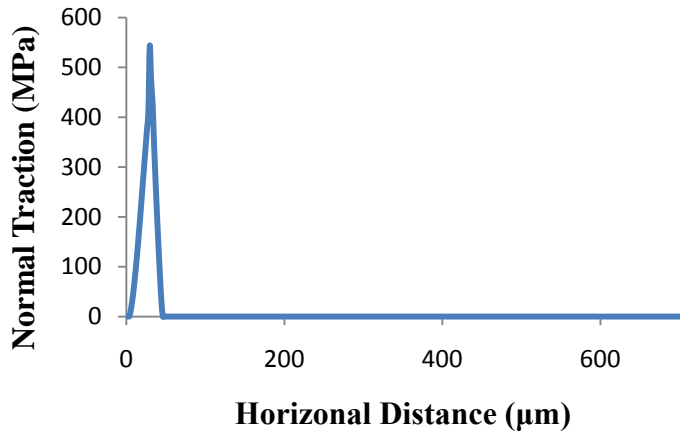


Figure 3.18. Normal traction vs. horizontal distance at the interface after indenter completely unloaded.

Figure 3.19 is intended to reveal non-linear relationships between the indentation loading and delamination sizes for models with curvature and planar characteristics. It is further noted that under the same loading conditions, models with curvature have larger delamination sizes than models without it, which indicates that models with curvature are susceptible to the interface delamination. This model is also used to study coating attribute effects on delamination sizes. Table 3.4 provides the range of coating parameters studied.

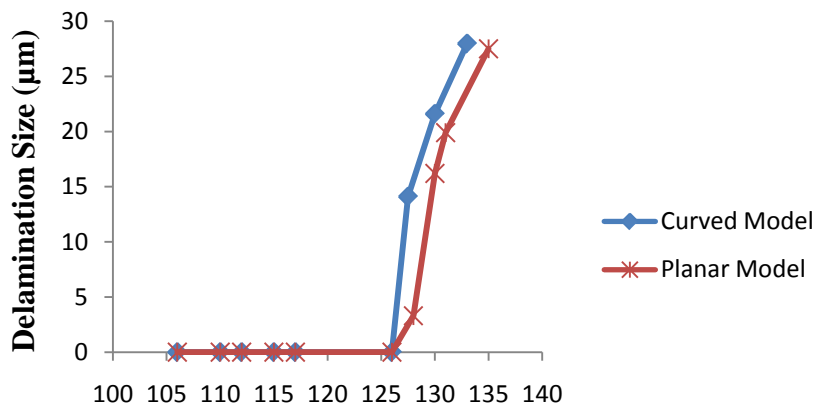


Figure 3.19. Loading vs. delamination size ($E = 1200 \text{ GPa}$, σ_r (Residual Stresses) = 0 GPa , Coating Thickness = 30 μm , Specimen Radius = 700 μm).

Table 3.4

Range of Parameters Studied for Indentation Simulations with a Wedge Indenter

<i>Young's Modulus, E(GPa)</i>	<i>600 – 1200</i>
Coating thickness, t(μm)	10 – 50
Deposition Temperature ($^{\circ}\text{C}$)	600 – 1000
Specimen Curvature (μm)	100 – 2800

Coating Attribute Effects on Indentations with a Wedge Indenter

Figure 3.20 depicts the substrate surface curvature effect on loading vs. displacement curves, and in this plot, it is concluded that the curvature slightly affects loading vs. displacement curves. Figure 3.21 and Figure 3.23 reveal that the curvature affects interface delamination sizes and that specimens with a large curvature are more susceptible to the interface delamination. Figure 3.21 also indicates that samples with residual stresses have larger delamination sizes. Figure 3.22 illustrates normal tractions and normal separations of the specimen with a smallest and a largest radius, respectively. Qasim et al. (2004) carried out both indentation experimentations and finite element (FE) simulations to test the specimen geometric effects on the critical loading to produce cone cracks at the surface of a coating and interface cracks between a coating and a substrate. Their results revealed that non-planar specimens appear more susceptible to the interface delamination. This result agrees with our conclusions concerning curvature effects.

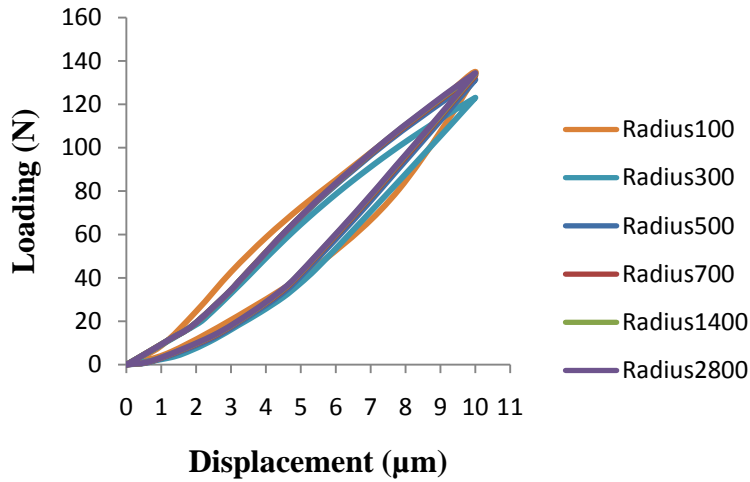


Figure 3.20. Loading vs. displacement curves with different curvatures ($E = 1200 \text{ GPa}$, σ_r (Residual Stresses) = 0 GPa , Coating Thickness = 30 μm , Indentation Depth = 10 μm).

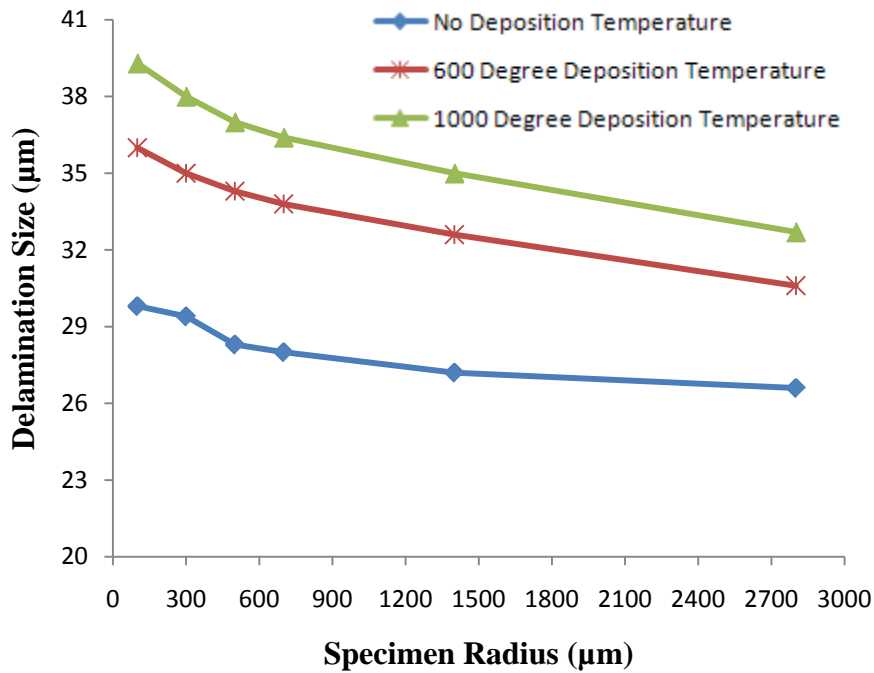


Figure 3.21. Curvature and residual stresses effects on delamination sizes ($E = 1200 \text{ GPa}$, Coating Thickness = 30 μm , Indentation Depth = 10 μm).

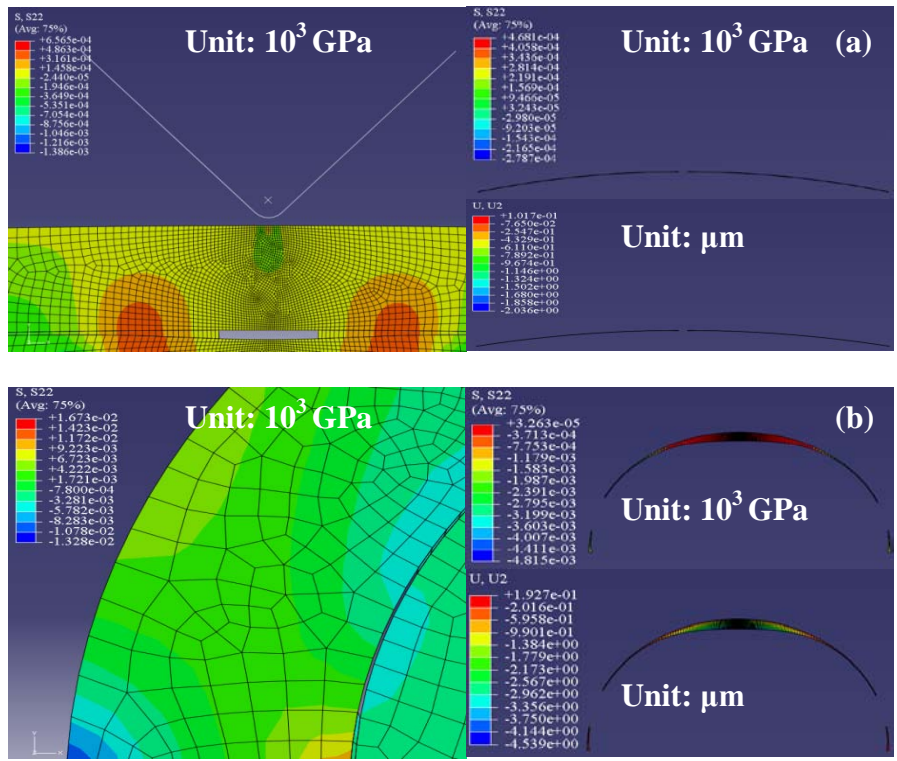


Figure 3.22. (a) Normal tractions and separations for a model with a specimen radius = 2800 μm, and (b) normal tractions and separations for a model with a specimen radius = 100 μm ($E = 1200$ GPa, σ_r (Residual Stresses) = 0 GPa, Coating Thickness = 30 μm, Indentation Depth = 10 μm).

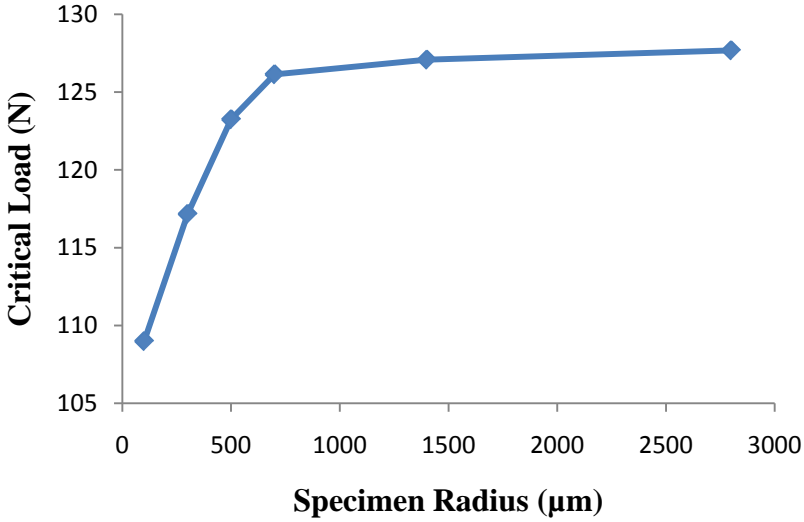


Figure 3.23. Curvature effects on the critical loading ($E = 1200$ GPa, σ_r (Residual Stresses) = 0 GPa, Coating thickness = 30 μm).

Figure 3.24 shows the relationship between the coating Young's Modulus and delamination sizes. The indentation loading is fixed at 133N for all cases in this example. The indentation depth for models with a curvature are 12.8 μm , 12.1 μm , 11.58 μm , 11.1 μm , 10.8 μm , 10.3 μm , and 10 μm , respectively, with the coating Young's Modulus from 600 GPa to 1200 GPa. Besides, the indentation depth for planar models are 12.5 μm , 11.8 μm , 11.3 μm , 10.9 μm , 10.5 μm , 10.1 μm , and 9.9 μm , respectively, with the coating Young's Modulus from 600 GPa to 1200 GPa. This demonstrates that with the increase of a coating Young's Modulus, delamination sizes decrease. A possible explanation for this phenomenon is that since the Young's Modulus represents the capability of a material to resist elastic deformations, under the same loading condition, the coating with a larger Young's Modulus is more inclined to show less strain and less deformation, thus reducing permanent plastic deformations of a substrate as well as delamination sizes. The plot also reveals that the sample with a curvature is more inclined to the interface delamination as compared to the planar model.

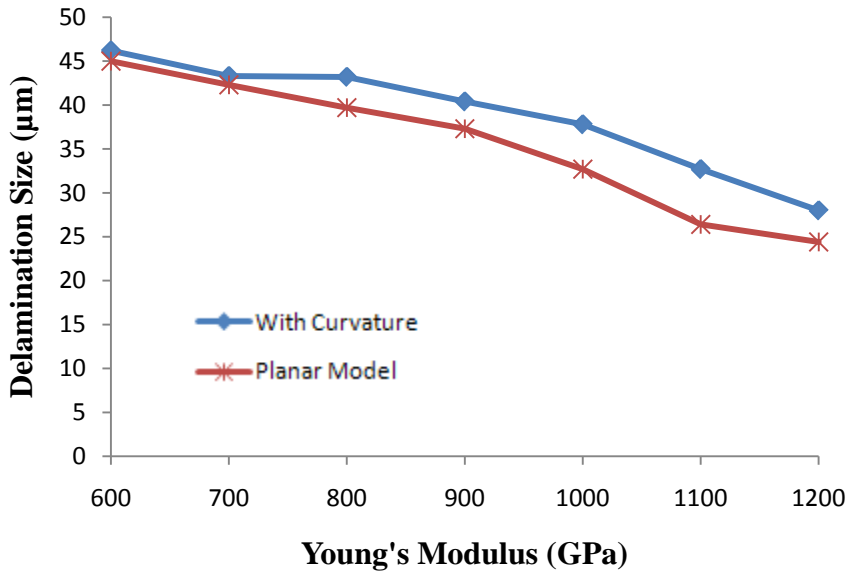


Figure 3.24. Coating Young's Modulus and curvature effects on delamination sizes (Specimen Radius = 700 μm , σ_r (Residual Stresses) = 0 GPa, Coating thickness = 30 μm , Indentation Loading = 133 N).

Figure 3.25 and Figure 3.26 show the comparison for loading vs. displacement curves for samples with residual stresses and without residual stresses, as well as residual stresses effects on the interface delamination. Figure 3.25 shows apparent deviations between these lines with different residual stresses. The sample with residual stresses appears to be more compliant under the same indentation depth. In addition, the sample with residual stresses is more subject to the interface delamination, and its delamination sizes are larger than the one without residual stresses (see Figure 3.26). Vanimisetti et al. (2006) used ABAQUS to numerically analyze residual stresses effects on the indentation. They demonstrated that residual stresses make coating-substrate systems more compliant. Similarly, Figure 3.26 demonstrates that the increased residual stresses correspondingly marginally increase delamination sizes. Jindal et al. (1987) employed the scratch testing on TiN coatings with WC-Co substrates to show that tensile residual stresses developed in the coatings reduce adhesion parameters. Through producing boron carbide coatings on a titanium alloy substrate by plasma spraying, and estimating the critical strain energy release rate of the interface by four-point bending tests, Tsui et al. (1994) demonstrated that remarkable errors would occur if residual stresses were not taken into consideration.

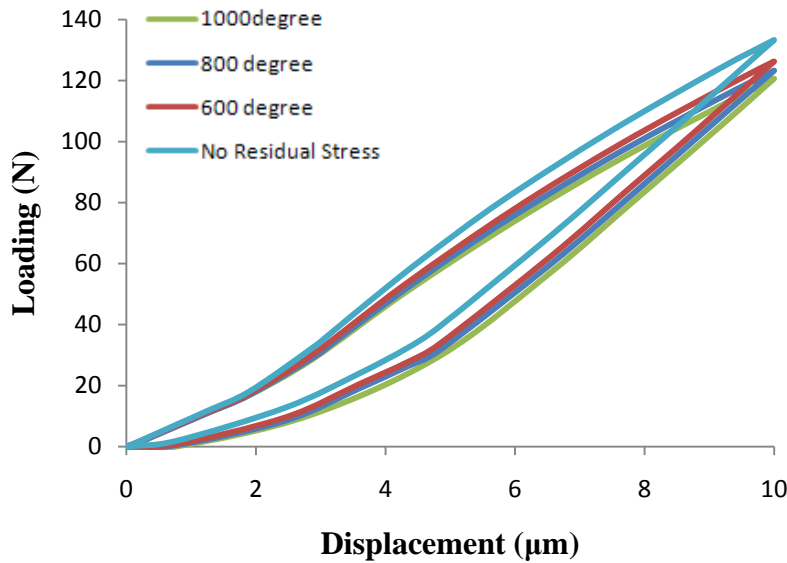


Figure 3.25. Residual stresses effects on loading vs. displacement curves ($E = 1200$ GPa, Sample Curvature = $700 \mu\text{m}$, Coating thickness = $30 \mu\text{m}$, Indentation Depth = $10 \mu\text{m}$).

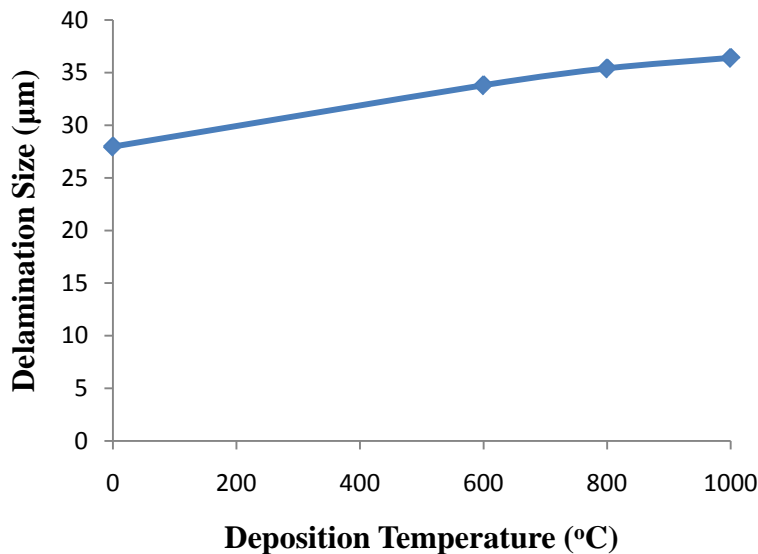


Figure 3.26. Residual stresses effects on delamination sizes ($E = 1200$ GPa, Sample Curvature = $700 \mu\text{m}$, Coating thickness = $30 \mu\text{m}$, Indentation Depth = $10 \mu\text{m}$).

Figure 3.27 shows the coating thickness effect on the interface delamination. The plot indicates that an increase of the coating thickness reduces plastic deformations on a substrate and provides coating-substrate specimens with the resistance for the interface delamination, thus decreasing interface delamination sizes. Examining this plot, it shows virtually no difference in

the delamination size between two models (planar vs. curved). However, other plots have shown two models make noticeable differences in the delamination size (e.g., Figure 3.21). The explanations for this phenomenon are: (1) regarding the case without residual stresses in Figure 3.21, the curvature effect on the delamination size is also very slight. In Figure 3.27, the residual stresses effect is excluded and thus, this result is consistent with the one in Figure 3.21, and (2) the mesh along the interface could also affect delamination sizes.

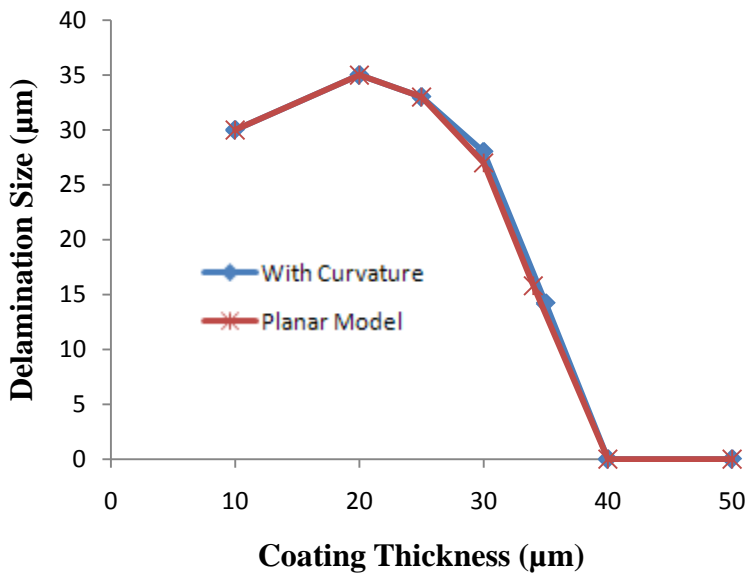


Figure 3.27. Coating thickness effects on delamination sizes ($E = 1200$ GPa, Sample Curvature = 700 μm , Indentation Depth = 10 μm , σ_r (Residual Stresses) = 0 GPa).

It is noted that the curvature has an effect on the interface delamination and the non-planar curved model is more susceptible to the interface delamination, which is consistent with the conclusion of Qasim et al. (2004). In this example, residual stresses and curvature combined effects on the critical loading are explored. Based on the trend depicted in Figure 3.28, it can be concluded that the inclusion of both residual stresses and curvatures significantly facilitate the initiation of the interface delamination. Also, the critical loading decreases with an increase of the deposition temperature.

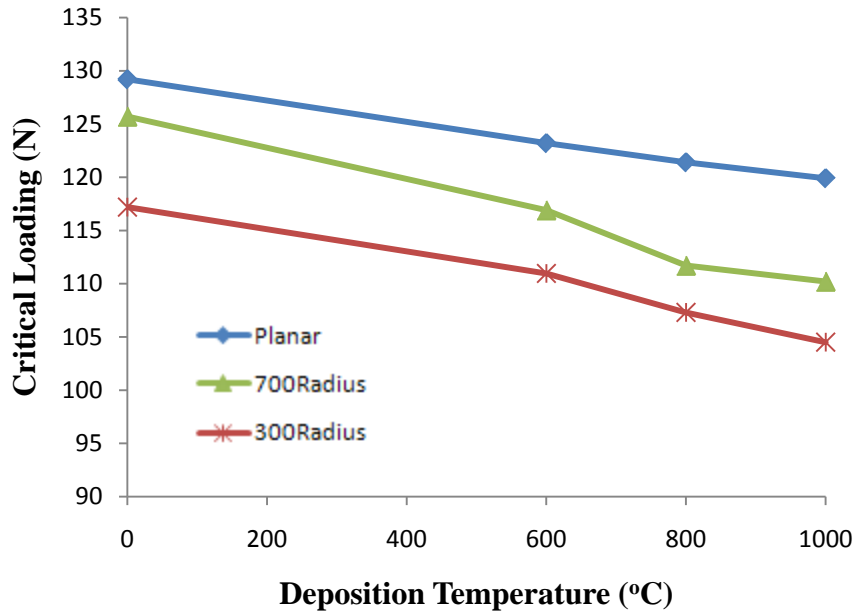


Figure 3.28. Residual stresses and curvature combined effects on the critical loading ($E = 1200$ GPa, Coating thickness = $30 \mu\text{m}$).

Conclusions

In this research, a cohesive zone model is introduced to define interface behaviors between a diamond coating and a tungsten carbide substrate. The residual stresses are also included because they affect the adhesion quality of a coating and a substrate. Simulations of indentations with a spherical indenter indicate that (1) delamination sizes decrease with an increase of a coating Young's Modulus under the same loading condition, (2) delamination sizes increase noticeably with a decrease of a coating thickness; however, a further decrease of a coating thickness to a smaller value results in a reverse regularity, and (3) residual stresses facilitate the interface delamination and reduce the critical loading. Simulations of indentations with a wedge indenter indicate that (1) curvatures slightly affect the loading vs. displacement curve, and models with a curvature have larger interface delamination sizes; also, models with a curvature is more susceptible to the interface delamination, (2) residual stresses will not only

make coating-substrate systems more compliant but also cause more severe interface delamination, and (3) combined residual stresses and curvature effects on the critical loading are significant.

Acknowledgments

This research is supported by the National Science Foundation: 0928627.

References

- Barenblatt, G. I. (1962). Mathematical theory of equilibrium cracks in brittle fracture. In: Dryden, H.L., von Karman, T. (Eds.). *Advances in Applied Mechanics, VII*. Academic Press, New York, 55–125.
- Barenblatt, G. I. (1959). The formation of equilibrium cracks during brittle fracture. General ideas and hypothesis. Axially-symmetric cracks. *Journal of Applied Mathematics Mechanics, 23*(3), 622–636.
- Begley, M. R., Mumm, D. R., Evans, A. G., & Hutchinson, J. W. (2000). Analysis of a wedge impression test for measuring the interface toughness between films/coatings and ductile substrate. *Acta Materialia, 48*, 3211-3220.
- Camacho, G. T. & Ortiz, M. (1996). Computational modeling of impact damage in brittle materials. *International Journal of Solids and Structures, 33*, 2899–2938.
- Cavalli, M. N. (2003). Cohesive zone modeling of structural joint failure. *Ph.D. thesis. University of Michigan, Ann Arbor*.
- Chai, H. & B. R. Lawn. (2004). Fracture mode transitions in brittle coatings on compliant substrates as a function of thickness. *Journal of material Research, 19*, 1752-1761.
- Chai, H. (2003). Fracture Mechanics Analysis of Thin Coating under Spherical Indentation. *International Journal of Fracture, 119*, 263-285.
- Chandra, N., Li, H., Shet, C., & Ghonem, H. (2002). Some issues in the application of cohesive zone models for metal–ceramic interfaces. *International Journal of Solids and Structures, 39*, 2827–2855.
- Dias, A. M. S., Modenesi, P. J., & Godoy, G. C. (2006). Computer simulation of stress distribution during Vickers hardness of WC-6Co. *Materials Research, 8*, 100-104.
- Dugdale, D. S. (1960). Yielding of steel sheets containing slits. *Journal of the Mechanics and Physics of Solids, 8*, 100–104.

- Fredriksson, P. & Larsson, Per-Lennart. (2008). Wedge indentation of thin films modelled by strain gradient plasticity. *International Journal of Solids and Structures*, 45, 5556–5566.
- Gagchi, A., Evans, A. G. (1996). The mechanics and physics of thin film decohesion and its measurement. *Interface Science*, 3, 169-193.
- Gao, Y. F. & Bower, A. F. (2004). A simple technique for avoiding convergence problems in finite elements simulations of crack nucleation and growth on cohesive interfaces. *Modeling and Simulations in Materials Science and Engineering*, 12, 454-463.
- Gerberich, W. W., Tymiak, N. I., Kramer, D. E., Bahr, D. F., & T. J. Wyrobek. (2001). Plastic strain and strain gradient at very small indentation depth. *Acta Materialia*, 49, 1021–1034.
- Geubelle, P. H. & Baylor, J. (1998). Impact-induced delamination of laminated composites: a 2D simulation. *Composites Part B: Engineering*, 29(5), 589–602.
- Grujicic, M., Cao, G., & Fadel, G. M. (2001). Effective materials properties: determination and application in mechanical design and optimization. *Proceeding Institution of Mechanical Engineers, Part L: Journal of Materials: Design and Applications*, 215, 225-234.
- Gunnars, J. & Alahelisten, A. (1996). Thermal stresses in diamond coatings and their influence on coating wear and failure. *Surface Coatings Technology*, 80, 303–312.
- Huang, B., Zhao, M., & T. Zhang. (2004). Indentation fracture and indentation delamination in ZnO Film/Si substrate system. *Philosophical Magazine*, 84, 1233-1256.
- Hu, J., Chou, Y. K., & Thompson, R. G. (2008). A numerical study of interface behavior of diamond coated cutting tools, *Transactions of NAMRI/SME*, 36, 533-540.
- Hutchinson, J. W. & Evans, A. G. (2000). Mechanics of materials: Top-down approaches to fracture. *Acta Materialia*, 48, 125–135.
- Jan, G. M. & Mier, V. (1996). Fracture Processes of Concrete, Assessment of Material Parameters for Fracture Models. CRC press, Boca Raton, Florida, 291.
- Jindal, P. C., Quinto, D. T., & Wolfe, G. J. (1987). Adhesion measurements of chemically vapor deposited and physically vapor deposited hard coatings on WC-Co substrates. *Thin Solid Films*, 154, 361-375.
- Kim, W. K. & Kawai, H. Koyama. (2007). Metal flow in wedge indentation of V- and W-shaped tools. *Journal of Materials Processing Technology*, 189, 392–400.
- Kriese, M. D. & Gerberich, W. W. (1999). Quantitative adhesion measures of multilayer films: part II. indentation of W/Cu, W/W, Cr/W. *Journal of Materials Research*, 14, 3019-3026.
- Liu, P., Zhang, Y. W., Zeng, K. Y., Lu, C. ,& Lam, K.Y. (2007). Finite element analysis of

- interface delamination and buckling in thin film systems by wedge indentation. *Engineering Fracture Mechanics*, 74, 1118–1125.
- Mehrotra, P. K. & Quinto, D. T. (1985). Techniques for evaluating mechanical properties of hard coatings. *Journal of Vacuum Science and Technology A*, 3, 2401- 2405.
- Michler, J. & Blank, E. (2001). Analysis of coating fracture and substrate plasticity induced by spherical indenters: diamond and diamond-like carbon layers on steel substrates. *Thin Solid Films*, 381, 119-134.
- Miranda, P. A., Pajares, F., Guiberteau, Y., Deng, H., Zhao, B., & Lawn, R. (2003). Designing damage- resistant brittle-coating structures: I. bilayers. *Acta Materialia*, 51, 4347–4356.
- Miranda, P. A., Pajares, F., Guiberteau, Y., Deng, H., Zhao, B., & Lawn, R. (2003). Designing damage-resistant brittle-coating structures: II. trilayers. *Acta Materialia*, 51, 4357-4365.
- Mumm, D. R. & Evans, A. G. (2000). On the role of imperfections in the failure of a thermal barrier coating made by electron beam deposition. *Acta Materialia*, 48, 1815-1827.
- Needleman, A. (1987). A continuum model for void nucleation by inclusion debonding. *Journal of Applied Mechanics*, 54, 525–531.
- Needleman, A. (1990b). An analysis of decohesion along an imperfect interface. *International Journal of Fracture*, 42, 21–40.
- Needleman, A. (1990a). An analysis of tensile decohesion along an interface. *Journal of the Mechanics and Physics of Solids*, 38, 289–324.
- Needleman, A. (1997). Numerical modeling of crack growth under dynamic loading conditions. *Computational Mechanics*, 19(6), 463–469.
- Qasim, T., Bush, M., & Hu, X. Z. (2004). A numerical/experimental study of contact damage in non-planar porcelain/metal bilayers. *International Journal of Mechanical Sciences*, 46, 827–840.
- Rice, J. R. & Wang, J. S. (1989). Embrittlement of interfaces by solute segregation. *Material Science and Engineering A*, 107, 23–40.
- She, C. M., Zhang, Y. W., & Zeng, K. Y. (2009). A three-dimensional finite element analysis of interface delamination in a ductile film/hard substrate system induced by wedge indentation. *Engineering Fracture Mechanics*, 76, 2272–2280.
- Souza, R. M. A., Sinatora, G. G., Mustoe, W., & Moore, J. J. (2001). Numerical and experimental study of the circular cracks observed at the contact edges of the indentations of coated systems with soft substrates. *Wear*, 251, 1337-1346.

- Su, C. & Anand, L. (2006). Plane strain indentation of a Zr-based metallic glass: experiments and numerical simulation. *Acta Materialia*, 54, 179–189
- Swain, M. V. & Mencik, J. (1994). Mechanical property characterization of thin films using spherical tipped indenters. *Thin Solid Films*, 253, 204-211.
- Tsui, Y. C., Howard, S. J., & Clyne, T. W. (1994). The effect of residual stresses on the debonding of coatings – II. an experimental study of a thermally sprayed system. *Acta Metallurgical Materials*, 42, 2837-2844.
- Tvergaard, V. (1990). Effect of fibre debonding in a whisker-reinforced metal. *Material Science and Engineering A*, 125 (2), 203–213.
- Tvergaard, V. & Hutchinson, J. W. (1992). The relation between crack growth resistance and fracture process parameters in elastic–plastic solids. *Journal of the Mechanics and Physics of Solids*, 40(6), 1377–1397.
- Vanimisetti, S, K. & Narasimhan, R. (2006). A numerical analysis of spherical indentation response of thin hard films on soft substrates. *International Journal of Solids and Structures*, 43, 6180–6193.
- Wang, J. S., Sugimora, Y., Evans, A. G., & Tredway, W. K. (1998). The mechanical performance of DLC films on steel substrates. *Thin Solid Films*, 325, 163-174.
- Wappling, D., Gunnars, J., & Stahle, P. (1998). Crack growth across a strength mismatched bimaterial interface. *International Journal of Fracture*, 89, 223–243.
- Zisis, Th. & Giannakopoulos, A. E. (2009). Wedge indentation of elastic–plastic layered substrates: designing against contact-induced plasticity. *Computational Materials Science*, 47, 275–285.

CHAPTER 4

CAD AND FEA OF DIAMOND-COATED END MILLS WITH CZM INCLUSION

Abstract

The objective of this chapter is to investigate the geometry effects on the deposition residual stresses in diamond-coated end mills, especially interfacial stresses. Computer-aided design (CAD) software is employed to create the 3D solid models of diamond-coated macro/micro end mills. CAD models are exported into the finite element analysis (FEA) software to simulate deposition residual stresses in diamond-coated end mills after the deposition process; the results indicate that the residual stresses on diamond-coated end mills can be significantly large. In addition, the cross-sections of end mills are extracted from their 3D CAD models, and 2D FEA is used to simulate the residual stresses of cross-sections in order to compare interface stresses around cutting edges. The methodologies applied on diamond-coated macro end mills are further developed and conducted on their micro counterparts. The cohesive zone model (CZM), characterized by a traction-separation law, is also incorporated into the 2D macro end mill cross-sections. Stress transformations of the interface stresses of end mill cutting edges have been conducted to quantitatively evaluate the end mill geometry effects. The obtained results show that (1) 3D FEA results indicate high stresses concentrate on the cutting edge, and the high tensile radial stresses can affect adhesion quality, (2) the edge radius is the most dominant geometric parameter affecting the deposition residual stresses; also, the coating thickness ranks second, only to the edge radius, for effects on the deposition residual stresses, (3) the macro-level geometric parameters, such as the helix angle, the rake angle, and the relief angle,

slightly alter the interface stresses around cutting edges, (4) when the macro size is scaled down to a micro level, the interfacial residual stresses are slightly increased, and (5) the inclusion of a cohesive zone reduces the interface stresses compared to the models without a cohesive zone.

Introduction

The actions of each intermittent cutting edge are important features of all milling operations. Cutting times are small fractions of a second and such actions repeat several times, involving both thermal and mechanical fatigue of the tool (Trent & Wright, 2000). There are two major categories of milling operations: facing milling and peripheral milling, and two general types of milling cutters: solid and the inserted-tooth cutters. Considering the wide range of materials that must be machined, an ideal milling cutter should have high abrasion resistance, hardness, and edge toughness (Walker, 2000). With regard to end milling cutters, they could generate two workpiece surfaces at the same time, and cutting edges are located on both the end face and the periphery of a cutter body. They are usually used in facing, profiling, slotting, shoulder, slabbing, and plunging operations. End mills are considered to be the most versatile milling tools and they are a more robust version of drills when producing hollow shapes such as dies cavities (Stephenson & Agapiou, 1997; Trend & Wright, 2000). End mill geometric parameters (Figure 4.1 and Table 4.1), such as the diameter and the flute length, must match the dimensions of pockets to be machined. The tooth edge geometry, the rake angle, the relief angle, and the flute forms are all important parameters of end mills (Stephenson & Agapiou, 1997).

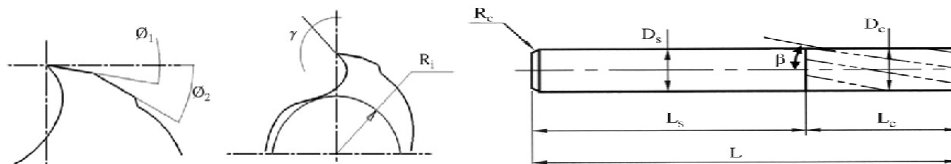


Figure 4.1. (a) Section dimensions and (b) external shape dimensions of end mill (Kim, Park and Ko, 2008).

Table 4.1

Parameters to Define End-milling Cutter Dimensions

ϕ_1	<i>First Relief Angle</i>	ϕ_2	<i>Second Relief Angle</i>
γ	Rake Angle	R_i	Radius of Inner Circle
R_c	Chamfer Length	D_s	Shank Diameter
β	Helix Angle	D_c	Cutter Diameter
L_c	Cutter Length	L_s	Shank Length
L	Overall Length	N_f	Number of Flutes

The coating, material, and shape of an end mill are the critical factors in improving the cutter performance, whereas the shape mainly affects the machining accuracy and the dynamic stability. The shape elements of an end mill include the relief angle, the rake angle, and the helix angle; these are the main determinants of the performance of end mills (Ehmann, 1990; Tlustý et al., 1991; Kanda et al., 1995; Gunnars et al., 1996; Gabler et al., 2000; Kim and Ko, 2002; Kim, Park & Ko, 2008). The helix angle dramatically affects the end mill cutter performance (Stephenson & Agapiou, 1997). Regarding the design of an end mill, certain difficulties lie in modeling the exact three-dimensional shape of an end mill since parts of the shape cannot be determined until actual machining. It is necessary to fabricate a physical prototype and conduct cutting tests to improve the cutter shape if a 3D end mill solid model is not available (Kim, Park & Ko, 2008). In order to predict the sectional profile of an end mill, it is important to obtain the helical groove shape as accurately as possible, because it determines the critical end mill geometric parameters, such as the rake angle, which substantially affects the machining performance. One useful methodology to predict the profile curve for the helical groove of an

end mill is the direct method. The “direct method” means the approximation of the grinding wheel as a set of a finite number of thin disks. The intersections between the primitive wheels and the tool workpiece are calculated to obtain a profile curve (Kim, Park & Ko, 2008). By using the “direct method”, Friedman and Meister (1973) studied the profile of a helical slot machined by a form-milling cutter. Kaldor et al. (1988) conducted the geometric analysis and software development for the design of milling cutters and grinding wheel profiles. Later, Ko (1994) conducted the geometrical analysis of helical flute grinding and applied it to end mills. Kim and Ko (2002) proposed the design and manufacturing technologies for end mills and the wheel was properly determined by using the developed simulation program.

When referred to the shapes of an end mill, they can be basically categorized into five types (see Figure 4.2): square end mills, corner chamfer end mills, corner radius end mills, ball nose end mills, and corner rounding end mills. Their machining properties and applications vary from each other. For a square end mill, it has a true square angle; thus, its corner is fragile. For a corner chamfer end mill, it displays resistant corners, good cutting in roughing operations, and suitability for coated tools and long tool life. Similarly, a corner radius end mill, which is mainly used for aeronautics use and roughing operations, has high corner resistance; therefore, it is suitable for coated tools. A ball nose end mill is usually suitable for molds, dies, and finishing operations. When a ball nose end mill is used to machine a workpiece, the cutting speed at the center is equal to 0, leading to a poor surface quality on soft materials. Finally, a corner rounding end mill is employed to round surfaces. The corner of such end mills is also fragile.

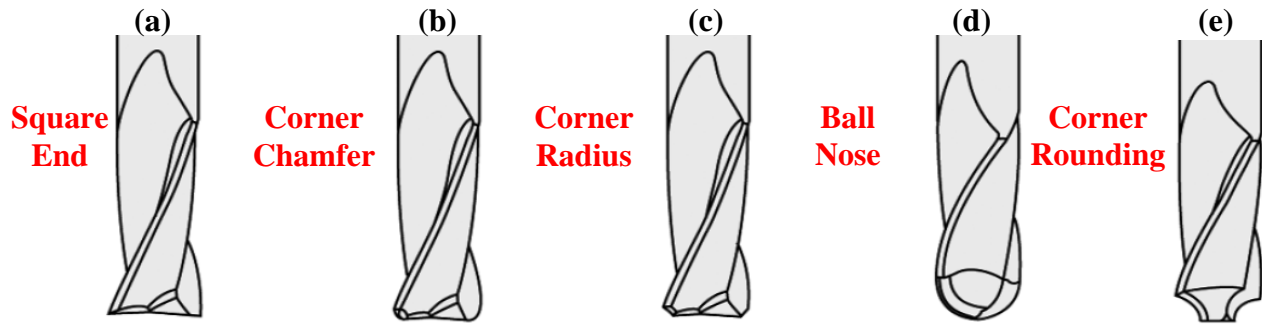


Figure 4.2. Different types of end mills: (a) square end end mill, (b) corner chamfer end mill, (c) corner radius end mill, (d) ball nose end mill, and (e) corner rounding end mill (<http://www.hssforum.com/MillingEN.pdf>).

Recently, micro-manufacturing is a rapidly growing worldwide industry estimated at \$60 billion (Bruno et al., 1995; Torres et al., 2009). Mechanical micro machining begins to enjoy an increasing attention due to its promising fabrication process (Kim et al., 2007; Jun et al., 2007). Micro end milling is also a material removal process that can generate a high aspect ratio in a single step (Liu et al., 2004; Kobayashi, 2005; Williams et al., 2005; Torres et al., 2009). In addition, mechanical micro machining is not limited to special clean room environments, and it is, therefore, more affordable and simpler to carry out. It is also compatible with various engineering materials such as polymers (Damazo et al., 1999), metals, metal alloys (Damazo et al., 1999; Kim, Bono & Ni, 2002; Isomura et al., 2003; Jackson, Robinson & Ahmed, 2006), and pre-sintered powder ceramics (Isomura et al., 2003; Jeon & Pfefferkorn, 2007). Even though there are many advantages of micro end milling, there are challenges for industrial practitioners when scaling down end mills to microscopic sizes. One typical challenge is that sintered tungsten carbides with a cobalt binder are quite brittle so micro-scaled features of end mills are easily damaged. This results in rapid tool degradation. Additionally, micro tools with small diameters have low flexural stiffness and strength (Kim, Bono, & Ni, 2002; Liu et al., 2004; Kobayashi, 2005; Torres et al., 2009). Due to many beneficial mechanical and tribological properties, for example, chemical inertness, low friction and high hardness, diamond coatings have been

applied to micro end mills to increase the tool operational life as well as the performance (Gabler, Schafer, & Westermann, 2000; Jackson et al., 2004; Sein et al., 2004; Torres et al., 2009).

Though diamond-coated end mills have a potential for high performance milling, machining performance evaluations of complex-shaped diamond-coated tools, such as diamond-coated end mills and drills, have not been studied in detail (Kandaa et al., 1995).

In this study, a method to generate diamond-coated four-flute macro/micro end mills is developed by using the commercial CAD software Solidworks. ABAQUS is also employed to simulate 3D deposition residual stresses generated in diamond-coated end mills. In addition, 2D approximation of stress analyses is proposed to simulate end mill cross-sections, and the stresses around cutting edges are extracted and transformed to quantitatively evaluate the local interface stresses of different components. The 3D solid modeling methodology is also utilized to generate end mills with different macro-level geometric parameters such as the helical angle, the rake angle, and the relief angle. Micro-level geometric parameters, such as the edge radius and the coating thickness, are also investigated by the finite element analysis (FEA) software to quantify and evaluate their effects on the residual stresses distributions. The same approaches are repeated and applied on diamond-coated micro end mills to investigate the residual stresses distributions after the size is scaled down. Finally, for the 2D case, a cohesive zone model (CZM) is incorporated into the macro end mill cross-section. The simulation processes above are repeated to address the cohesive zone effect on the residual stresses distributions.

Solid Modeling of 3D Diamond-Coated Four Flutes Corner Chamfer Macro End Mills

3D solid modeling procedures of a diamond-coated end mill in Solidworks can be summarized as follows. To begin with, a helix curve with a specified helix angle and a pitch (length advancement per revolution) is created and then, the flute cross-section is generated

according to the geometric relationship of a specific end mill (Kim, Park & Ko, 2008). Then, the former designed helix curve is used as the sweep trajectory and the flute cross-section is swept along the helix curve to create the end mill flute body. For the next step, the extrude-cut function is used to create a cut feature to remove a portion of the head to develop one portion of the cutter head. With this created as one portion of the cutter head, a pattern feature is used to produce another three portions of the cutter head to form 4 cutting edges on the end mill head. Then, a small hole is drilled with a specified depth and a diameter on the top of the end mill. All cutting edges on the head and the peripheral edges are rounded, and chamfer the peripheral edges on the cutter head. Finally, the shank is added into the 3D end mill model to form a completed end mill body. With respect to modeling of the diamond-coated end mill, the established end mill model serves as the substrate, on which the revolve-cut and the shell features are employed to generate the diamond coating with a given coating thickness and an edge radius. Then, the completed end mill substrate and the coating models are assembled to attain a diamond-coated four-flute corner chamfer macro end mill. Figure 4.3 illustrates the 3D view of a completed diamond-coated four-flute corner chamfer macro end mill. Details regarding the modeling procedures are described in Appendix B.

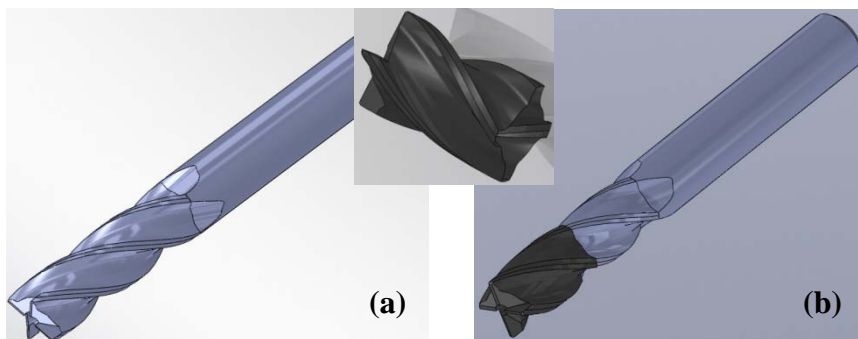


Figure 4.3. (a) a completed end mill solid model and (b) a diamond-coated end mill.

Finite Element Analysis of Diamond-Coated Macro End Mill Deposition Residual Stresses

3D Diamond-Coated Macro End Mill Residual Stress Analysis

With regard to the 3D simulations process, the above completed 3D model is imported from Solidworks to ABAQUS, where the assembly and merging process are conducted. As for the material properties, boundary conditions, element properties, and deposition temperature definition, they are the same as the ones discussed in Chapter 2. Since high residual stresses occur on the cutting edge areas when the deposition temperature is returned to the room temperature, the mesh is further refined in these areas with a 0.05 mm element size (Figure 4.4 (b)). The total number of elements in this end mill is 917360.

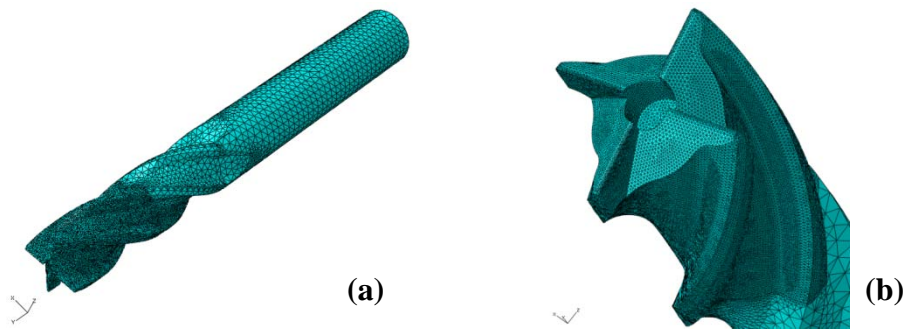


Figure 4.4. Mesh distributions on a diamond-coated macro end mill: (a) whole model (b) around head.

The finite element simulation can be executed according to the above model setup. A typical example is illustrated in Figure 4.5 and geometric parameters of this end mill are 6 mm diameter, 18.85 mm cutter length, 30° helix angle, 5° 1st relief angle, 6° rake angle, 5 μm edge radius, 5 μm coating thickness, and 29 mm shank length. Figure 4.5 shows the longitudinal stress contours of a diamond-coated end mill. It can be noted that the magnitude of longitudinal stresses on the coating surface with the moderate curving is around 3 GPa in compression, which is consistent with the results attained from the biaxial stress analysis. It is reported that since the compressive stresses inhibit crack initiation and growth to a certain level, suitable high

compressive residual stresses in PVD coated surfaces are tribologically beneficial (Wiklund, Gunnars & Hogmark, 1999). Quinto, Santhanam and Jindal (1988) also indicated that the compressive residual stresses within the plane of a coating are beneficial to the surface fracture strength which translates to a better performance, particularly in milling. However, at the same time, it is important to notice that very high compressive stresses in a coated surface may result in buckling, and exert effects at the corners, holes, or surface topography asperities (Wiklund, Gunnars & Hogmark, 1999). Alternatively, the substrate receives tensile stresses and the stress values are comparatively higher on the coated area. For the area away from the coating, the tensile stresses on the substrate are generally small. Further noted is that the deposition stresses concentrate around a cutting edge, which is consistent with the drill results reported by Miao et al. (2009).

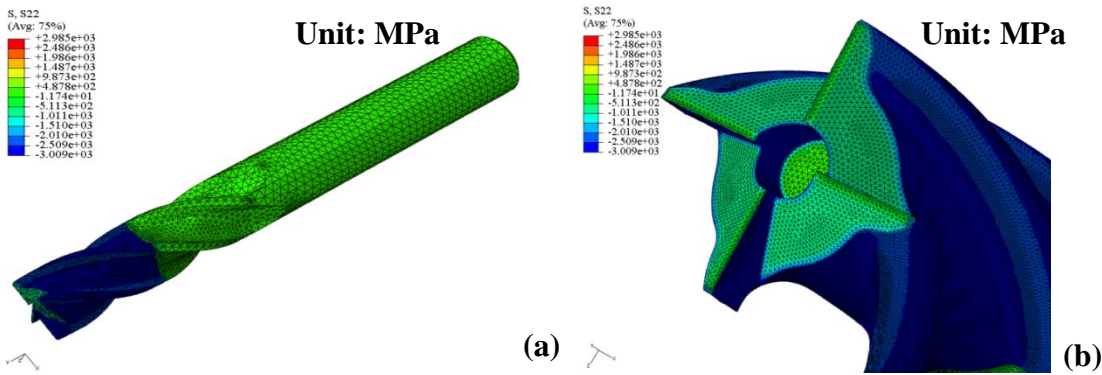


Figure 4.5. Longitudinal stress distributions in a diamond-coated macro end mill (a) entire end mill (b) around end mill head.

2D Approximation

2D end mill cross-sections can be generated using a plane normal to a peripheral cutter and a workpiece plane, defined by considering the relative motion at a local end mill edge.

Figure 4.6 demonstrates how to employ the principle of end milling processes to define the workpiece plane, as well as the plane normal to the cutter, to construct the cross-section. In this

specific cross-section, the rake angle is equal to 6° and 5° for a 1st relief angle. The highlighted cross-section profile (Figure 4.6 (c)) can be extracted and exported to ABAQUS for 2D FEA simulations of deposition residual stresses analysis with a 2D plain-strain assumption. The edge radius and coating layer, uniformly all around, can be generated in the ABAQUS. The material properties and the deposition temperatures are the same as in the 3D analysis. In addition, as in the case of 3D simulations, the cutting edge areas also receive further refined meshing, with a $0.03 \mu\text{m}$ element size. With regard to the boundary conditions, one corner is fully constrained and another corner, diagonal to the corner mentioned, is constrained on only one direction (Figure 4.6).

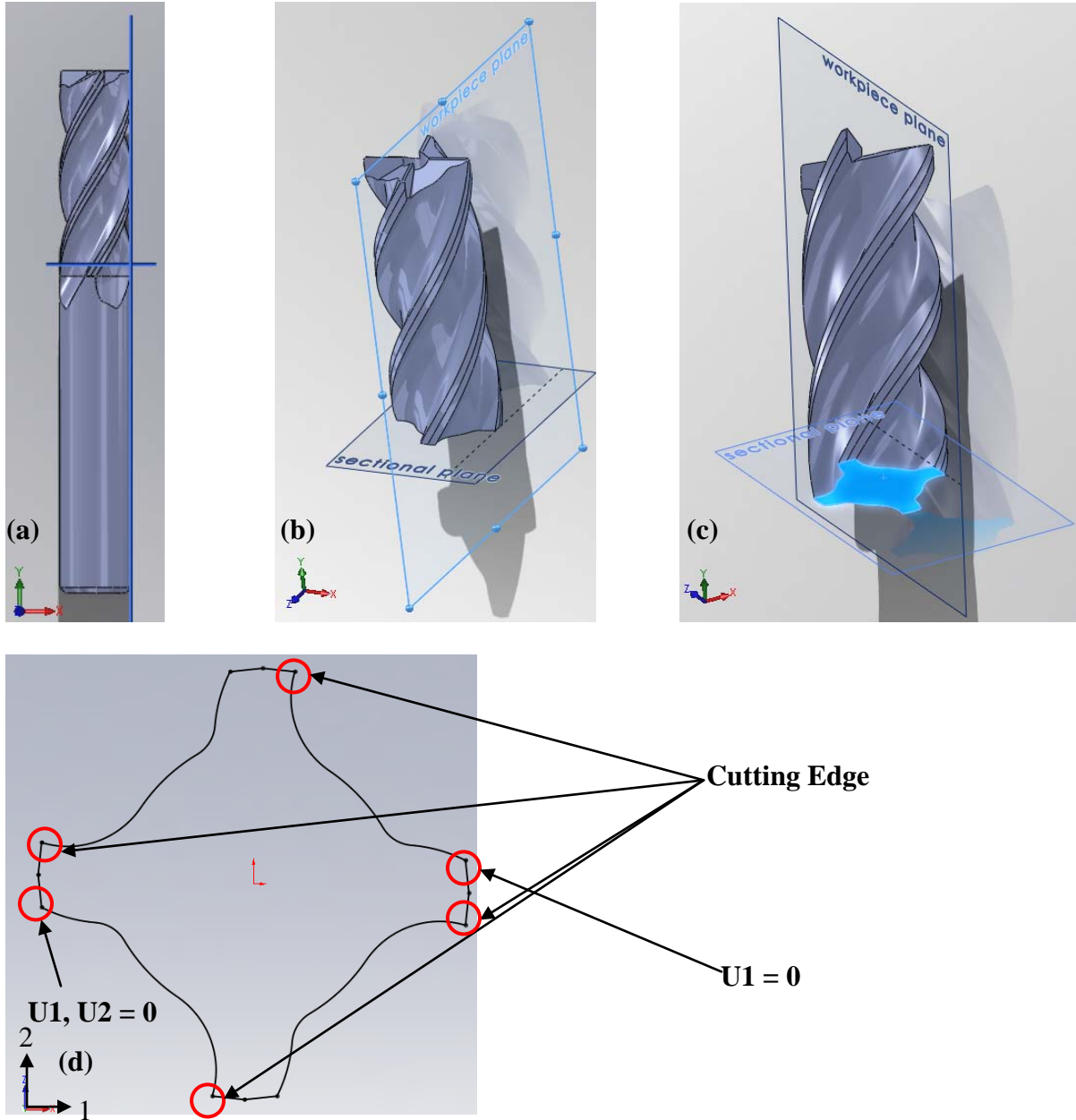


Figure 4.6. 2D cross section of an end mill for FEA: (a) sectional plane specification and workpiece plane view#1, (b) sectional plane specification and workpiece plane view#2, (c) highlighted cross section area, and (d) extracted 2D cross section.

With these steps accomplished, the extracted 2D cross-section (Figure 4.6 (d)) can be exported into ABAQUS for the 2D deposition residual stresses analysis. Figure 4.7 illustrates the maximum principal stress contours, both the entire model and the edge rounding area, of a

typical end mill without a cohesive zone inclusion. The maximum principal stresses distributed on the cross-sections are in the neighborhood of 2 GPa to 3 GPa. It can be further noted that the cutting edge area, where the 3 μm edge rounding is located, receives high stresses.

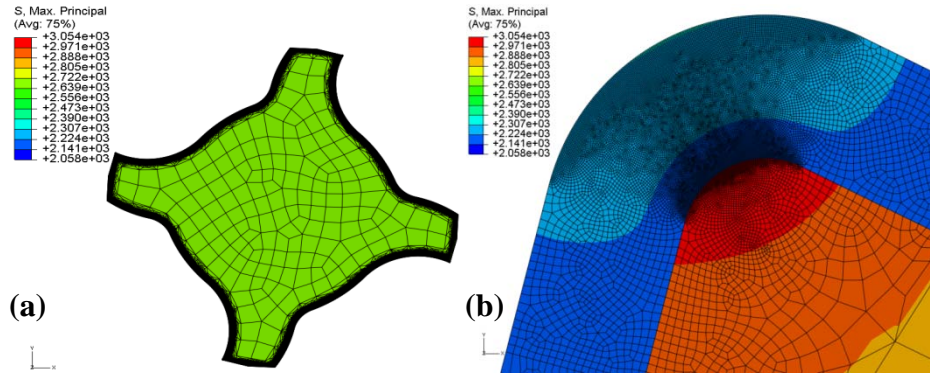


Figure 4.7. Maximum principal stress contour of a 2D diamond-coated macro end mill cross section (a) entire model (b) around the cutting edge.

With the obtained 2D FEA results, the interface stresses of the end mill can be extracted and transformed by employing the Mohr's circles concept in order to quantitatively address the interface stresses around a cutting edge. Three stress components, the radial normal stress (σ_r), the circumferential normal stress (σ_θ), and the shear stress ($\tau_{r\theta}$), are introduced by changing the Cartesian coordinate system to a local polar coordinate system around a cutting edge (Miao et al., 2009).

Diamond-Coated Macro End Mill Geometric Parameters Effect

The CAD program is applied to generate end mills with different helix angles (Figure 4.8) using the developed modeling methodology. Among the end mill macro-level geometric parameters, the helix angle is selected for further study because for end mills, the helix angle strongly affects cutter performance (Stephenson & Agapiou, 1997). In addition to the helix angle, the rake angle and 1st relief angle effects are also tested with values of -6° , 0° , 6° for the rake angle, and 5° , 7° , 9° for the 1st relief angle. With regard to the micro-level of end mill geometry,

since the coating thickness is the key factor improving the cutter performance, it is tested with 5 μm , 10 μm , 15 μm and 30 μm coating thickness. Edge radii are tested at 3 μm , 7 μm and 15 μm since the edge radius has already been proven to be an important factor affecting the residual stresses developed around cutting edge (Hu, Chou & Thompson, 2007; Miao et al., 2009).

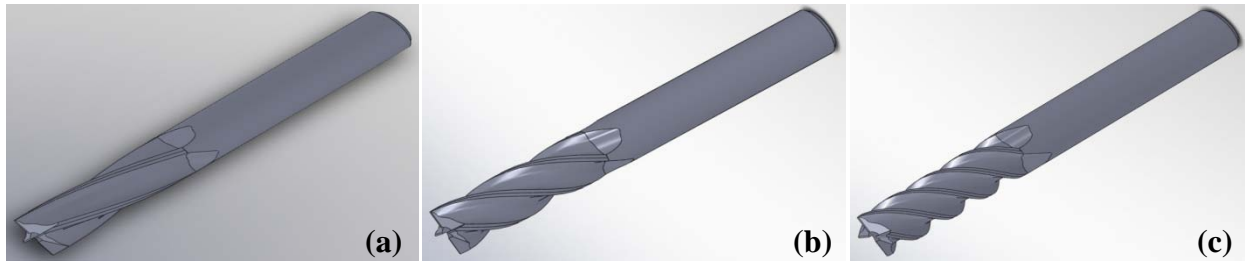


Figure 4.8. End mills with different helix angles (a) 15° (b) 30° (c) 45°

Cross-sections are generated in the above models, and the deposition residual stress finite element simulation is conducted again. Similarly, the interface stress data is extracted and transformed again to evaluate sectional profiles. The FEA results show that the helix angle's effect on interface stresses is negligible. Similarly for the rake angle and the relief angle, their effects on radial normal stresses are also minor, but they slightly affect circumferential stress (σ_{θ}). Alternatively, it can be noted that the edge radius (r_e) significantly alters interface stresses compared with the helix angle, the rake angle and the relief angle (Figure 4.9). With regard to the radial normal stress (Figure 4.9(a)), the maximum stress increases from 0.75 GPa for 15 μm r_e to 1.45 GPa for 3 μm r_e . As for the circumferential stress (Figure 4.9(b)), the maximum stress increases from 3.08 GPa for 15 μm r_e to 3.67 GPa for 3 μm r_e . In addition, models with a large edge radius have smooth stress gradients along the cutting edge. As for shear stresses, the stress magnitude is relatively smaller and stress reductions by edge hone are also evident: 0.84 GPa for 3 μm r_e and 0.36 GPa for 15 μm r_e . In our previous study, Qin et al. (2009) proved that an increase of a coating thickness significantly increases interface stresses; thus, it is important to quantify the coating thickness effect on deposition residual stresses around the cutting edges of

diamond-coated end mills as well. As for the coating thickness effect (Figure 4.10), radial normal stresses increase from 0.75 GPa for 5 μm to 1.51 GPa for 30 μm , and circumferential stresses increase from 3.08 GPa for 5 μm to 3.86 GPa for 30 μm .

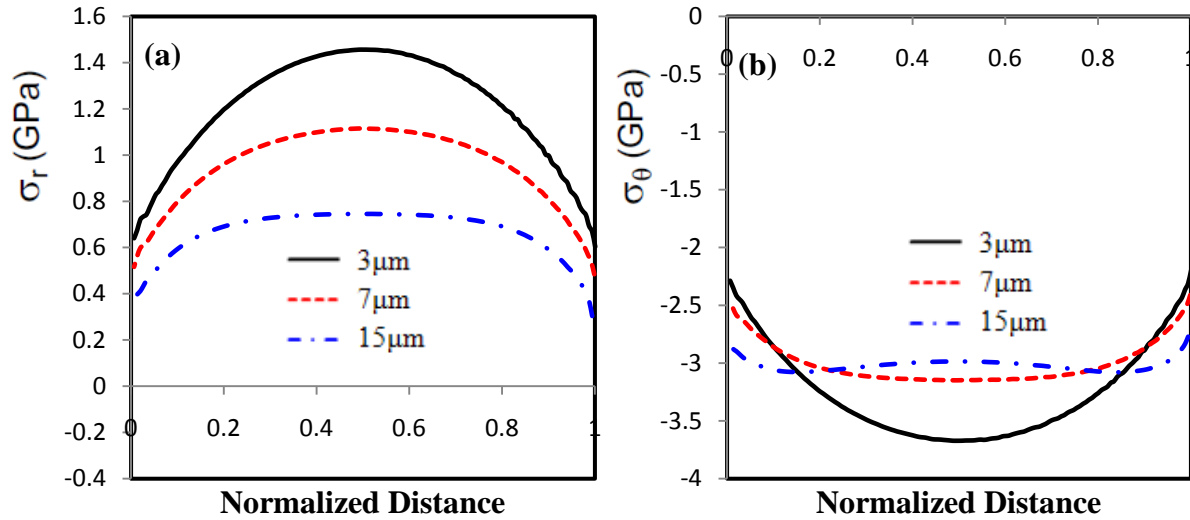


Figure 4.9. Edge radius effect on interface stresses of 2D diamond-coated macro end mills (a) radial normal stresses (b) circumferential stresses (helical angle = 30° and coating thickness = 5 μm).

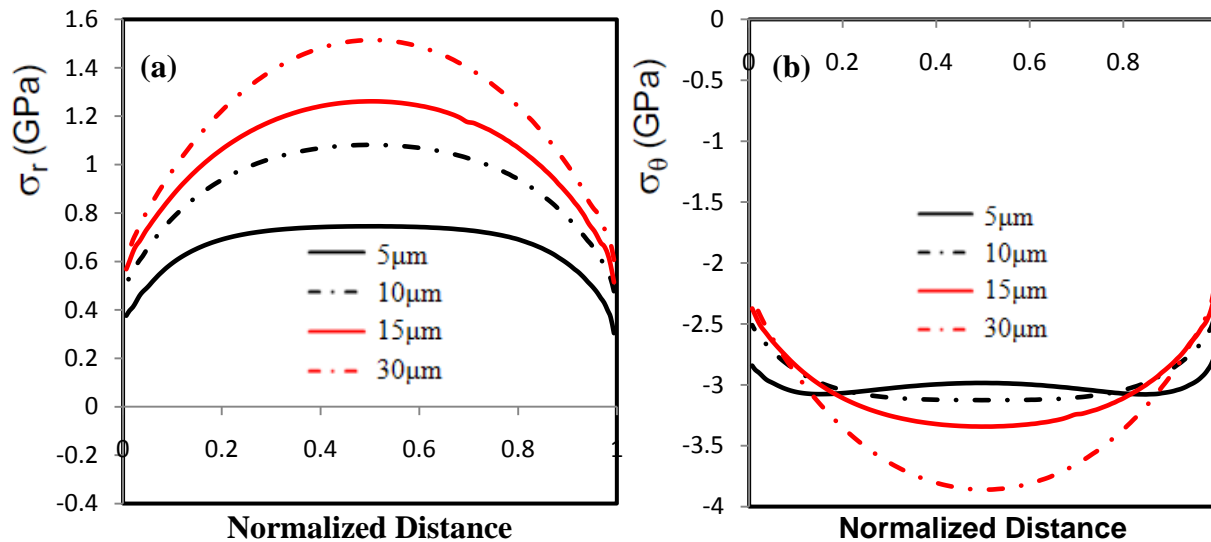


Figure 4.10. Coating thickness effect on interface stresses of 2D diamond-coated macro end mills (a) radial normal stresses (b) circumferential stresses (r_e (edge radius) = 15 μm and helical angle = 30°).

With the attained interface stress data, all maximum values of three stress components for end mill cross-sections with different geometric parameters are documented in several tables. Table 4.2 and Table 4.3 depict the maximum interface stress comparisons of 2D diamond-coated macro end mills with different edge radii and coating thicknesses. It can be noted that an end mill with the smallest edge radius, i.e., 3 μm r_e , has the largest $\sigma_{r_{\max}}$ and $\sigma_{\theta_{\max}}$, 1.45 GPa and 3.67 GPa, respectively. On the contrary, the end mill with the largest edge radius, i.e., 15 μm r_e , has the smallest $\sigma_{r_{\max}}$ and $\sigma_{\theta_{\max}}$, 0.75 GPa and 3.08 GPa, respectively. This is consistent with our previous results concerning edge radius effects on diamond-coated drills (Miao et al., 2009) and diamond-coated inserts (Hu, Chou & Thompson, 2007). As for the coating thickness, the end mill with the smallest coating thickness, i.e., 5 μm , has the smallest $\sigma_{r_{\max}}$ and $\sigma_{\theta_{\max}}$, 0.75 GPa and 3.08 GPa, respectively. Then, the end mill with the largest coating thickness, i.e., 30 μm , has the largest $\sigma_{r_{\max}}$ and $\sigma_{\theta_{\max}}$, 1.51 GPa and 3.86 GPa, which agrees with our previous results (Qin et al., 2009). Regarding the magnitude of wedge angles, the end mill and the drill have the largest (79.4°) and the smallest (54°) values, respectively. The wedge angle of an insert (79°) is only second to that of an end mill. For the helix angle, its effect on end mill deposition residual stresses is quite minor, which is also consistent with our previous results on the helix angle effect on diamond-coated drills (Miao et al., 2009). With regard to the rake angle and the relief angle effects on end mill residual stresses, their effects are also slight but more remarkable than that of the helix angle.

Table 4.2

Maximum Radial Normal Stress for Different Edge Radii

Edge Radius Effect on Interfacial Stress (Coating Thickness = 5 μ m)				
Edge Radius	Radial Normal Stress (Unit: GPa)		Circumferential Stress (Unit: GPa)	
	End Mill	Drill	End Mill	Drill
3 μ m	1.45	1.41	3.67	3.11
7 μ m	1.11	1.08	3.14	2.80
15 μ m	0.75	0.73	3.08	2.94

Table 4.3

Maximum Radial Normal Stress for Different Coating Thicknesses

Coating Thickness Effect on Interfacial Stress ($r_e = 15\mu$ m)				
Coating Thickness	Radial Normal Stress (Unit: GPa)		Circumferential Stress (Unit: GPa)	
	End Mill	Insert	End Mill	Insert
5 μ m	0.75	0.6	3.08	2.61
10 μ m	1.08	0.84	3.13	2.6
15 μ m	1.26	1.0	3.34	2.73
30 μ m	1.51	1.25	3.86	3.09

Finite Element Analysis of Diamond-Coated Micro End Mill Deposition Residual Stresses

Modeling Process and Cross Section Generation of Diamond-Coated Micro End Mills

The 3D solid modeling process of micro end mills is identical with macro end mill modeling process. The only difference is that all of the geometric parameters, except the edge

radii and coating thicknesses of macro end mills, are scaled down 50 times to get micro end mills. Figure 4.11 provides an illustration of a micro end mill geometric shape as well as its dimension specifications. From the illustration, it can be noted that the micro end mill geometric shape is almost the same as its macro counterparts, and the only difference is the size for each of them. With this completed micro end mill, it can be imported into ABAQUS again for 3D deposition residual stress simulations.

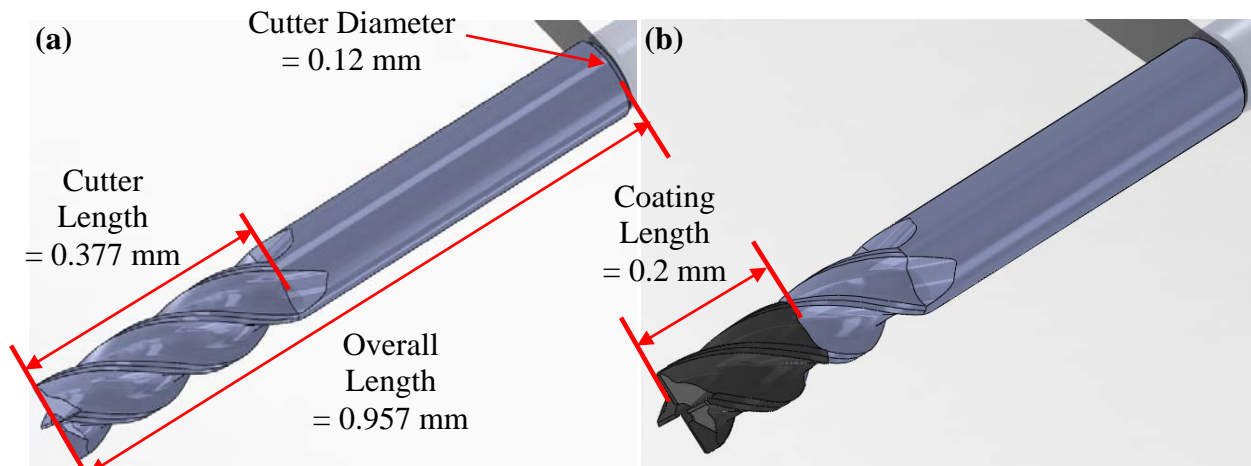


Figure 4.11. (a) a micro end mill substrate and (b) a diamond-coated micro end mill.

3D Diamond-Coated Micro End Mill Analysis

The methodology of 3D simulations of diamond-coated micro end mills is based on the simulations of diamond-coated macro end mills. As for material properties, boundary conditions, element properties and mesh distributions, they are the same as their macro counterparts.

Based on the above model setup, finite element simulations can be achieved. The diamond-coated micro end mill geometric parameters are 0.12 mm for the diameter, 0.377 mm for the cutter length, 30° for the helix angle, 5° for the 1st relief angle, 6° for the rake angle, 0.5 μm for the edge radius, 1 μm for the coating thickness, and 0.58 mm for the shank length. Figure 4.12 shows the plot for longitudinal stress contours of a diamond-coated micro end mill. It can be noted that the magnitude of longitudinal stresses on the coating surface with moderate curving is

still around 3 GPa in compression. By comparing the maximum longitudinal compressive stress of a micro end mill with a macro end mill, it can be concluded that the maximum compressive stress of a micro end mill is slightly larger than that of a macro end mill, which indicates that if a macro end mill is scaled down to a micro size, corresponding compressive stresses of it are increased.

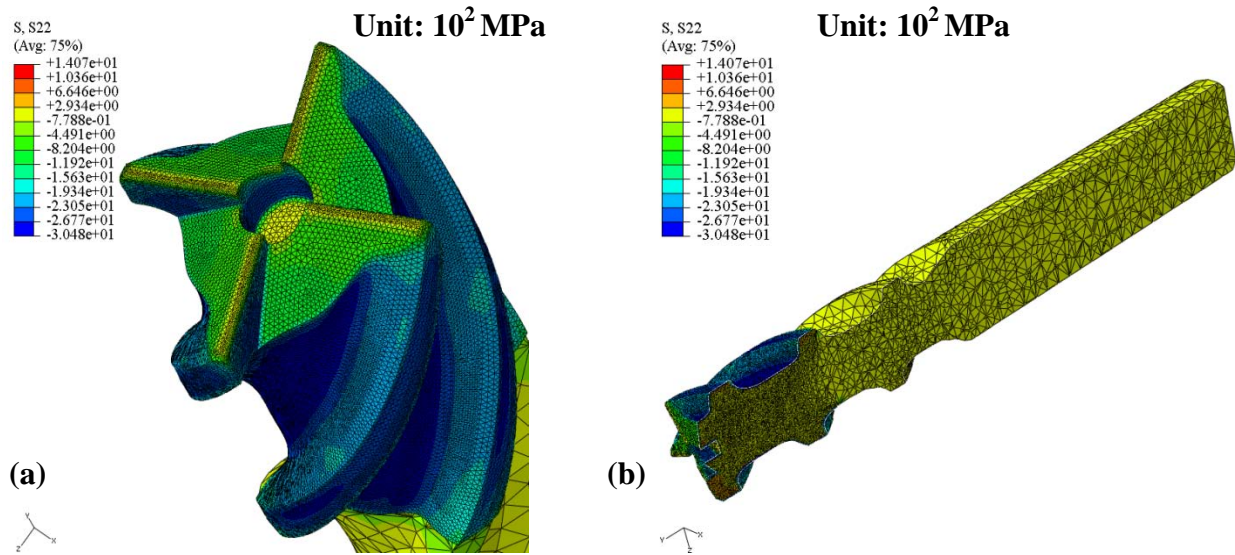


Figure 4.12. Longitudinal stress distributions in a diamond-coated micro end mill (a) around end mill head (b) sectional view.

Diamond-Coated Micro End Mill 2D Cross Section FE Simulation

Similarly, in terms of the methodology to generate 2D cross-sections, identical processes on generating macro end mill 2D cross-sections have been repeated. After the cross-section is determined, it can be extracted and exported into ABAQUS for 2D FE simulations of deposition residual stress analysis with an assumption of a 2D plain-strain condition. The edge radius and coating layer, uniformly all around, can be generated in ABAQUS. The operations in ABAQUS are also replicated according to the FEA of macro end mill cross sectional. Due to the geometric symmetry of end mill cross-sections, a quarter part of a micro end mill cross-section is extracted for FEA.

For the modeling parameters of a micro end mill, geometric parameters are scaled down by 50 times, except a edge radius and a coating thickness. The edge radius range under investigation here is $0.5 \mu\text{m} \sim 1 \mu\text{m}$, and the coating thickness is $1 \mu\text{m}$. There are two reasons for selecting these values: (1) our previous study in FE simulations of diamond-coated drills has shown that if all geometric parameters are equally, proportionally scaled down, interface stresses as well as overall stresses remain almost the same; this phenomenon is supposed to be the same as the micro end mill model, and (2) if edge radii and the coating thickness are scaled down by 50 times, which means $0.06 \mu\text{m} \sim 0.3 \mu\text{m}$ for edge radii and $0.1 \mu\text{m}$ for the coating thickness, the associated microscopic size will be too difficult to achieve from fabrication perspectives. In previous chapters, it has been concluded that the edge radius is the most dominant factor affecting interface stresses; thus, it is more critical to know the edge radius effect on micro end mills than the effects of other factors.

FE simulations are applied on completed micro end mill sectional profiles and Figure 4.13 provides maximum principal stress contours on a 2D micro end mill. Figure 4.13 (b) is a local view of the edge rounding area. As for the geometric parameters of this cross-section, they are generated from a diamond-coated micro end mill with a 0.12 mm diameter, a 0.377 mm cutter length, a 30° helix angle, a 5° relief angle, a 6° rake angle, a $0.5 \mu\text{m}$ edge radius, a $1 \mu\text{m}$ coating thickness, and a 0.58 mm shank length. It can be seen that stresses developed on cross-sections is in the range of 2 GPa to 3 GPa. Further noted is that the cutting edge area receives exceptionally high stresses compared with other locations.

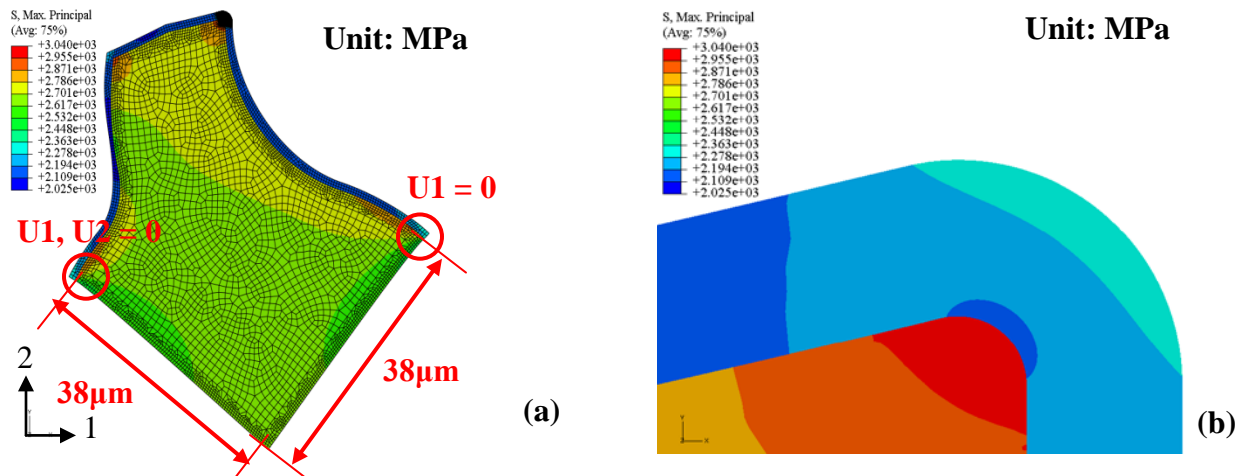


Figure 4.13. Maximum principal stress contours in a 2D diamond-coated micro end mill cross section (a) entire model (b) around the cutting edge.

The extraction and transformation of interface stresses are repeated according to the methodologies in previous paragraphs. Figure 4.14 provides a clear quantitative comparison between a 2D diamond-coated micro end mill and a 2D diamond-coated macro end mill in terms of their radial normal stresses and circumferential stresses. For the micro end mill, it can be seen that the edge radius significantly affects interface stresses, and for radial normal stresses (Figure 4.14 (a)), the maximum stress increases from 1.12 GPa for $1.0 \mu\text{m } r_e$ to 1.52 GPa for $0.5 \mu\text{m } r_e$. As for circumferential stresses (Figure 4.14(b)), the maximum stress increases from 3.12 GPa for $1.0 \mu\text{m } r_e$ to 3.92 GPa for $0.5 \mu\text{m } r_e$. Through the maximum stress comparisons between macro and micro end mills (Table 4.4), it can be said that the maximum radial normal stress as well as the circumferential stress of micro end mills are larger than those of macro end mills.

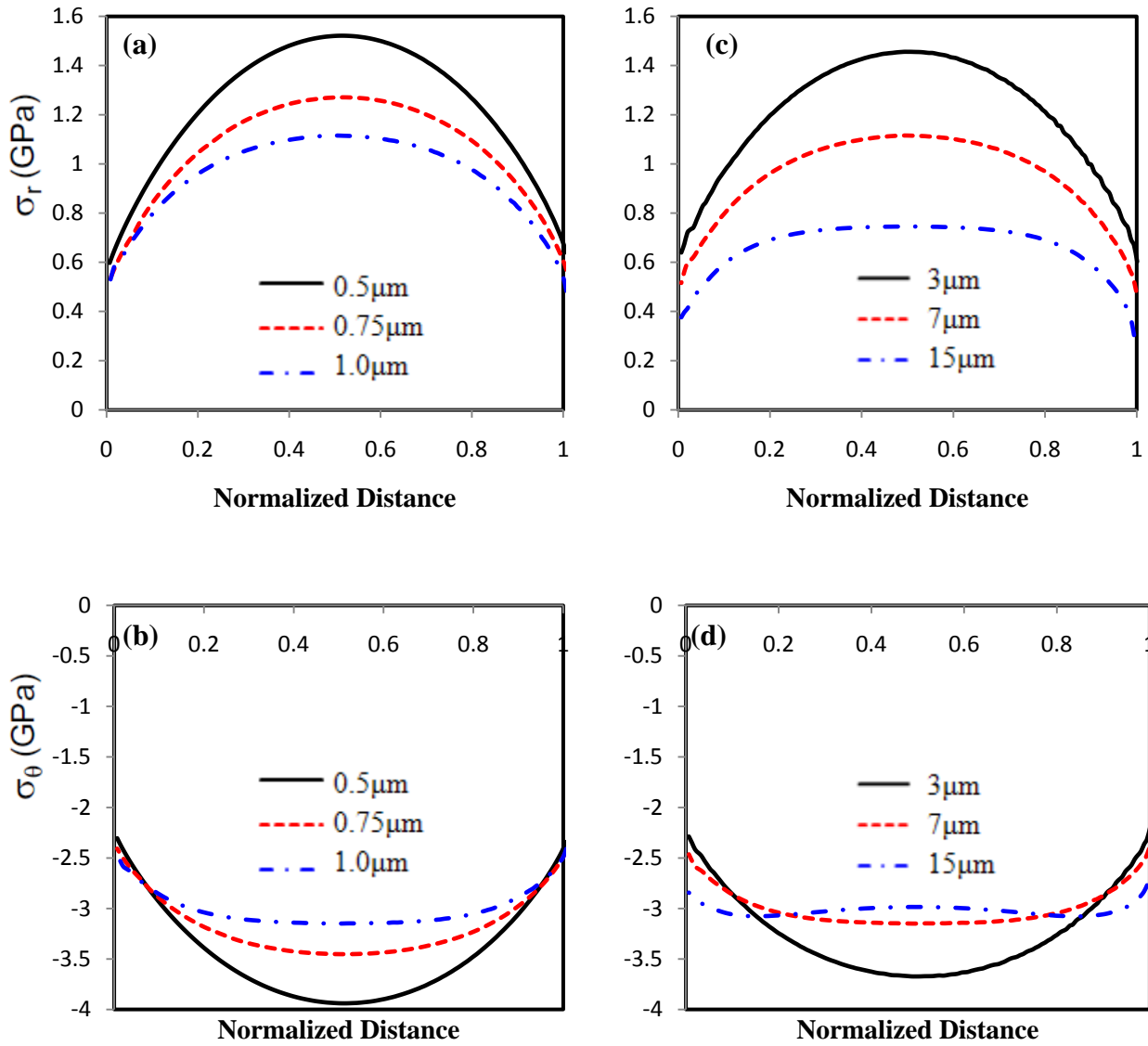


Figure 4.14. Edge radius effect on the interface stresses of diamond-coated micro/macro end mills (a) radial normal stresses of micro end mills, (b) circumferential stresses of micro end mills, (c) radial normal stresses of macro end mills, and (d) circumferential stresses of macro end mills.

Table 4.4

Edge Radius Effect on Interfacial Stresses for 2D Diamond-Coated Macro/Micro End Mills

<i>Edge Radius Effect on Interfacial Stress (Unit: GPa)</i>						
Micro End Mill (D = 0.12mm)			Macro End Mill (D = 6mm)			
r_e	σ_r	σ_θ	r_e	σ_r	σ_θ	
0.5 μm	1.52	3.92	3 μm	1.45	3.67	
0.75 μm	1.27	3.45	7 μm	1.11	3.14	
1.0 μm	1.12	3.12	15 μm	0.75	3.08	

2D Approximation with the Inclusion of a CZM

The above FEA results of diamond coated end mills under an assumption of the coating-substrate perfect contact provide well explanations and approximations for residual stress distributions; however, in reality, the coating-substrate interface does not perfectly adhere with each other, and deposition induced residual stresses exert a detrimental effect on the adhesion quality of diamond films as well as the cutting tool life (Hu, Chou & Thompson, 2008). Thus, a CZM needs to be incorporated into macro end mill 2D cross-sections. Chapter 3 has already provided the details regarding the cohesive zone modeling. Figure 4.15 illustrates maximum principal stress contours, normal tractions, and separations of quarter end mill cross-section models. It is also noted that U2 displacement values are all negative in Figure 4.15 (d). That is because after the deposition process, the entire cohesive elements drop along the negative direction in reference to the original location, which represents the zero U2 displacement.

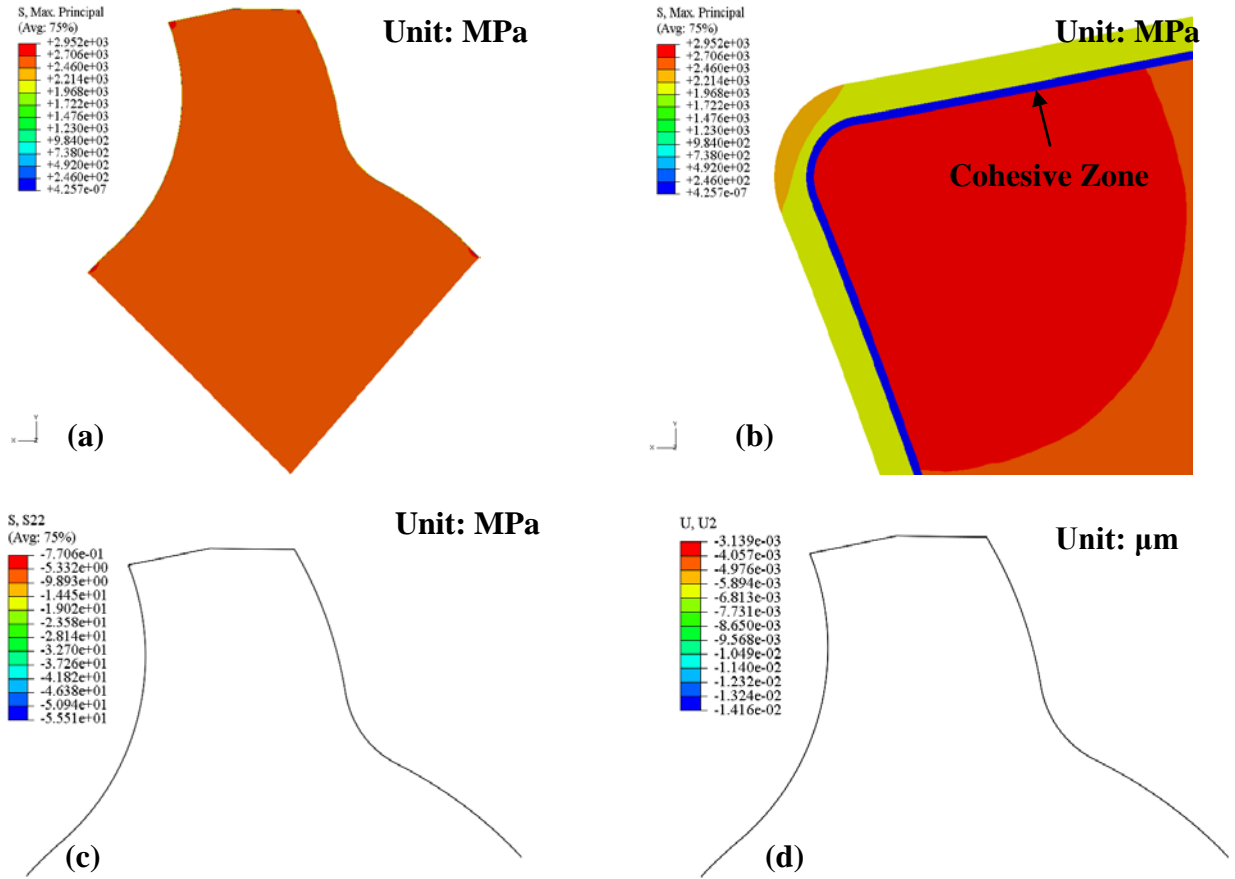


Figure 4.15. Maximum principal stress contours in a 2D diamond-coated macro end mill cross section with the inclusion of a cohesive zone model (a) entire model, (b) around the cutting edge, (c) normal tractions at the interface, and (d) normal separations at the interface ($r_c = 7 \mu\text{m}$, coating thickness = $5 \mu\text{m}$ and helix angle = 30°).

With regard to the geometric parameter effect on residual stresses, rake angle, relief angle and helix angle effects on 2D cross-sections are minor as well. This is identical with rigid contact results excluding the CZM. Figure 4.16 and Figure 4.17 illustrate edge radius and coating thickness effects on radial normal stresses and circumferential stresses, respectively.

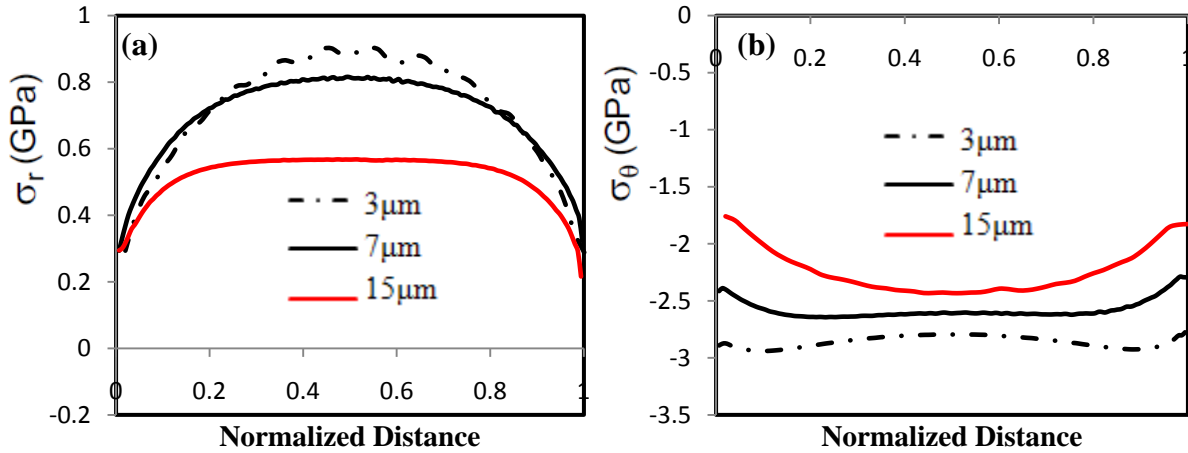


Figure 4.16. Edge radius effect on interface stresses of 2D diamond-coated macro end mills with the inclusion of a CZM (a) radial normal stress (b) circumferential stress (coating thickness = 5 μm and helix angle = 30°).

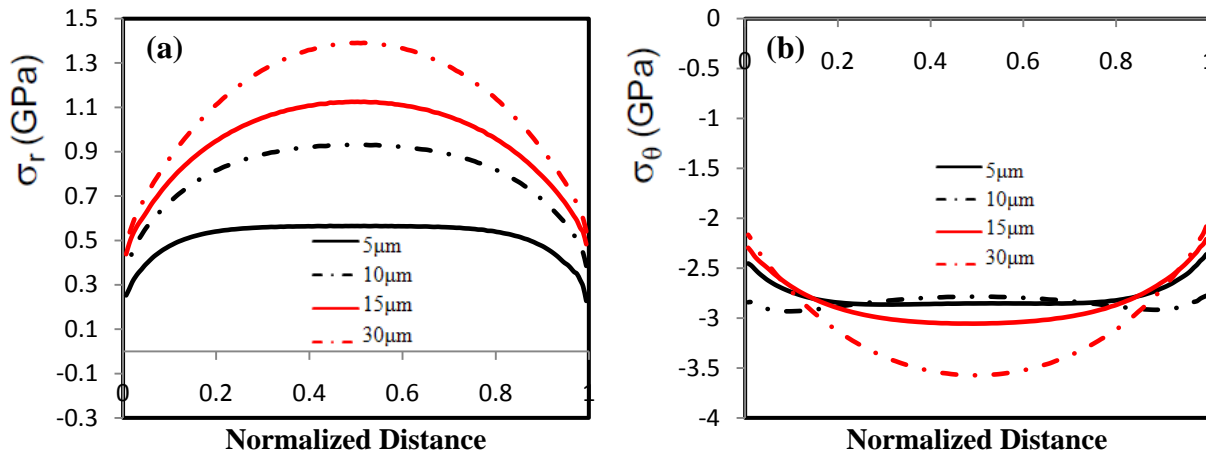


Figure 4.17. Coating thickness effect on interface stresses of 2D diamond-coated macro end mills with the inclusion of a CZM (a) radial normal stress (b) circumferential stress ($r_e = 15\mu\text{m}$ and helix angle = 30°).

From Figures 4.16 and 4.17, it can be noted that edge radii and coating thicknesses still exert remarkable effects on deposition residual stresses with the inclusion of a CZM. With regard to radial normal stresses (Figure 4.16(a)), the maximum stress increases from 0.57 GPa for 15 μm r_e to 0.9 GPa for 3 μm r_e . As for circumferential stresses (Figure 4.16(b)), the maximum stress is reduced from 2.94 GPa for 3 μm r_e to 2.43 GPa for 15 μm r_e . Regarding the coating

thickness effect on interface stresses, the radial normal stress increases from 0.57 GPa for 5 μm to 1.39 GPa for 30 μm , and the circumferential stress increases from 2.93 GPa for 5 μm to 3.57 GPa for 30 μm . In order to quantitatively address the difference between models with and without a CZM, Table 4.5 and Table 4.6 are presented for comparison and evaluation.

Table 4.5

Maximum Radial Normal Stresses and Circumferential Stresses for End Mills with Different Edge Radii with the Inclusion of a CZM

r_e	σ_r (Unit: GPa)		σ_θ (Unit: GPa)	
	End Mill (CZM)	End Mill (Rigid Contact)	End Mill (CZM)	End Mill (Rigid Contact)
3 μm	0.9	1.45	2.94	3.67
7 μm	0.82	1.11	2.64	3.14
15 μm	0.57	0.75	2.43	3.08

Table 4.6

Maximum Radial Normal Stresses and Circumferential Stresses for End Mills with Different Coating Thicknesses with the Inclusion of a CZM

Coating Thickness	σ_r (Unit: GPa)		σ_θ (Unit: GPa)	
	End Mill (CZM)	End Mill (Rigid Contact)	End Mill (CZM)	End Mill (Rigid Contact)
5 μm	0.57	0.75	2.86	3.08
10 μm	0.99	1.08	2.93	3.13
15 μm	1.13	1.26	3.06	3.34
30 μm	1.39	1.51	3.57	3.86

Based on the evaluation of above tables, it can be noted that a CZM does play a role in altering the magnitude of residual stresses in diamond-coated end mill cross-sections. For the case with a smallest edge radius with the inclusion of a CZM, the interface stress curve fluctuates and becomes unsmooth. It is also interesting to note that with the inclusion of a cohesive zone, interface stresses all decrease without exception. The reasons for these phenomena are: (1) A CZM provides a buffering zone between a coating and a substrate; also, interface stresses induced from the thermal expansion mismatch transfer stresses to the cohesive zone, thus reducing interface stresses on both coating and substrate sides; however, for rigid contact cases, since coatings and substrates bond perfectly with each other, residual stresses are certainly larger since no stress loss caused by the cohesive zone happens along the interface, and (2) the cohesive zone inclusion slightly alters the overall and the edge shape of the interface, thus affecting interface stresses.

Conclusions

In this study, diamond-coated macro/micro end mill solid modeling techniques have been accomplished using CAD software. The obtained 3D diamond-coated end mill CAD model has also been successfully imported into FEA software for residual stress analysis. FEA results indicate that the magnitude of longitudinal normal stresses in the area of less curvatures is in the neighborhood of 3 GPa in compression. The developed CAD modeling techniques for end mills have been further employed to design end mills with different geometric parameters, i.e. the helix angle. 2D approximation of residual stresses has been applied for diamond-coated end mill cross-sections. The residual stresses distributed on diamond-coated end mills can be remarkable. With regard to micro-level geometric parameters, the edge radius is a most dominant factor affecting interface stresses, and the coating thickness effect on interface stresses is only second

to the edge radius. Radial normal stresses are largely tensile which are supposed to affect the adhesion quality. With macro-level geometric parameters changed, i.e. the helix angle, interface stresses are slightly affected. Further noted is that when the size of macro end mills is scaled down to a micro level, interface stresses are increased. Last but not the least, the trial and the investigation of a CZM effect on deposition residual stresses are conducted, and 2D approximation is duplicated, as has been conducted in rigid contact cases. The results show that with the CZM inclusion, all three of stress components are altered and reduced to smaller values, and for the small edge radius case, i.e., 3 μm , the interface stress curve slightly fluctuates due to stress concentrations caused by geometric sharpness. Regarding future works, since deposition residual stresses will also be affected by induced mechanical and thermal loads during milling processes, it is critical to study stress field evolutions during milling processes to make best use of diamond-coated end mills.

Acknowledgments

This research is supported by the National Science Foundation: 0741028.

References

- Bower, A. F. & Fleck, N. A. (1994). Brittle fracture under a sliding line contact, *Journal of the Mechanics and Physics of Solids*, 42(9), 1375–1396.
- Bruno, F., Friedrich, C. & Warrington, R. O. (1995). The miniturization technologies: past, present, and future. *IEEE Transactions on Industrial Electronics*, 42(5), 423–430.
- Damazo, B. N., Davies, M. A., Dutterer, B. S., & Kennedy, M. D. (1999). A summary of micro-milling studies. *First International Conference and General Meeting of the European Society of Precision Engineering and Nanotechnology, Bremen, May 31–June 4*, 322–325.
- Eberhardt, A. W. & Peri, S. (1995). Surface breaking cracks in layered Hertzian contact with friction, *STLE Tribology Transaction*, 38(2), 299–304.
- Ehmann, K. F. (1990). Grinding wheel profile definition for the manufacture of drill flutes. *CIRP Annal*, 39(1), 153–156.

- Friedman, M. & Meister, I. (1973). The profile of a helical slot machined by a form-milling cutter, *Annals of the CIRP*, 37(1), 53–56.
- Gabler, J. L., Schafer, H., & Westermann, H. (2000). Chemical vapour deposition diamond coated microtools for grinding, milling and drilling. *Diamond and Related Materials*, 9, 921–924.
- Gahlin, R., Alahelisten, A., & Jacobson, S. (1996). The effects of compressive stresses on the abrasion of diamond coatings, *Wear*, 196, 226-233.
- Gunnars, J. & Alahelisten, A. (1996). Thermal stresses in diamond coatings and their influence on coating wear and failure. *Surface Coatings Technology*, 80, 303–312.
- Hu, J., Chou, Y. K., & Thompson, R. G. (2008). A numerical study of interface behavior of diamond coated cutting tools, *Transactions of NAMRI/SME*, 36, 533-540.
- Hu, J., Chou, Y.K., & Thompson, R.G. (2007). On stress analysis of diamond coating cutting tools, *Transactions of NAMRI/SME*, 35, 177-184.
- <http://www.hssforum.com/MillingEN.pdf>
- Isomura, K. M., Murayama, H., Yamaguchi, N., Ijichi, N., Saji, O., Shiga, K., Takahashi, Tanaka, S., Genda, T., & Esashi, M. (2003). Development of micro-turbo charger and micro combustor as feasibility studies of three-dimensional gas turbine at micro-scale. *ASME Turbo Expo 2003*, Atlanta, GA, June 16–19, 2003, 685–690.
- Jackson, M. J., Hyde, L. J., Ahmed, W., Sein, H., & Flaxman, R. P. (2004). Diamond-coated cutting tools for biomedical applications, *Journal of Materials Engineering and Performance*, 13 (4), 421–430.
- Jackson, M. J., Robinson, G. M., & Ahmed, W. (2006). Micromachining selected metals using diamond coated cutting tools. *International Journal of Nanomanufacturing*, 1(2), 304–317.
- Jeon, Y. & Pfefferkorn, F. E. (2007). Laser-assisted machining of silicon nitride with cubic boron nitride tipped micro end mill. *Second International Conference on Micro-Manufacturing*, Greenville, South Carolina, USA, 43.
- Jun, M. B. G., Boune, K., Devor, R. E., & Kapoor, S. G. (2007). Estimation of effective error parameters in high-speed micro - endmilling. *International Journal of Machine Tools & Manufacture*, 47, 1449-1454.
- Jun, M. B. G., Devor, R.E., & Kapoor, S.G. (2006). Investigation of the dynamics of microend milling - part II: model validation and interpretation. *Journal of Manufacturing Science and Engineering, Transactions of the ASME*, 128(4), 901–912.
- Kaldor, S., Rafael, A. D., & Messinger, D. (1988). On the CAD of profile for cutters and helical

- flutes geometrical aspects. *CIRP 37/1*, 53–56.
- Kandaa, K., Takehanaa, S., Yoshidaa, S., Watanabea, R., Takanoa, S., Andob, H., & Shimakurab, F. (1995). Application of diamond-coated cutting tools. *Surface and Coatings Technology*, 73(1-2), 115-120.
- Kang, I. S., Kim, J. S., Kim, J. H., Kang, M. C., & Seo, J. Y. W. (2007). A mechanistic model of cutting force in the micro-end-milling process. *Journal of Materials Processing Technology*, 29, 117–127.
- Kim, C.-J. & Bono, M., & Ni, J. (2002). Experimental analysis of chip formation in micro-milling. *Technical Paper Society of Manufacturing Engineers, MR(MR02-159)*, 2002.
- Kim, J. H., Park, J. W., & Ko, T. J. (2008). End mill design and machining via cutting simulation. *Computer-Aided Design*, 40, 324–333.
- Kim, Y. H. & Ko, S. L. (2002). Development of design and manufacturing technology for end mills in machining hardened steel. *Journal of Materials Processing Technology*, 653–661.
- Kobayashi, A. (2005). The features and application of UPC nano-micro forming tools. *Industrial Diamond Review*, 28–30.
- Ko, S. L. (1994). Geometrical analysis of helical flute grinding and application to end mill. *Transactions of NAMRI/SME*, 22, 165–172.
- Liu, X., Devor, R. E., Kapoor, S. G., & Ehmann, K. F. (2004). The mechanics of machining at the microscale: assessment of the current state of the science. *ASME Journal of Manufacturing Science and Engineering*, 126, 666–678.
- Miao, C., Qin, F., Sthur, G., Chou, K., & Thompson, R. (2009). Integrated design and analysis of diamond-coated drills. *Computer-Aided Design & Applications*, 6(2), 195-205.
- Qin, F., Chou, Y. K., Nolen, D., & Thompson, R. G. (2009). Coating thickness effects on diamond coated cutting tools. *Surface & Coatings Technology*, 204, 1056–1060.
- Quinto, D. T., Santhanam, A. T., & Jinal, E. C. (1988). Mechanical properties, structure and performance of chemically vapor-deposited and physically vapor-deposited coated carbide tools. *Materials Science and Engineering, A 105/106*, 443-452.
- Sein, H., Ahmed, W., Jackson, M., Woodward, R., & Polini, R. (2004). Performance and characterisation of CVD diamond coated, sintered diamond and WC-Co cutting tools for dental and micromachining applications. *Thin Solid Films*, 455–461.
- Stephenson, D. A. & Agapiou, J. S. (1997). *Metal cutting theory and practice*. Marcel Dekker, Inc., 191-205.

- Tlusty, J., Smith, S., & Zamudia, C. (1991). Operation planning based on cutting process model, *Annals of the CIRP* 40/1, 95–98.
- Torres, C. D., Heaney, P. J., Sumant, A.V., Hamilton, M. A., Carpick, R. W., & Pfefferkorn, F. E. (2009). Analyzing the performance of diamond-coated micro end mills. *International Journal of Machine Tools and Manufacture*, 49, 599–612.
- Trent, E. M. & Wright, P. K. (2000). *Metal Cutting* (4th edition). Butterworth-Heinemann, 14-17.
- Walker, J. R. (2000). *Machining fundamentals: from basic to advanced techniques*. The Goodheart-Willcox Company, Inc., 285-305.
- Wiklund, U., Gunnars, J., & Hogmark, S. (1999). Influence of residual stresses on fracture and delamination of thin hard coatings. *Wear*, 232, 262–269.
- Williams, R. E., Huang, Y., Melkote, S., Kinsey, B., Sun, W., & Yao, D. (2005). Recent advances in micro/meso-scale manufacturing processes. *International Mechanical Engineering Congress and Exposition*, Orlando, Florida, ICMECE 2005-79889.
- Zoestbergen, E. & De Hosson, J. T. (2002). Crack resistance of PVD coatings: influence of surface treatment prior to deposition, *Surface Engineering*, 18(4), 283–288.

CHAPTER 5

CONCLUSIONS AND RECOMMENDATIONS FOR FUTURE RESEARCH

Conclusions

This thesis studies the interface behavior of diamond-coated tungsten-carbide tools, the deposition residual stresses as well as the methodologies to model complex diamond-coated tools such as drills and end mills. The conclusions and major findings reached from this research are summarized in this chapter.

Chapter 2 discusses CAD modeling techniques to achieve 3D diamond-coated drill models as well as FEA of the residual stresses in diamond-coated drills during the deposition process. 3D FEA results indicate that the nominal longitudinal normal stresses in the area of less curvature are about 3 GPa in compression. The 2D approximation of FEA results reveals that significant residual stresses are generated on the diamond-coated drills during the deposition process. Among different geometric parameters, the micro level geometry, such as the edge radius, has the most dominant effect on the interface stresses. It has also been detected that the radial normal stresses can become largely tensile, over 1.0 GPa. The helix angle, point angle, and web-thickness affect the wedge angle at the cutting tip, but their effects on the interface stresses are slight.

Chapter 3 develops numerical methods to study the interface behavior of diamond-coated tools through indentation simulations. A bilinear cohesive zone model (CZM) is introduced into the coating-substrate interface to characterize its behavior. The major findings attained from the indentation simulations with a spherical indenter are summarized as follows: (1) under a coating

thickness equal to 30 μm , the relationship between the indentation loading force and the delamination size is non-linear and the minimum indentation loading force to initiate interface delamination of the samples with and without residual stresses are about 98.2 N and 110 N, respectively, which indicate that the residual stresses will reduce the critical loading for interface delamination, (2) under the same indentation loading force, the delamination size decreases with the increase of the coating Young's Modulus, (3) under the same indentation loading force, no delamination occurs at the coating-substrate interface for coatings with 40 μm and 50 μm thicknesses. For coatings with a 5 μm to 40 μm thickness, the delamination size increases noticeably with the decrease of the coating thickness; however, further decreasing the coating thicknesses to smaller values results in a reverse relationship, and (4) the samples with residual stresses included are more susceptible to interface delamination. The results obtained from the indentation simulations with a wedge indenter are listed here: (1) the specimen surface curvature slightly affects the loading vs. displacement curve, and it influences interface delamination; a large curvature model is more susceptible to interface delamination, (2) the augmented coating Young's Modulus decreases interface delamination, and coatings with a larger Young's Modulus are more resistant to interface delamination, (3) the residual stresses not only make the coating-substrate system more compliant but also cause more severe interface delamination, (4) the system with a thicker coating thickness will have more resistance to interface delamination, and (5) the combined residual stress and curvature effects on the critical loading are significant.

Chapter 4 discusses the CAD modeling methodologies of diamond-coated macro/micro end mills, and the FEA of deposition residual stresses developed in the diamond-coated end mills. It is concluded that (1) the magnitude of longitudinal normal stresses in the area of less curvature is in the neighborhood of 3 GPa in compression, (2) the 2D FEA approximation indicates that the

residual stresses distributed in diamond-coated end mills can be remarkable, and the edge radius dominantly affects the interface residual stresses; the radial normal stresses are largely tensile, greater than 1.0 GPa, (3) with the macro level geometric parameters changed, i.e. the helix angle, the interface stresses are slightly affected, (4) the interface residual stresses increase when macro end mills are scaled down to the micro-size, and (5) with the inclusion of the CZM, all three residual stress components are altered and reduced to smaller values compared with the rigid contact models excluding the CZM, and for the small edge radius case, i.e. 3 μm , the interface stress curve slightly fluctuates due to the stress concentration caused by the geometric sharpness.

Contributions

The contributions of this study can be summarized below.

1. This study conducts systematic approaches regarding the CAD modeling methodologies of diamond-coated drills and diamond-coated macro/micro end mills with different geometric parameters. The FEA of 3D and 2D cross-sectional approximation of those diamond-coated tools have been developed to investigate the depositional residual stresses as well as the interface stresses around cutting edge. The cohesive zone model is incorporated into the 2D cross-section model to study its effect on depositional residual stresses.

2. A bilinear traction-separation law has been applied to characterize the interface behavior of diamond-coated tungsten carbide tools. The FEA has been developed and implemented to simulate the indentations with a spherical indenter on diamond-coated tools to investigate the coating attribute effects on the interface behavior.

3. The same methodologies discussed have also been applied to the indentation models with a wedge indenter to investigate the coating attribute, substrate surface curvature, residual

stresses, and their combined effects on interface delamination, which provides more accurate approximations for the tool failure mechanism.

Recommendations for Future Research

This study provides a better understanding of modeling methodologies, geometric shapes, and the depositional residual stresses development of the diamond-coated tooling with complex geometries, as well as the tool failure mechanism of coating-substrate systems. The directions of the future research can be summarized as follows:

1. The tool stress and temperature distributions during machining processes can be critical to tool failures and wears of the diamond-coated tooling. With the geometric shape and depositional residual stress distributions of diamond-coated tools with complex shapes attained in this study, this research can be advanced to investigate the wear mechanism through 2D drilling and 2D end milling simulations with the consideration of depositional residual stresses on diamond-coated tools. Parametric studies, such as the point angle, the helical angle, the rake angle, the relief angle, the coating thickness, and the edge radius, etc. can be conducted to analyze their corresponding effects on the coated tool wear mechanism with cutting simulations.
2. The indentation with a wedge indenter experiments can be conducted on the tool edge rounding area to investigate the curvature effects on the interface delamination. The achieved experimental results can be compared with simulated outcomes to test the validity and the feasibility of numerical results.
3. The developed cohesive zone model can be incorporated into 2D turning simulations to investigate the delamination condition during material removal processes. The parametric study (for example, the feed, the cutting speed, and the depth of cut) effects on the interface delamination during machining processes can also be carried out with 2D cutting simulations.

For verification purposes, cutting experiments with the same process parameters can be conducted and used to compare with the simulation results.

REFERENCES

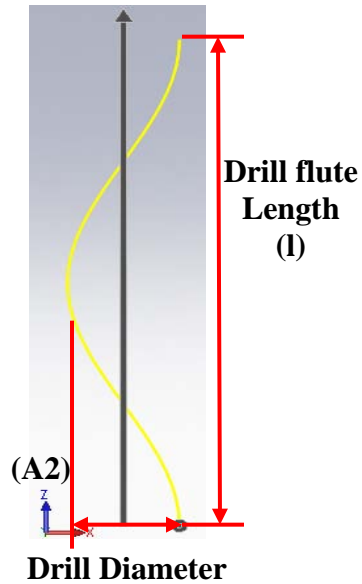
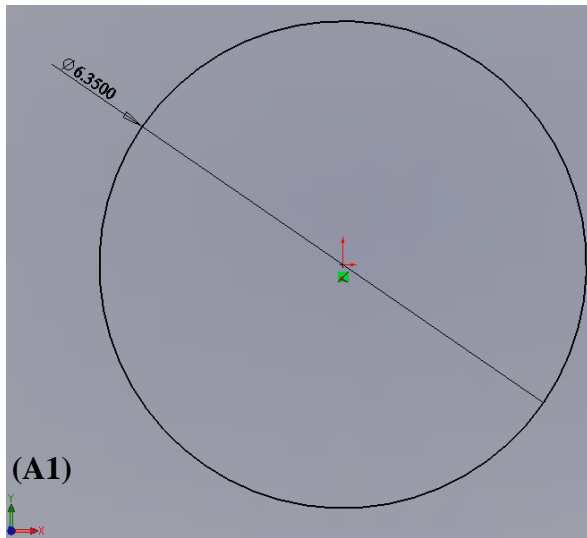
- Barenblatt, G. I. (1962). Mathematical theory of equilibrium cracks in brittle fracture. In: Dryden, H.L., von Karman, T. (Eds.). *Advances in Applied Mechanics, VII*. Academic Press, New York, 55–125.
- Barenblatt, G. I. (1959). The formation of equilibrium cracks during brittle fracture. General ideas and hypothesis. Axially-symmetric cracks. *Journal of Applied Mathematics Mechanics, 23*(3), 622–636.
- Chandra, N., Li, H., Shet, C., & Ghonem, H. (2002). Some issues in the application of cohesive zone models for metal–ceramic interfaces. *International Journal of Solids and Structures, 39*, 2827–2855.
- Chou, Y. K. & Liu, J. (2005). CVD diamond tool performance in composite machining. *Surface and Coatings Technology, 200*, 1872–1878.
- Geubelle, P. H. & Baylor, J. (1998). Impact-induced delamination of laminated composites: a 2D simulation. *Composites Part B: Engineering, 29*(5), 589–602.
- Hu, J., Chou, Y. K., & Thompson, R. G. (2008). A numerical study of interface behavior of diamond coated cutting tools, *Transactions of NAMRI/SME, 36*, 533-540.
- Hu, J., Chou, Y. K., Thompson, R. G., Burgess, J., & Street, S. (2007). Characterizations of nano-crystalline diamond coating cutting tools. *Surface and Coatings Technology, 202*, 1113–1117.
- Hu, J., Chou, Y. K., & Thompson, R. G. (2008). Nanocrystalline diamond coating tools for machining high-strength Al alloys. *International Journal of Refractory Metals & Hard Materials, 26*, 135–144.
- Hu, J., Chou, Y. K., & Thompson, R. G. (2007). On stress analysis of diamond coating cutting tools, *Transactions of NAMRI/SME, 35*, 177-184.
- Qin, F., Chou, K., Noland, D., Thompson, R. G., & Ni, W. N. (2009). Cutting edge radius effects on diamond-coated tools. *Transactions of NAMRI/SME, 37*, 653-660.
- Qin, F., Chou, Y. K., Nolen, D., & Thompson, R. G. (2009). Coating thickness effects on diamond coated cutting tools. *Surface & Coatings Technology, 204*, 1056–1060.
- Renaud, A., Hu, J., Qin, F., & Chou, Y. K. (2009). Numerical simulations of 3D tool geometry effects on deposition residual stresses in diamond coated cutting tools. *International Journal of Mechatronics and Manufacturing Systems, 2*(4), 490-502.

APPENDIX A

3D DIAMOND-COATED DRILL CAD MODELING PROCESS

The basic geometric parameters of the designed drill could be summarized below. Radius

(R): 3.175mm, point angle (p): 118° , web thickness (w): 1.35mm, helical angle (h): 30° .

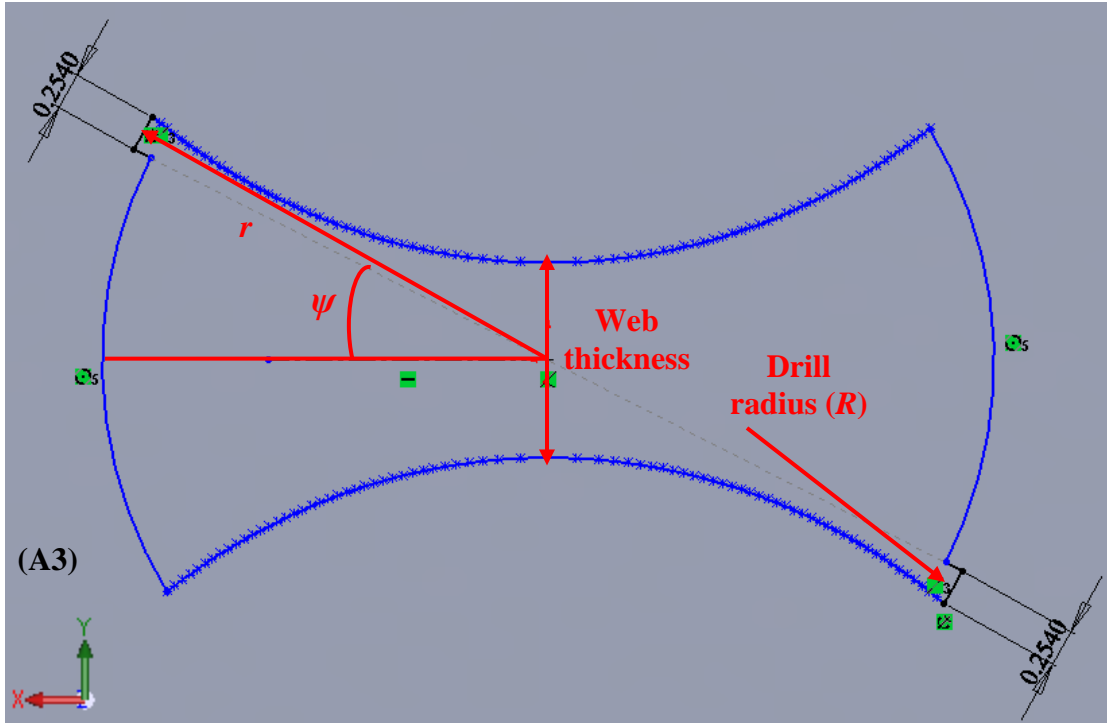


(A1) Create a circle with 6.35mm diameter.

(A2) use the circle created in the step (A1) to generate a helix curve with a 34.96mm drill flute length (l) and the helix direction is counter clockwise. The drill flute length (l) can be calculated by the following: equation:

$$h = \tan^{-1} \frac{2\pi R}{l} \dots\dots\dots(a1)$$

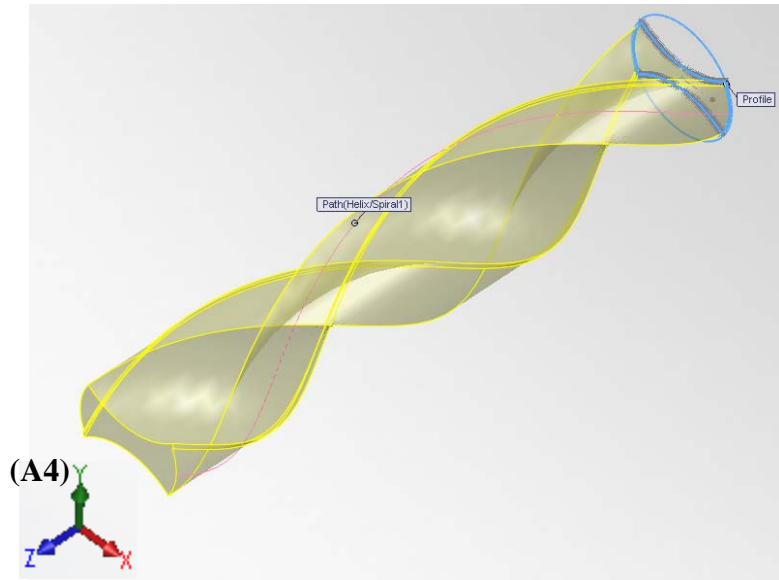
In equation (a1), h is the helix angle, R for drill radius and l for drill flute length.



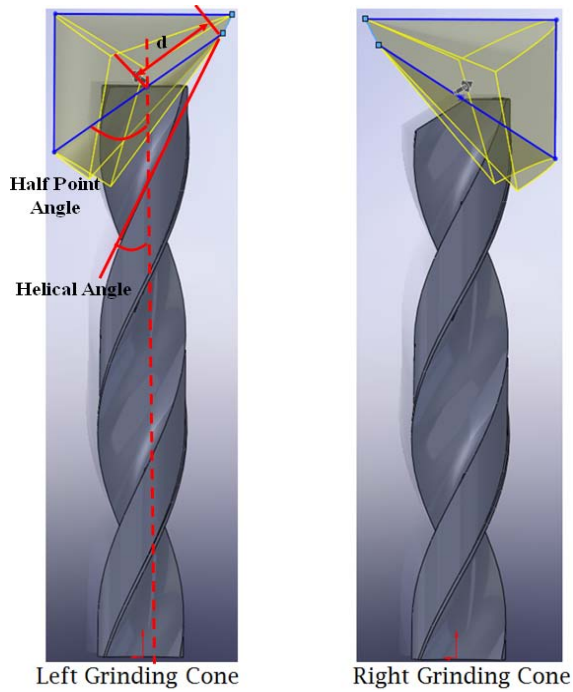
$$\psi = \sin^{-1} \frac{W}{2r} + \frac{\sqrt{r^2 - (W/2)^2}}{r} \tan(h) \cot(p) \dots\dots\dots (a2)$$

(A3) With regard to the geometric parameters in this equation, w is the webthickness, p for point angle and h for helical angle.

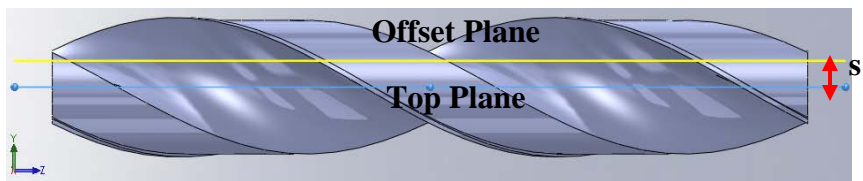
The drill cross-section is determined by the equation (a2). Here, r is varying from $w/2$ to drill radius. This ensures that the flank section produces a drill with a straight cutting edge.



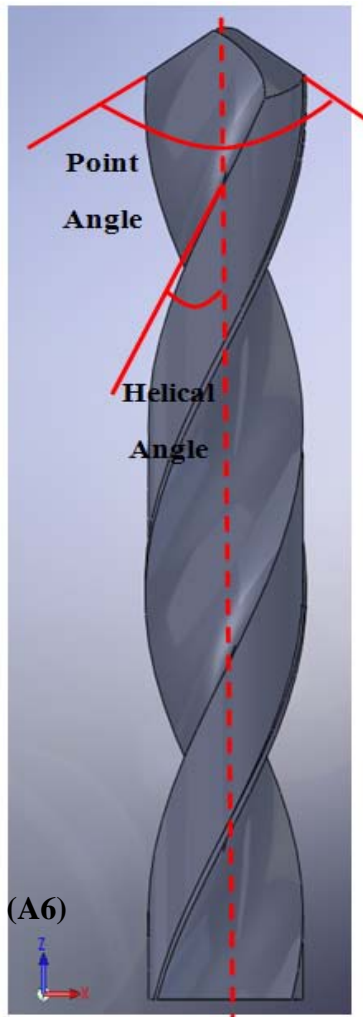
(A4) With the created cross-section and helix curve, the drill flute body can be generated by sweeping the cross-section along the helix curve.



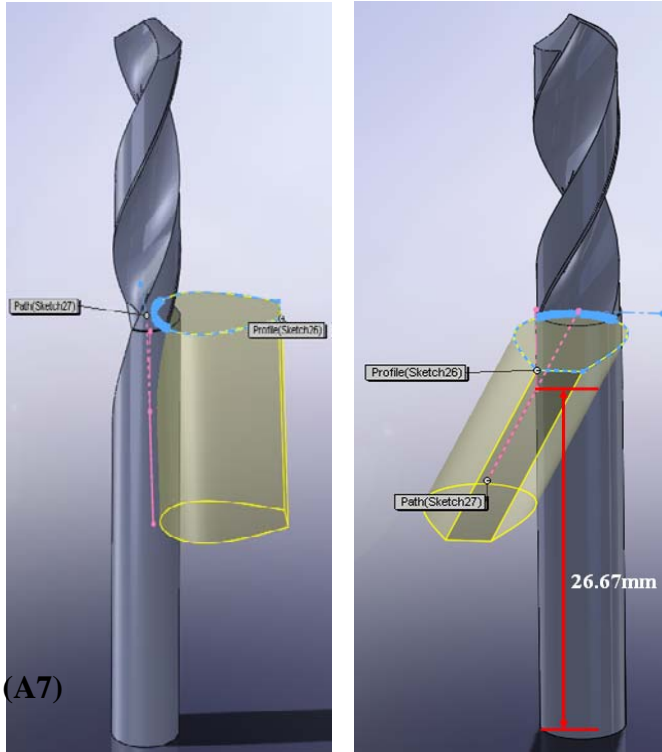
(A5)



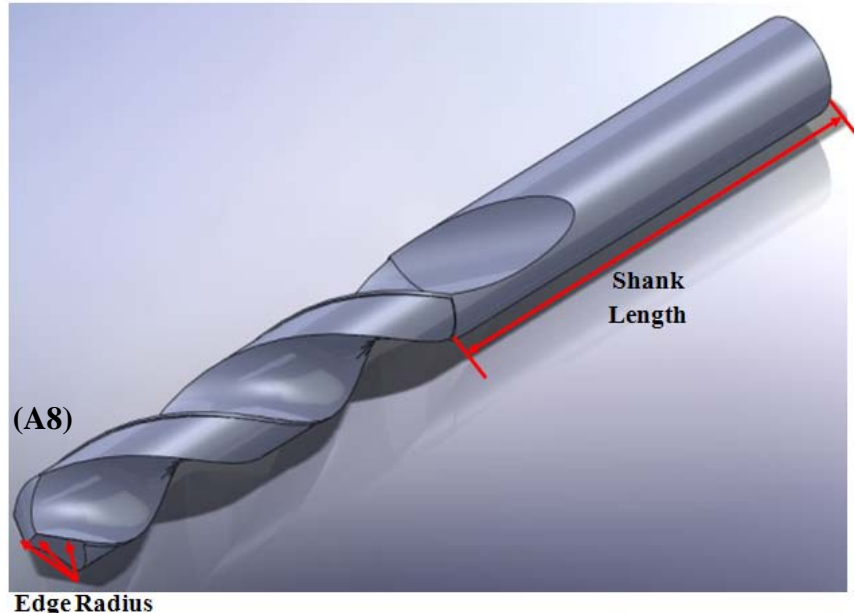
(A5) The left and right grinding cone can be generated based on the values of the point angle, the helical angle, d (5.5mm) and s (1.2mm). s represents the distance between the top plane and the offset plane and this offset plane that locates on both sides, on which the left and the right grinding cones are defined and generated, respectively.



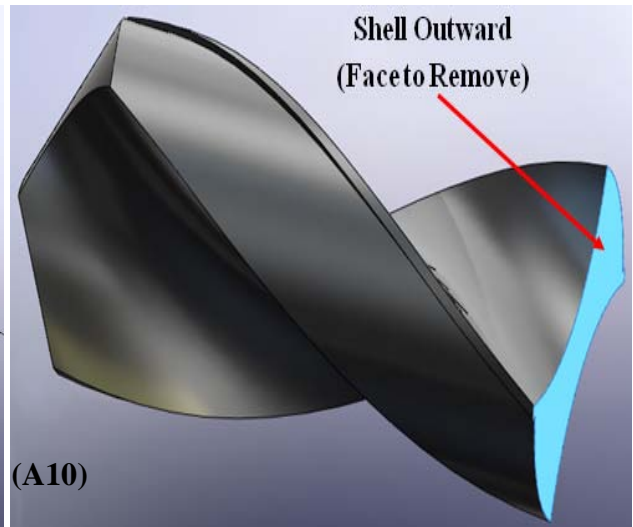
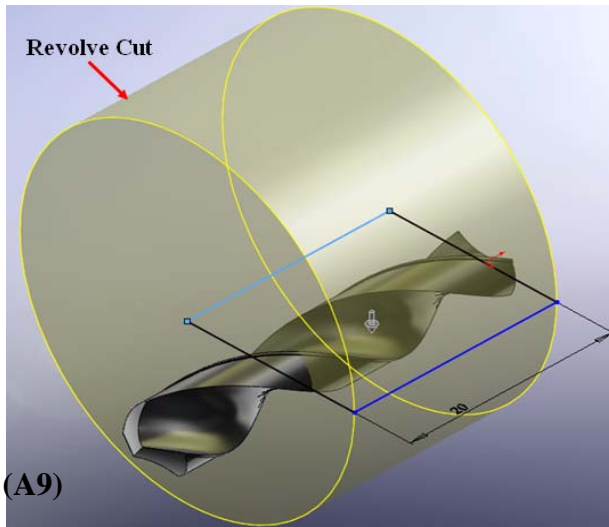
(A6) after finishing the procedures above, the illustration in figure A6 can be obtained. However, in order to attain the fully designed drill, it is necessary to add the shank to the drill flute body.



(A7) use the swept cut function to create the cut feature on both sides in order to create hollow areas on the drill which could facilitate the chip flow.

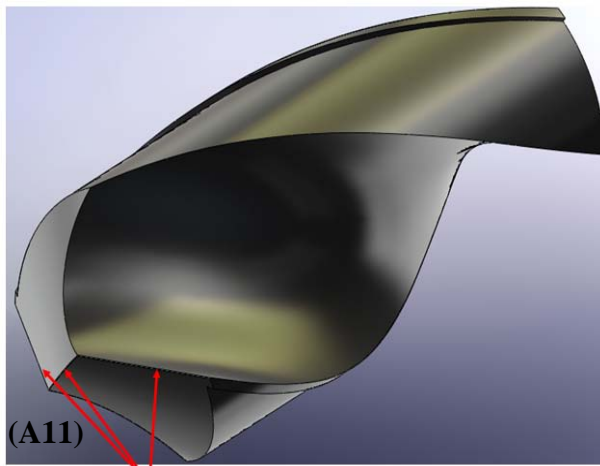


(A8) this figure illustrates the fully designed uncoated drill.

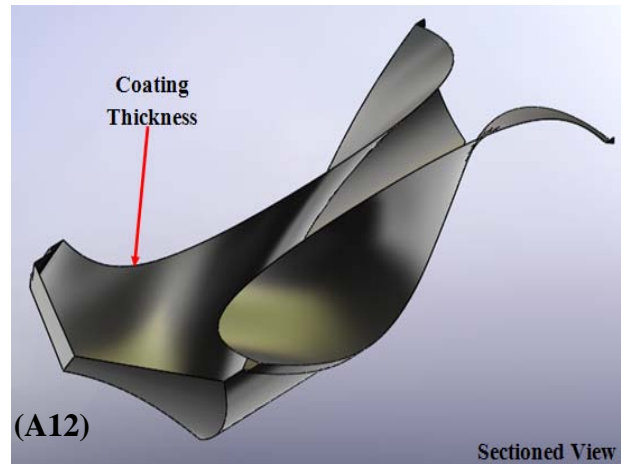


(A9) create a revolve cut feature on the drill in order to reserve a portion for coating creation.

(A10) use the shell function to remove the highlighted surface to create a shell body representing the diamond coating.

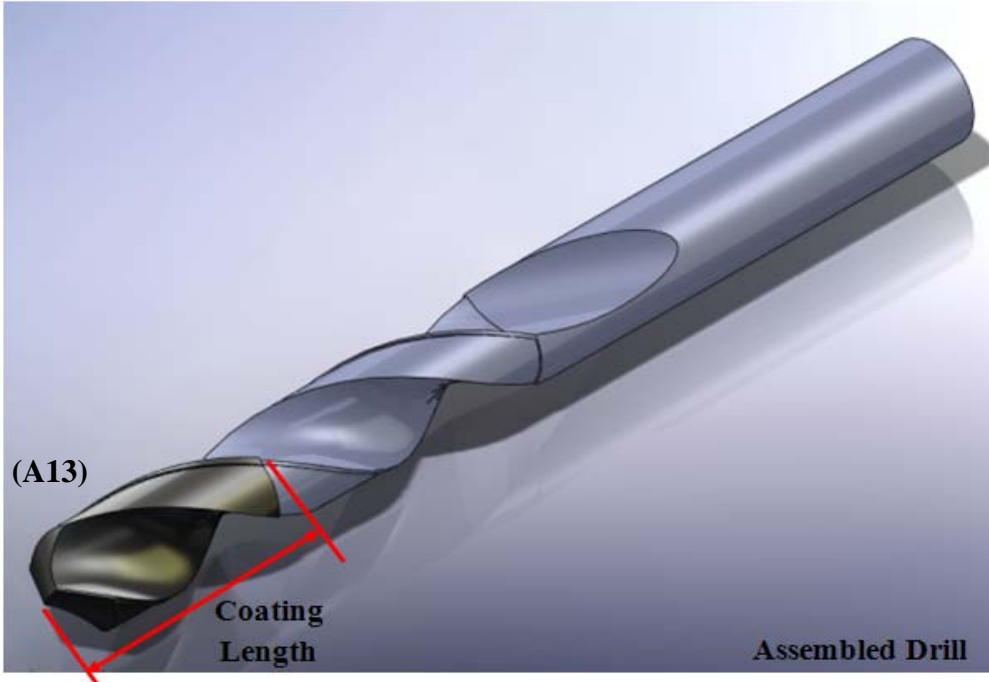


Edge Radius



(A11) round two cutting lips and one chisel edge on the coating.

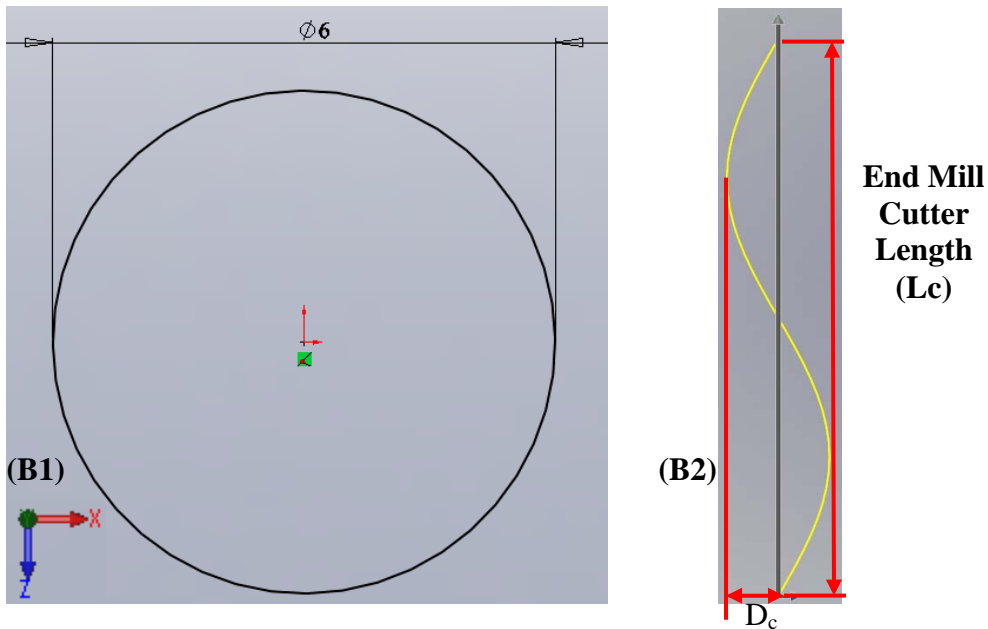
(A12) sectional view of a diamond coating.



(A13) a diamond-coated drill.

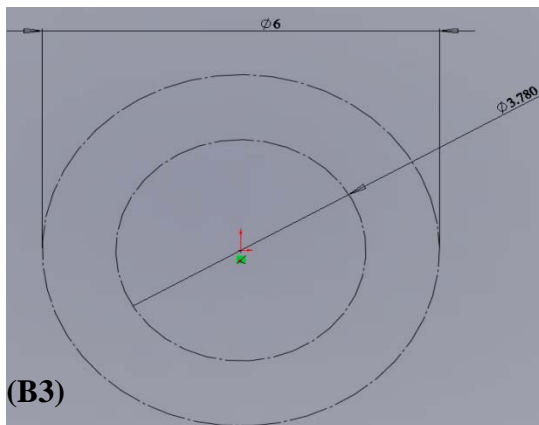
APPENDIX B

3D DIAMOND-COATED END MILL CAD MODELING PROCESS

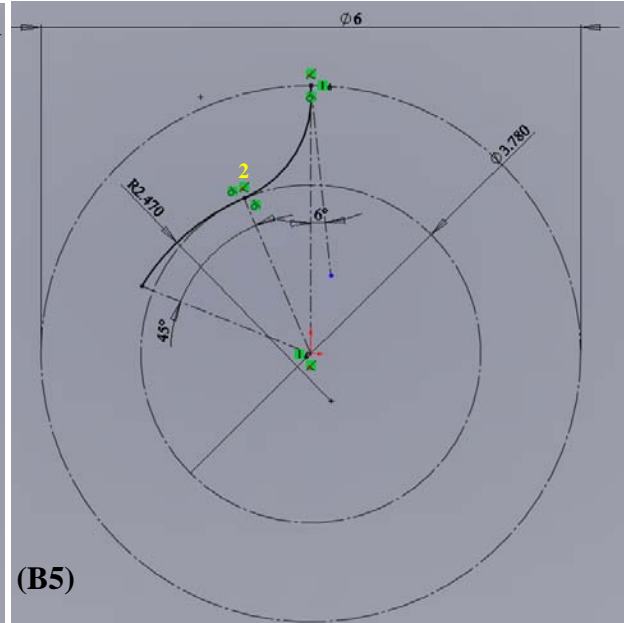
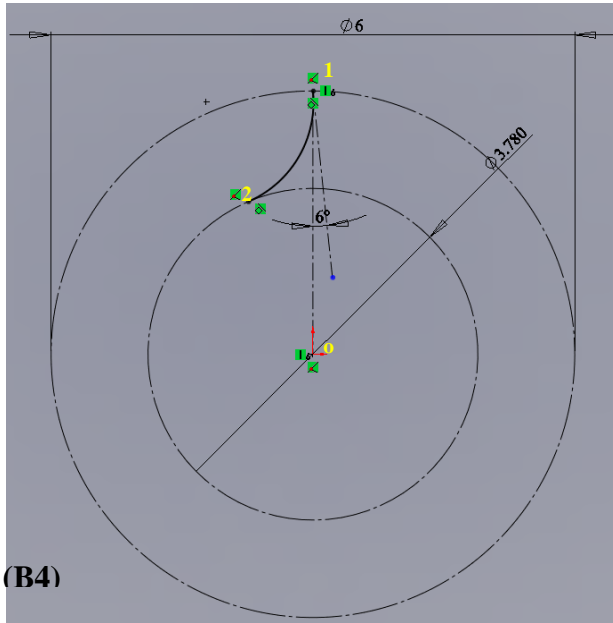


(B1) Create a circle with D_c (Cutter Diameter) = 6.0mm.

(B2) Based on the circle created above, a helix curve is generated with a pitch = 32.6mm (= L_c) and helical angle = 30° .

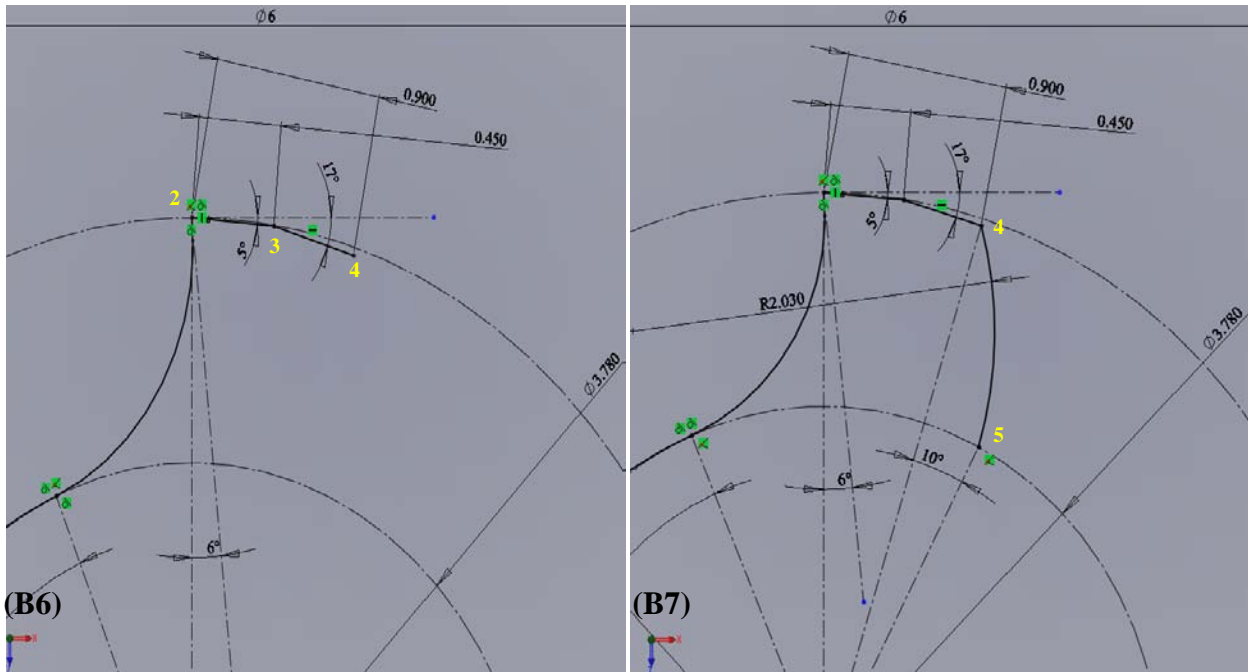


(B3) Draw two concentric circles with D_c (Cutter Diameter) = 6.0mm, R_i (Inner Radius) = 1.89mm. Besides, two circles here are set as the construction lines.



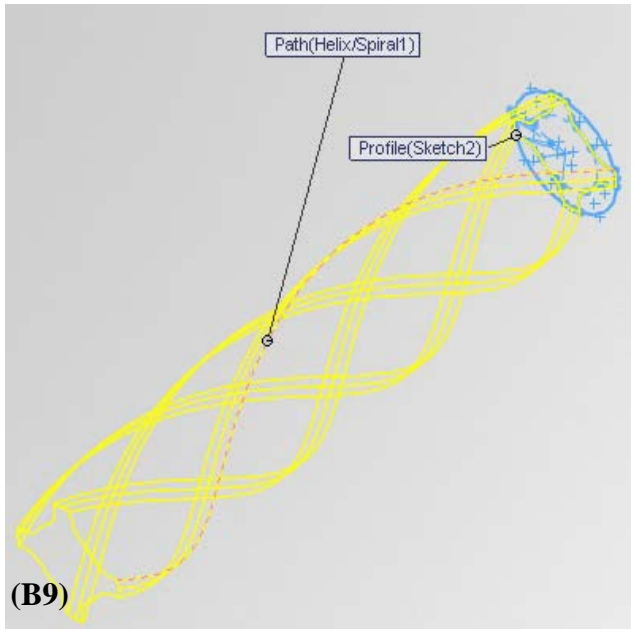
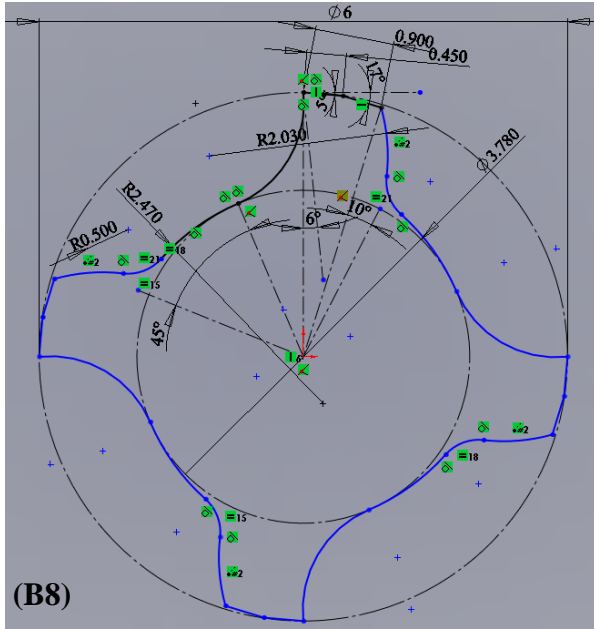
(B4) Connect the point#1 and the point#2 to create a curve with the point#1 located on the quarter point of the outer circle and the point#2 on the inner circle. Set this curve tangent to the inner circle. Then, draw a construction line passing the point#1 and make this line tangent to the curve_{1,2}. Again, connect the point#1 and the origin point, then define the γ (Rake Angle) = 6.0° between those two lines.

(B5) Draw another curve passing the point#2 and the radius of this curve is equal to t_1 (first wheel thickness) = 2.47mm. In order to determine the curve length, θ_1 (first wheel angle) = 45° is defined between two curve end points. This curve is set to be tangent to the curve created by (B4).



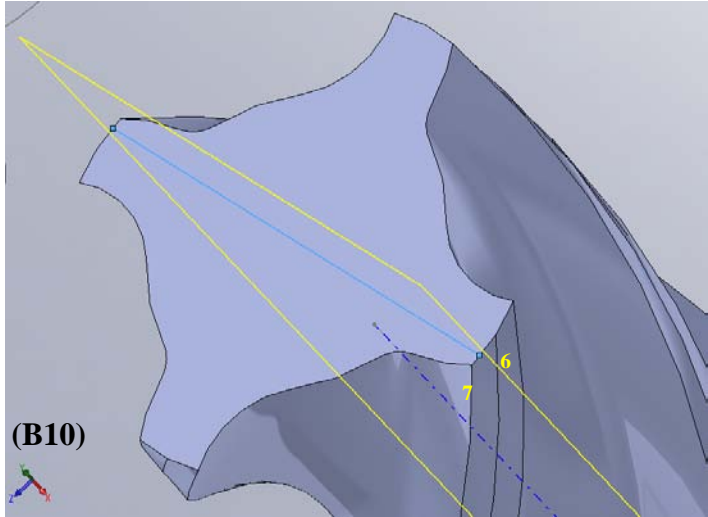
(B6) Draw a construction line passing the point#2 and set this construction line tangent with the outer circle. Then, draw another two lines in the outer circle passing through the point#2, the point#3 and the point#4. Set Φ_1 (First Relief Angle) = 5° between the line_{2,3} and the construction line tangent to the outer circle. Similarly, set Φ_2 (Second Relief Angle) = 17° between the line_{3,4} and the construction line tangent to the outer circle. The width of curve_{2,3,4} is defined as C_w (Cutter Width) = 0.9mm with point#3 set as mid-point.

(B7) Connect the point#4 and the point#5, and the point#5 is located on the inner circle. The radius of the curve_{4,5} is set as $t_2 - t_1$ (second wheel thickness) = $4.5 - 2.47 = 2.03$ mm. Besides, create two construction lines passing through the point#4, the origin and the point#5, the origin and set the angle between those two lines as θ_2 (second wheel angle) = 10° . Until now, all the dimensions are defined and what is needed to be done next is nothing, but circularly patterns all created curves.

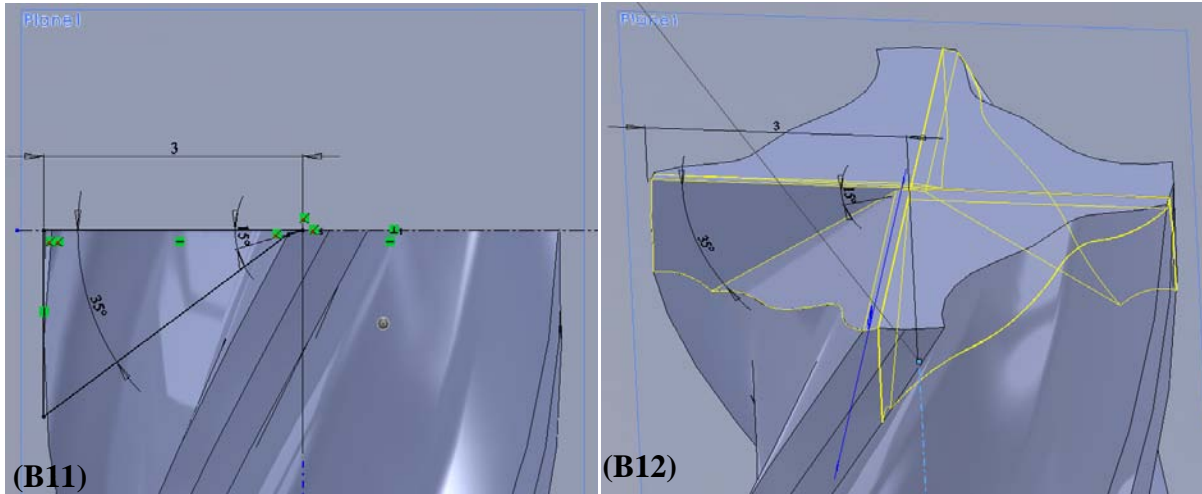


(B8) Circular pattern all created curves. Also, round off all of the transitional area with a radius = 0.5mm.

(B9) sweep the section along the helix curve to create the flute body.

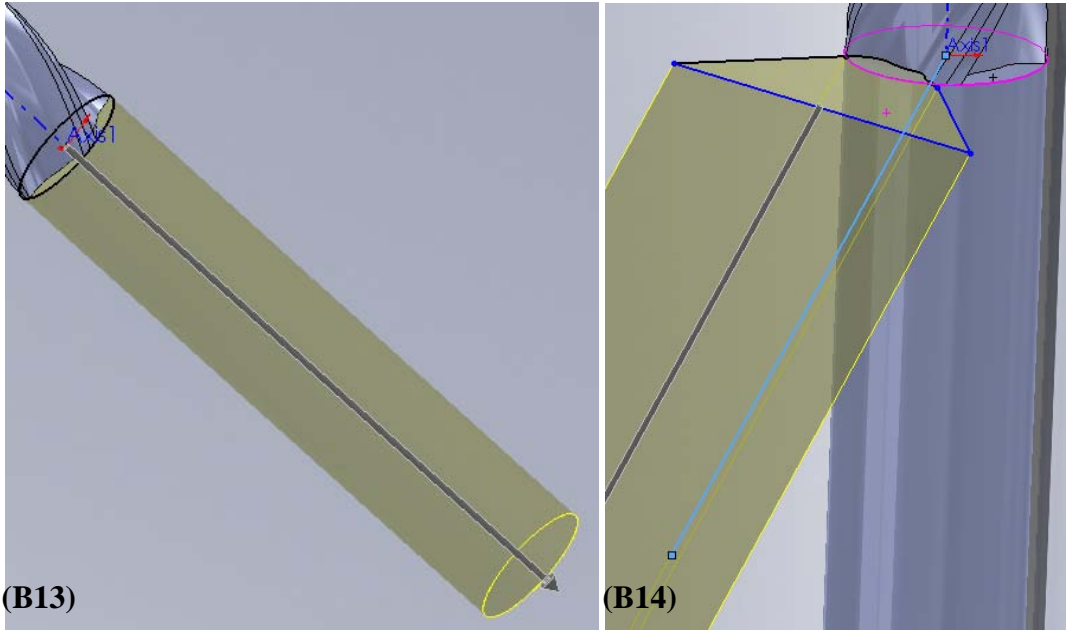


(B10) create a reference plane illustrated above, and the distance between the point #6 and the point #7 represents the width of head cutter.



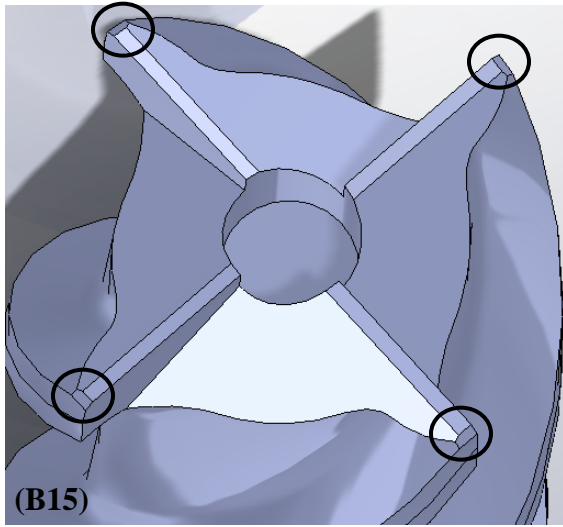
(B11) based on the plane created above, generate an extrude-cut feature on the head.

(B12) circular pattern the cut feature to generate four cut blades on the head and also drill a hole on the top of the end mill head.



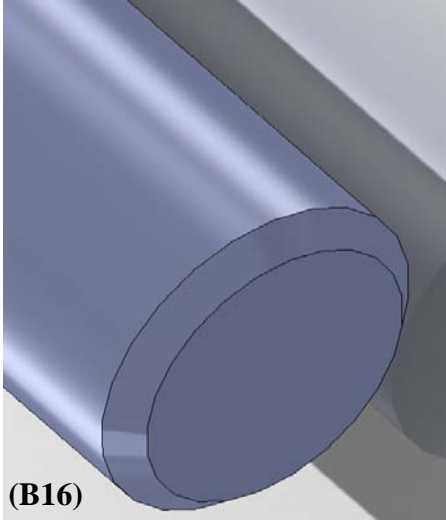
(B13) create a shank bar on the bottom of the end mill by using the extrusion function

(B14) create the hollow area by extrusion cut along path function and pattern this feature to create another 3 features.



(B15)

(B15) chamfer the highlighted circled areas.



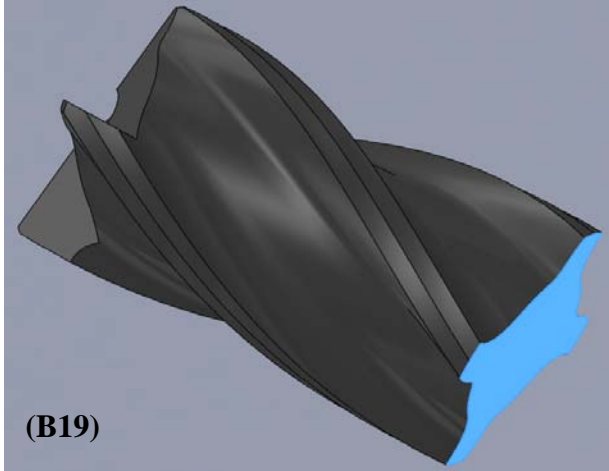
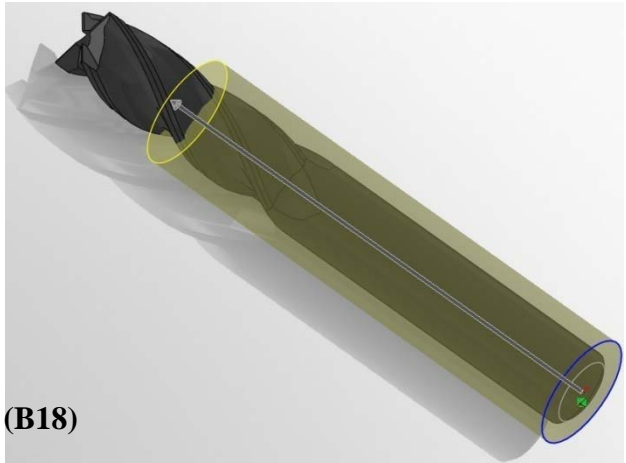
(B16)

(B16) chamfer the bottom of the shank.



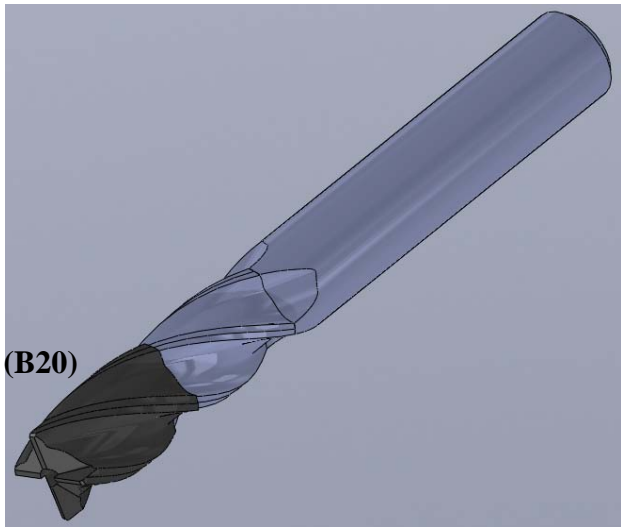
(B17)

(B17) view of fully designed uncoated end mill.



(B18) extrude cut the end mill substrate to reserve a portion for a coating.

(B19) use the shell feature to remove the highlighted surface to create a diamond coating.



(B20) round off all cut edges and assemble a coating and a substrate to create a diamond-coated end mill.